

Measurement of the ${}^3\text{He}(n, \gamma)$ Cross Section
for $E_n=0.14\text{--}2.0$ MeV

by

Robert John Komar

A thesis submitted to the Department of Physics
in conformity with the requirements for
the degree of Doctor of Philosophy

Queen's University
Kingston, Ontario, Canada

November 19, 1992

Copyright ©Robert John Komar, 1992

Abstract

The absolute cross section of the ${}^3\text{He}(n, \gamma)$ reaction was measured at five energies between $E_n=0.14\text{--}2.0$ MeV to an accuracy of $\sim\pm 10\%$. The ~ 21 MeV gamma rays were produced in a ${}^3\text{He}$ gas target, and were detected at 90° with respect to the beam direction using a spectrometer housing a $127\text{ mm} \times 76\text{ mm}$ BGO crystal. Due to the small amount of light emitted by the BGO crystal, a conventional pile-up rejection circuit was found to be inadequate for eliminating pulses with pile-up. Instead, the pulses from the BGO detector were digitized and processed off-line on a computer to allow pile-up events to be identified and corrected. The results are discussed in light of previous measurements of the two-body photodisintegration of ${}^4\text{He}$.

Statement of Originality

The work in this thesis is completely original except for the first introductory chapter, and where referenced in the text. In particular, the design of the gamma ray spectrometer, the digital pulse processing technique used, and the measurement of the ${}^3\text{He}(n, \gamma)$ cross section constitute original work. The Monte Carlo program used to track gamma rays, electrons and positrons in the BGO scintillator was produced by modifying a program developed by B.J. Varley *et al.* [Va81], as noted in the text. Most of the work was performed either independently or in collaboration with Dr. H.-B. Mak. Drs. J.R. Leslie, H.C. Evans, T.K. Alexander, E. Bonvin and D. Earle collaborated in the design and construction of the spectrometer, and are duly credited in the acknowledgements.

Acknowledgements

Foremost, I would like to express my gratitude to my supervisor, Dr. Hay-Boon Mak, for his guidance and support each time I barged into his office, and for his patience during the long spells in between. As far as advisors go, they don't get any better than that! I would also like to thank Drs. J.R. Leslie, H.C. Evans, T.K. Alexander, E. Bonvin and D. Earle for their advice during the design and construction phase of the project, and for their willingness to leap down from their pedestals and do a little shift work around the accelerator. My fellow students Luc, Rob, Chris, Jeff and Vic also deserve a ton of credit for 'volunteering' for hours of monotony in the comfy chair or the lumpy cot at the control panel. It was much appreciated.

I would like to thank Mr. Dirk Bouma for the loan of the digital storage oscilloscope, and Mr. Bob Stevenson for the use of the SUN 4/110 computer. I would also like to acknowledge the loan of 300 lbs. of paraffin and 10 lbs. of ^6Li -enriched lithium carbonate from Chalk River National Laboratory. My first son goes to Mr. Charles Hearn for keeping the accelerator and beamline operational over the course of the experiment. Dr. Peter Skensved deserves plenty o' slaps on the back for his help in matters of computing. Luc Ouellet gets my undying respect and gratitude for creating his ultra-useful data analysis package when by rights any other mortal would have been cursing his luck and eating barley sandwiches by lunch.

Finally, I would like to express my gratitude for the financial support offered by the

McLaughlin, Reinhardt and Queen's Graduate Fellowships.

Contents

Statement of Originality	ii
Acknowledgements	iii
1 Introduction	1
2 Apparatus	10
2.1 Overview of System	10
2.2 Production of Neutrons	14
2.3 ^3He Gas Target	19
2.4 The Medium Energy Gamma Ray Spectrometer	23
2.4.1 The Gamma Ray Detector	24
2.4.2 Active Shielding	28
2.4.3 Passive Shielding	33
2.4.4 Electronics	34
3 Digital Signal Processing	43
3.1 Review of Other Systems	43
3.2 The Present System	44
3.2.1 On-line Analysis	45
3.2.2 Off-line Analysis	45

4	Monte Carlo Simulations	56
4.1	Description of the Monte Carlo Program	56
4.1.1	Neutron Tracking	57
4.1.2	Gamma Ray Tracking Outside of the BGO Crystal	60
4.1.3	Gamma Ray, Electron and Positron Tracking in the BGO Crystal	61
4.1.4	Calculating the Response Functions	66
4.2	Testing of the Program	67
4.2.1	Modifications	67
4.2.2	Experimental and Calculated Results	68
4.3	Systematic Uncertainties	77
5	Procedure, Results and Analysis	81
5.1	Data Collection	81
5.2	Activity Measurements	84
5.3	Pulse Processing into Spectra	86
5.3.1	${}^7\text{Li}(p, \gamma)$ Spectra	86
5.3.2	${}^3\text{He}(n, \gamma)$ and Background Spectra	88
5.3.3	Cosmic Ray Spectrum	94
5.4	Monte Carlo Simulations	97
5.5	Extracting the ${}^3\text{He}(n, \gamma)$ Cross Section	101
6	Conclusions	108
	Bibliography	114
	Vita	120

List of Figures

1.1	The design of the SNO heavy water Čerenkov detector.	2
1.2	A preliminary design for a medium energy gamma ray source based on the ${}^3\text{He}(n, \gamma)$ reaction.	4
1.3	The relative neutron energy spectrum from ${}^{252}\text{Cf}$	4
1.4	The absolute cross section of the ${}^3\text{He}(n, \gamma)$ reaction for fast neutron capture.	5
1.5	Previous results for $\sigma_{\gamma, n}$ near the threshold.	9
2.1	Schematic top view of the spectrometer and target systems.	11
2.2	Diagram of the target system at the end of the beamline.	17
2.3	Neutron energy spectra corresponding to different positions of the gas target.	21
2.4	Neutron energy spectra for three arrangements of shadowbars	22
2.5	The calculated response functions for 10.76 MeV and 20.0 MeV gamma rays on the bare BGO crystal.	29
2.6	The response function of the plastic scintillator to gamma rays from a ${}^{22}\text{Na}$ and a ${}^{137}\text{Cs}$ source.	30
2.7	The background spectra in the spectrometer collected in coincidence and anti-coincidence with the veto counter.	31
2.8	Electronics used in conjunction with a pile-up rejection circuit.	36
2.9	Electronics used in conjunction with the digital storage oscilloscope.	36

2.10	Circuit used to clip the anode pulses from the BGO detector.	38
2.11	Circuit for the LED light pulser.	41
2.12	Circuit for the active transistor base used with the BGO detector.	42
3.1	Distributions of rise time constants θ^{-1} for ${}^7\text{Li}(p, \gamma)$ and LED light pulser events.	48
3.2	Distributions of fall time constants λ^{-1} for ${}^7\text{Li}(p, \gamma)$ and LED light pulser events.	48
3.3	Distribution of $\chi^2_{R/A}$ for ${}^7\text{Li}(p, \gamma)$ events, along with the acceptance cut. . .	49
3.4	Steps in the analysis of raw pulses.	49
3.5	Scintillator event and fit to a single pulse.	51
3.6	LED light pulser event and fit to a single pulse.	51
3.7	Pre-pulse pile-up event and fits to single and double pulses.	52
3.8	Pre-pulse pile-up event and fits to single and double pulses.	52
3.9	Post-pulse pile-up event and fits to single and double pulses.	53
3.10	Pre-pulse pile-up event and fits to single and double pulses.	53
3.11	Pile-up event with afterpulse and fits to single and double pulses.	54
3.12	Flow chart for the processing of spectra.	55
4.1	The calculated one-quantum annihilation-in-flight cross section for capture by the K and L shell electrons of bismuth.	64
4.2	Schematic diagram of the spectrometer and target system used for the resonance reaction measurements.	68
4.3	Measured and calculated yields for the ${}^{27}\text{Al}(p, \gamma){}^{28}\text{Si}$ reaction at $E_p=992$ keV. . .	69

4.4	Measured and calculated spectra for 10.76 MeV gamma rays produced via the $^{27}\text{Al}(p,\gamma)^{28}\text{Si}$ resonance reaction at $E_p=992$ keV.	71
4.5	Measured and calculated yields for the $^7\text{Li}(p,\gamma)^8\text{Be}$ reaction at $E_p=441$ keV.	72
4.6	The fitted spectral density function $\chi(E_{\alpha\alpha})$ for the first excited state of ^8Be .	75
4.7	Measured and calculated $^7\text{Li}(p,\gamma)^8\text{Be}$ spectra for the usual geometry.	76
4.8	Measured and calculated $^7\text{Li}(p,\gamma)^8\text{Be}$ spectra with some of the shielding removed.	77
5.1	The deadtime corrected $^7\text{Li}(p,\gamma)$ spectrum and background.	83
5.2	Absolute full energy peak efficiency of the germanium detector.	85
5.3	$^7\text{Li}(p,\gamma)$ spectrum from the start of the $E_p=2.30$ MeV run.	87
5.4	The sum of the distributions of θ^{-1} and λ^{-1} from the $^7\text{Li}(p,\gamma)$ events for each experiment.	89
5.5	The sum of the distributions of $\chi_{R/A}^2$ from the $^7\text{Li}(p,\gamma)$ events for each experiment.	90
5.6	The average charges of the LED pulser events from the <i>gas in</i> run.	91
5.7	The average charges of the LED pulser events from the <i>gas out</i> run.	92
5.8	The gain corrected energy spectrum for each run.	95
5.9	The average charges of the LED pulser events from the cosmic ray measurement.	96
5.10	The energy spectrum for cosmic ray events over the region of interest.	97
5.11	The Monte Carlo simulated energy spectra for the neutrons that are captured via the $^3\text{He}(n,\gamma)$ reaction.	98
5.12	The calculated gamma ray angular distribution from the $E_p=2.30$ MeV calculation.	99

5.13	The Monte Carlo simulated energy spectrum for the ${}^3\text{He}(n, \gamma)$ reaction at $E_p=2.30$ MeV.	100
5.14	The deadtime corrected and cosmic ray subtracted <i>gas out</i> spectra.	103
5.15	The corrected <i>gas in</i> spectra.	104
6.1	Measured and calculated values of the cross section for the ${}^3\text{He}(n, \gamma)$ reaction.	110

List of Tables

2.1	Neutron Production Reactions	15
2.2	Radiative Capture Gamma Ray Energies	15
2.3	Ratios of Counts in Peak Regions to Wall Effect Region	22
2.4	Pile-up rates into the region of interest for NaI and BGO	27
5.1	Particulars of each data run	82
5.2	Neutron Production During Data Collection	86
5.3	Fractional Livetime For Each Run	94
5.4	Gamma Ray Production and Detection	105
5.5	Quantities for Computing the Differential Cross Sections	107
5.6	The Differential and Absolute Cross Sections for the ${}^3\text{He}(n, \gamma)$ Reaction . .	107

Chapter 1

Introduction

The radiative capture of fast neutrons on ${}^3\text{He}$ is of interest for several reasons. From a practical point of view, the reaction can be used to produce ~ 21 MeV gamma rays without an accelerator for calibrating medium energy detectors. In terms of fundamental physics, a measurement of the cross section is useful for determining the presence of charge symmetry breaking components in the nuclear force. Both aspects are discussed in more detail below.

The Sudbury Neutrino Observatory (SNO) heavy water Čerenkov detector is presently under construction, and will be used to measure the energy and flavour of solar neutrinos [Ew87, Be89]. The neutrinos will be detected via the three interactions:

$$\nu_e + d \rightarrow p + p + e^- \quad (1.1)$$

$$\nu_x + e^- \rightarrow \nu_x + e^- \quad (1.2)$$

$$\nu_x + d \rightarrow \nu_x + p + n \quad (1.3)$$

where ν_e refers to an electron neutrino, and ν_x refers to a neutrino of any flavour. The Čerenkov radiation emitted by a fast electron will be detected using 20 cm photomultiplier tubes (PMTs) located outside of the heavy water vessel (see Figure 1.1). The fast electrons produced by solar neutrinos via reactions (1.1) and (1.2) will have energies of up to 15 MeV. The energy of the fast electron will be deduced from the number of PMTs that detect the

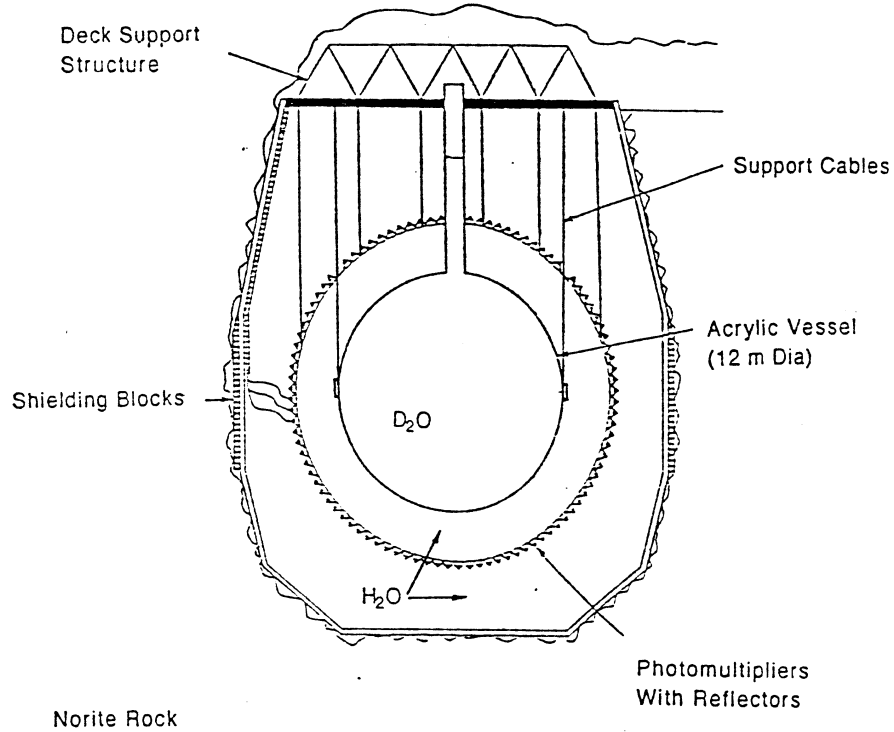


Figure 1.1: The present design of the Sudbury Neutrino Observatory heavy water Čerenkov detector.

Čerenkov light. The time at which each PMT is triggered and its position around the vessel will be used to reconstruct the position and direction of motion of the fast electron within the fiducial volume of the detector. To calibrate the absolute response of the detector, sources that produce fast electrons are required that can be conveniently placed within the heavy water. One such gamma ray source currently under study is based on the radiative capture of fast neutrons on ^3He [Le92]. The gamma rays produced via this reaction have energies $E_\gamma = 20.58 + \frac{3}{4}E_n$, where E_γ and E_n are the gamma ray and neutron energies, respectively, in MeV.

A schematic diagram of such a medium energy gamma ray source is shown in Figure 1.2. A ^{252}Cf fission source provides neutrons with an energy spectrum of the form

$$dN(E_n) = C \sqrt{E_n/T} e^{-E_n/T} dE_n \quad (1.4)$$

where E_n is the neutron kinetic energy in MeV, and $T=1.355$ MeV [Bo82] (see also Figure 1.3). Fast neutrons are required because, due to the prolific ${}^3\text{He}(n, p)$ reaction, high pressure ${}^3\text{He}$ gas is self-shielding against thermal neutrons. The lead surrounding the neutron source is for absorbing the fission gamma rays, and the borated polyethylene serves to moderate and capture neutrons that might otherwise be captured in the heavy water to produce a background of lower energy gamma rays.

The mean free path of the ~ 21 MeV gamma rays from the source is ~ 55 cm in water. A source of gamma rays which is small compared to the mean free path in water would be most useful for testing the reconstruction of the events. Hence, a small, compact volume of ${}^3\text{He}$ gas is required. The compactness is limited by the amount of lead required to attenuate the fission gamma rays, and by the maximum pressure that can be safely stored. To optimize the design of the source, the absolute cross section of the ${}^3\text{He}(n, \gamma)$ reaction must be known. Figure 1.4 shows the values for the fast neutron capture cross section that have been previously measured. Except for one measurement at $E_n=4$ MeV made using a $3'' \times 4''$ NaI crystal [Zu63], the ${}^3\text{He}(n, \gamma)$ cross section has not been previously measured between 70 keV and 6 MeV. However, Figure 1.3 shows that most of the neutrons emitted by the ${}^{252}\text{Cf}$ fission source have energies within the unmeasured range. Hence, more information on the cross section is required for the optimization of the source design.

The cross section $\sigma_{n,\gamma}$ for the ${}^3\text{He}(n, \gamma){}^4\text{He}$ reaction can be calculated from the cross section $\sigma_{\gamma,n}$ for the inverse reaction ${}^4\text{He}(\gamma, n){}^3\text{He}$ using the principle of detailed balance

$$\sigma_{n,\gamma} = \sigma_{\gamma,n} \frac{E_\gamma^2}{3 Mc^2 E} \quad (1.5)$$

where M is the neutron mass, and E and E_γ are the total kinetic energy and gamma ray energy, respectively, in the center-of-mass system [Al80]. The photonuclear reactions ${}^4\text{He}(\gamma, n){}^3\text{He}$ and ${}^4\text{He}(\gamma, p){}^3\text{H}$ have been studied extensively in the search for evidence of

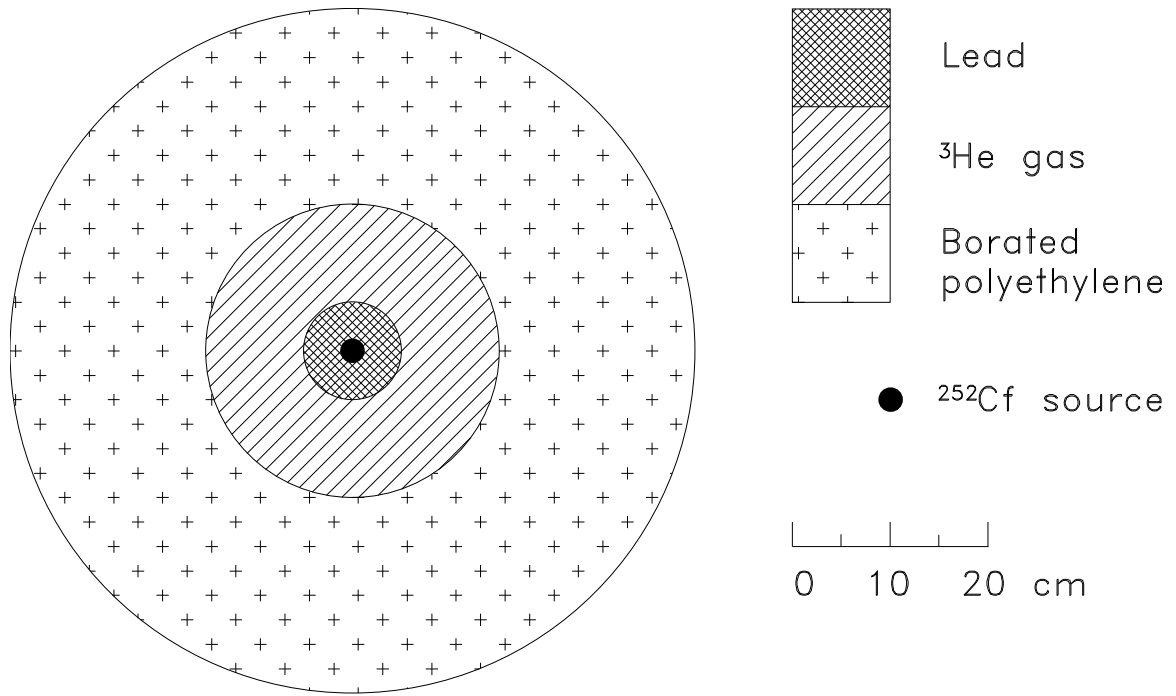


Figure 1.2: A preliminary design for a medium energy gamma ray source based on the $^3\text{He}(n, \gamma)$ reaction.

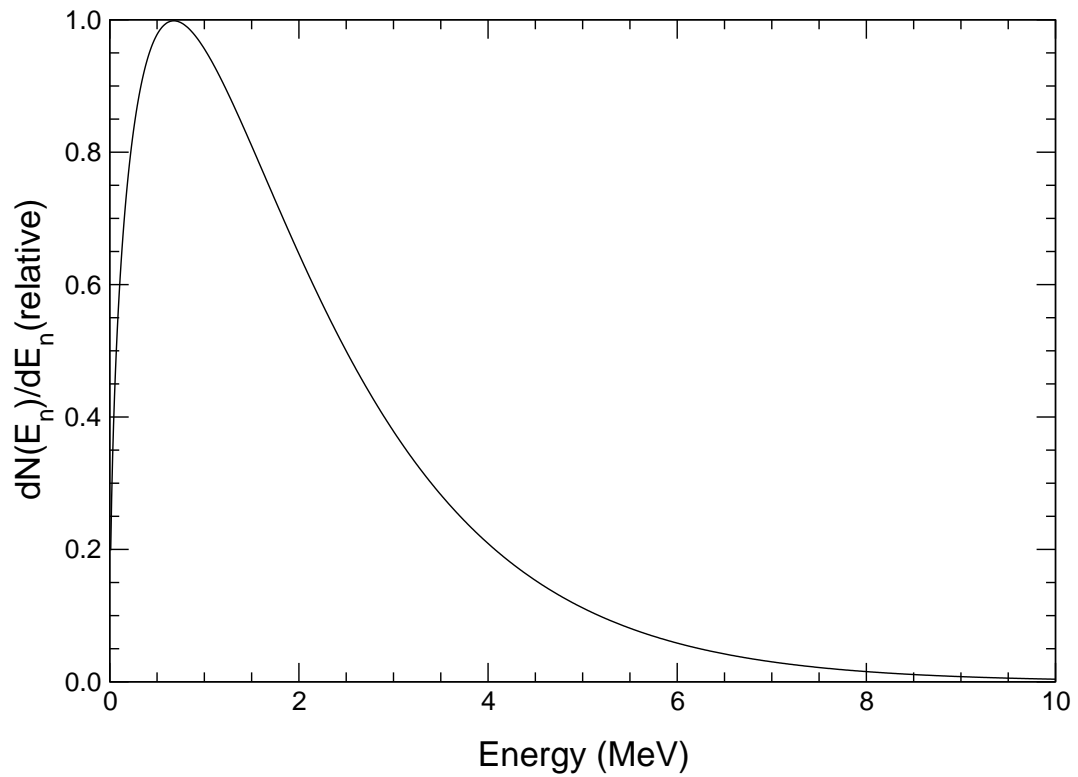


Figure 1.3: The relative neutron energy spectrum from ^{252}Cf , given by eqn.(1.4) [Bo82].

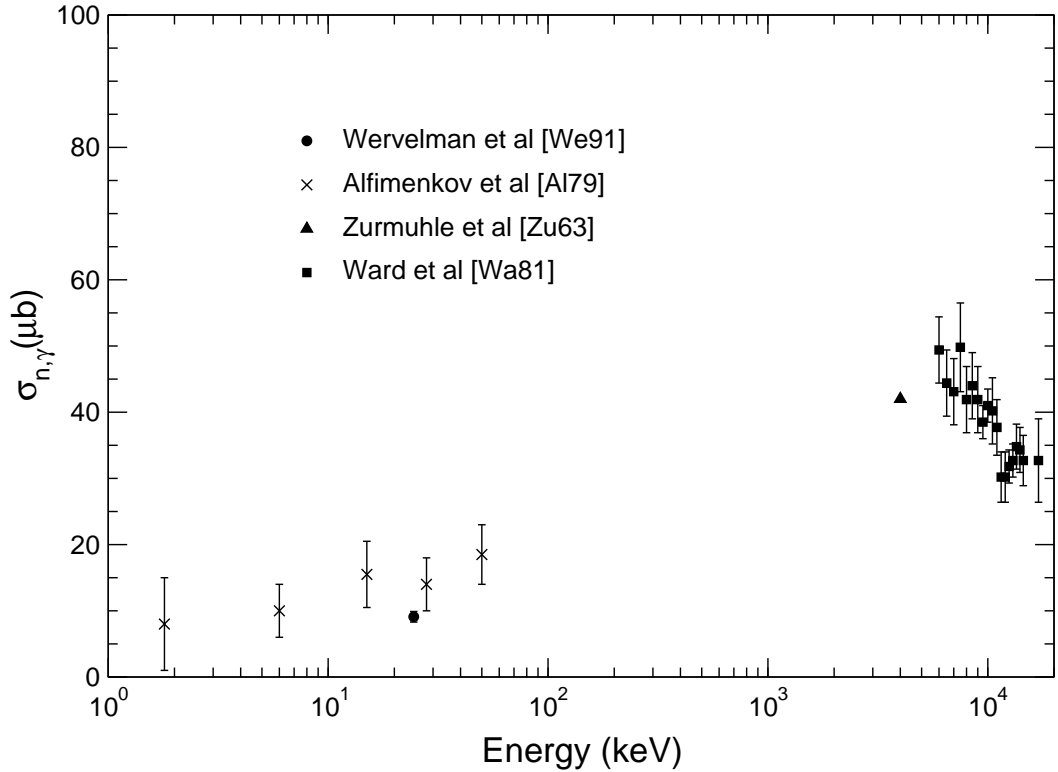


Figure 1.4: The absolute cross section of the ${}^3\text{He}(n, \gamma)$ reaction for fast neutron capture. The uncertainty on the result of [Zu63] is unknown.

charge symmetry breaking in the nuclear force. Barker and Mann [Ba57] first suggested that the ratio of the cross sections for proton and neutron emission from the excited state of a self-conjugate nucleus would depend sensitively on the amount of isospin mixing in the state. In particular, over the region of the isovector giant dipole resonance in ${}^4\text{He}$, conventional theoretical calculations predict the ratio $R = \sigma_{\gamma,p}/\sigma_{\gamma,n}$ to be ~ 1.1 [Ba84, and the references therein] [Wa88]. Many experiments measuring $\sigma_{\gamma,n}$ and $\sigma_{\gamma,p}$ have been performed to test the theory (see [Ti92] and the references therein for a list of the experiments). However, the results of the measurements vary widely, and the experimental situation remains unclear. Calarco *et al.* [Ca83a] reviewed the experimental data obtained before 1983, and made recommendations for $\sigma_{\gamma,p}$ and $\sigma_{\gamma,n}$. The recommended values for $\sigma_{\gamma,n}$ were based on the ${}^3\text{He}(n, \gamma)$ capture data of Ward *et al.* [Wa81], and on the ${}^3\text{He}(\gamma, n)$ measurements of Berman

et al. [Be80] performed using a monoenergetic photon beam, a gas target and a $\sim 4\pi$ neutron detector. The recommended peak value of $\sigma_{\gamma,n}$ was ~ 1.1 mb. The recommended values for $\sigma_{\gamma,p}$ were based on the ${}^3\text{H}(p,\gamma)$ capture data of Perry and Bame [Pe55], McBroom *et al.* [Mc80] and Calarco *et al.* [Ca83b] (see [Ca83b] for a discussion of the (p,γ) data). The recommended peak value of $\sigma_{\gamma,p}$ was ~ 1.8 mb. From the recommended values of the cross sections, the value of R was found to vary between 1.7–1.2 over the energy region $E_\gamma=25\text{--}35$ MeV. Hence, it was suggested by the authors that a charge symmetry breaking component of the nuclear force was responsible for the large value of the ratio.

Recently, Bernabei *et al.* [Be88] measured the ${}^4\text{He}(\gamma,p)$ cross section between $E_\gamma=28.6\text{--}58.1$ MeV in an experiment similar to that of [Be80], that is, using a monoenergetic beam of photons, a gas target and a $\sim 4\pi$ particle detector. The results are substantially lower than the previously recommended values of $\sigma_{\gamma,p}$, agreeing more closely with the previously recommended values of $\sigma_{\gamma,n}$. Feldman *et al.* [Fe90] subsequently measured the ${}^3\text{H}(p,\gamma)$ capture cross section between $E_\gamma=21.3\text{--}31.1$ MeV and found a reduction of $\sim 35\%$ in $\sigma_{p,\gamma}$ as compared to the previously measured results; verifying the results of [Be88]. With the lower values for $\sigma_{\gamma,p}$, and the previously recommended values for $\sigma_{\gamma,n}$, a value of R close to unity is obtained [Be88, Fe90], in agreement with the conventional theoretical predictions for the ratio.

Previous simultaneous measurements of the ratio R have also obtained results consistent with unity. Dodge and Murphy [Do72] measured the ratio of the ${}^4\text{He}(e,{}^3\text{H})$ and ${}^4\text{He}(e,{}^3\text{He})$ cross sections at 90° , and converted the results to get a ratio of the photonuclear cross sections of $R=1.03\pm 0.04$ between $E_x=30.0\text{--}51.8$ MeV. Philips *et al.* [Ph79] measured the ratio of the ${}^4\text{He}(\gamma,{}^3\text{H})$ and ${}^4\text{He}(\gamma,{}^3\text{He})$ cross sections at 90° between $E_\gamma=31\text{--}51$ MeV using bremsstrahlung photons with $E_{\gamma_{max}}=56$ MeV. Spahn *et al.* [Sp89] measured the cross

sections for the ${}^4\text{He}(e, e'p){}^3\text{H}$ and ${}^4\text{He}(e, e'n){}^3\text{He}$ reactions between $E_x=22\text{--}36$ MeV. Recently, Nagornyi *et al.* [Na91] simultaneously measured the ${}^4\text{He}(\gamma, {}^3\text{H})$ and ${}^4\text{He}(\gamma, {}^3\text{He})$ cross sections using a cloud chamber and bremsstrahlung photons with $E_{\gamma_{max}}=150$ MeV. In all cases, the ratio R was found to be in agreement with the conventional theoretical predictions. In a somewhat different measurement, Blilie *et al.* [Bl86] measured the π^+ and π^- inelastic scattering cross sections on ${}^4\text{He}$, and found the ratio of the cross sections to be $R_\pi=1.05\pm 0.08$ between $E_x=23\text{--}30$ MeV. From this, it was deduced that the degree of isospin mixing in the excited states was consistent with the Coulomb interaction being the only charge symmetry breaking force in the nucleus. However, a similar experiment to measure the isospin mixing in the 10.6 MeV giant quadrupole resonance in ${}^{208}\text{Pb}$ [Se86b] produced results in marked disagreement with those from recent measurements using heavy-ion Coulomb excitation [Be90] and electron scattering [Bo88]. Thus, there is some uncertainty as to whether the conclusions drawn from the measurements of [Bl86] are valid.

Although the recent data appear to be consistent, it is not certain that the magnitudes of the photonuclear cross sections are correct. The higher values for the ${}^3\text{H}(p, \gamma)$ cross section from the earlier measurements [Pe55, Mc80, Ca83b] have not been explained. Also, the recent simultaneous measurements of $\sigma_{\gamma,p}$ and $\sigma_{\gamma,n}$ by Nagornyi *et al.* [Na91] yielded results for the cross sections substantially higher than the other recent measurements, with peak cross sections of 1.8 and 1.7 mb for the (γ, p) and (γ, n) reactions, respectively. The results for $\sigma_{\gamma,p}$ reported by [Na91] are in agreement with the earlier capture measurements, and the results for $\sigma_{\gamma,n}$ are in agreement with the results measured by Irish *et al.* [Ir75] using bremsstrahlung photons and a time-of-flight neutron detection system. Figure 1.5 shows the results of some of the measurements of $\sigma_{\gamma,n}$ near the threshold for the reaction, along with some of the results of the (n, γ) measurement of Ward *et al.* [Wa81], and the

recommended cross section of Calarco *et al.* [Ca83a]. A recent measurement of the elastic photon scattering cross section on ^4He by Wells *et al.* [We92] was used to deduce a peak total photoabsorption cross section of 2.86 ± 0.12 mb. At the peak in the giant dipole resonance, the total photoabsorption cross section is well approximated by the sum of $\sigma_{\gamma,p}$ and $\sigma_{\gamma,n}$. The sum of the peak values recommended by [Ca83a] is 2.90 ± 0.16 mb, in agreement with the result of [We92]. The results of [Be88, Fe90] for $\sigma_{\gamma,p}$ and the values recommended by [Ca83a] for $\sigma_{\gamma,n}$ that produce a ratio R consistent with unity, however, sum to a peak value of 2.37 ± 0.13 mb, substantially lower than the result of [We92]. If the photon scattering results are correct, and it is true that the ratio R of the photonucleon cross sections is close to unity, then neither set of photonucleon cross sections is correct. The sum of the peak cross sections measured by [Na91] is ~ 3.5 mb, higher than the result of [We92]. Hence, the experimental situation is still unclear. In their discussion of the measurements, Calarco *et al.* [Ca83a] indicate that the photonucleon measurements are not as accurate near the threshold as at higher energies. This is evident from the scatter in the low energy results shown in Figure 1.5. Thus, the measurements of $\sigma_{\gamma,n}$ are at present too uncertain to provide accurate values in the energy range required for the design of the $^3\text{He}(n, \gamma)$ gamma ray source.

The aim of the present work is to measure the $^3\text{He}(n, \gamma)$ cross section for $E_n=0.14$ – 2.0 MeV (corresponding to photon energies $E_\gamma=20.7$ – 22.0 MeV) to an accuracy of $\sim \pm 10\%$. The cross sections will be used elsewhere [Ur92] for the design optimization of a medium energy gamma ray source which could be used for calibrating the SNO detector. The results will also be used to calculate values for $\sigma_{\gamma,n}$ near the threshold, and thus, will provide a check on the recommended values of [Ca83a].

The experiment was performed at the Queen's University Nuclear Physics Laboratory.

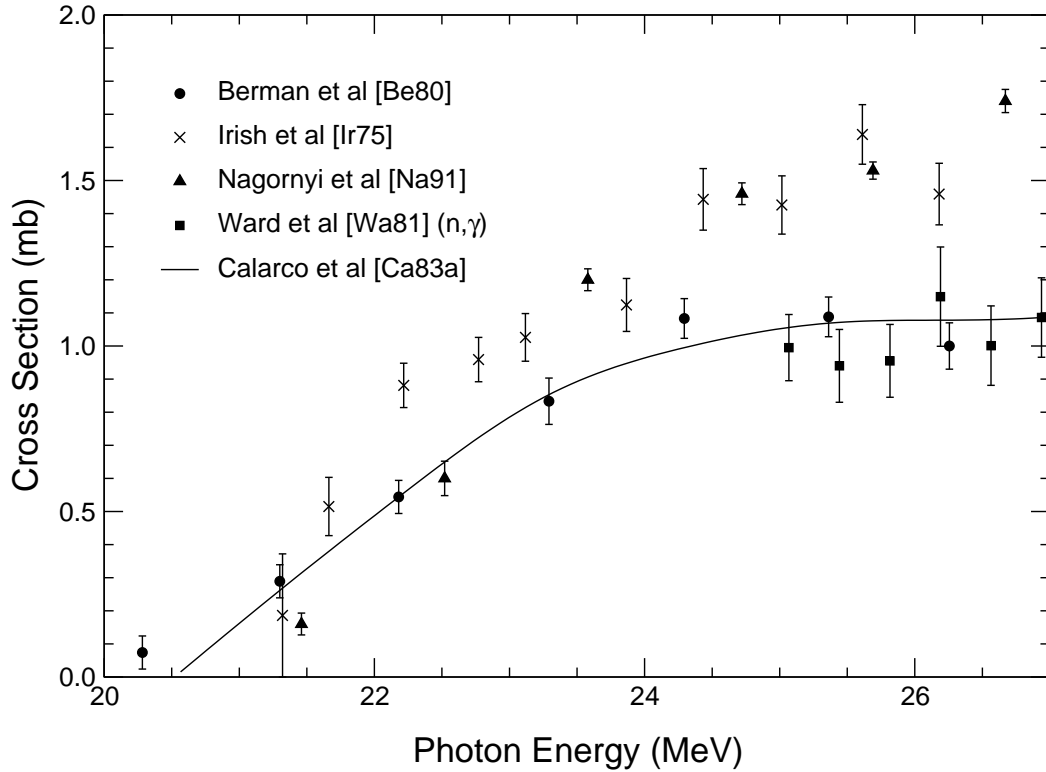


Figure 1.5: Previous results for $\sigma_{\gamma,n}$ near the threshold, along with the recommended values of Calarco *et al.* [Ca83a].

The 4 MeV HVEC Van de Graaff accelerator was used to produce monoenergetic neutrons via the ${}^7\text{Li}(p,n)$ reaction. The ~ 21 MeV gamma rays from the ${}^3\text{He}(n,\gamma)$ reaction were produced in a ${}^3\text{He}$ gas target. The gamma rays were detected in a medium energy gamma ray spectrometer housing a $5'' \times 3''$ bismuth germanate oxide (BGO) scintillator. Due to the small cross section for the reaction ($\sigma_{n,\gamma} \leq 100\mu\text{b}$), contamination of the spectrum by pile-up events is a problem. Hence, the pulses from the scintillator were digitized, and processed digitally to allow pile-up events to be recognized and corrected. The apparatus for the experiment, the digital pulse processing techniques, and the analysis of the data are presented in this report. The results will be discussed in light of the previous measurements of the photonuclear reactions on ${}^4\text{He}$.

Chapter 2

Apparatus

In this chapter, the apparatus used to measure the absolute cross section of the ${}^3\text{He}(n, \gamma)$ reaction is described. First, a brief overview of the entire system is given, followed by a detailed discussion of each component in the system.

2.1 Overview of System

The targets and medium energy gamma ray spectrometer used in the experiment are shown schematically in Figure 2.1. The fast neutrons were produced via the ${}^7\text{Li}(p, n){}^7\text{Be}$ reaction by bombarding lithium evaporated onto tantalum backings with protons from a Van de Graaff accelerator. The ${}^3\text{He}$ gas was placed a distance of 5 cm behind the lithium target at an angle of 0° with respect to the proton beam direction. The beamline and targets were situated about 1 m above the concrete floor, and about 2 m from the nearest wall. Protons at energies of 1930, 2300, 2770, 3220 and 3680 keV were used, producing neutrons with maximum energies of 135, 570, 1070, 1530 and 2000 keV. At each proton energy, a 48 hour run was done with the ${}^3\text{He}$ gas in place, followed by a 24 hour background run with the gas removed.

The medium energy gamma ray spectrometer was placed facing the center of the gas target at an angle of 90° with respect to the proton beam direction. The results of previous

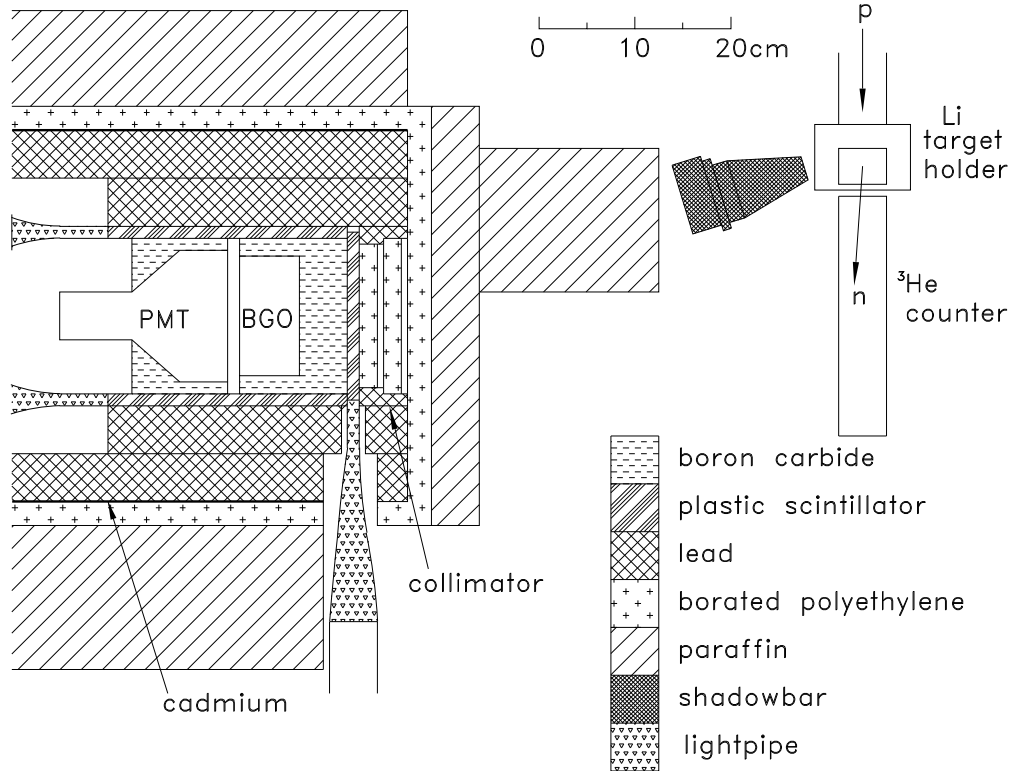


Figure 2.1: Schematic top view of the spectrometer and target systems.

studies of the ${}^3\text{He}(n, \gamma)$ reaction for neutrons in the energy range 10 to 120 keV [A180] and at 9.0 MeV [We82] indicate that the reaction goes predominately by p-wave capture for neutrons in the energy range of the present experiment. Thus, the gamma rays are emitted with an angular distribution that is proportional to $\sin^2 \theta$, where θ is the angle between the directions of motion of the neutron and gamma ray. By positioning the spectrometer at 90° with respect to the beam direction, the gamma ray detection efficiency is maximized.

A 15 cm shadowbar of Mallory 1000 (a high density alloy composed of 90% tungsten and 10% nickel by mass) was placed between the lithium target and the spectrometer to shield the detector from the fast neutrons and gamma rays produced within the target. The shadowbar was removed before and after each run so that the gamma rays produced via the ${}^7\text{Li}(p, \gamma)$ reaction (Q-value of 17.24 MeV) could be used to calibrate the energy response of the detector.

The spectrometer was constructed specifically for the present experiment, and was designed to measure medium energy gamma rays (~ 20 MeV) produced at a low rate in the presence of large fluxes of fast neutrons and gamma rays with energies $E_\gamma \leq 10$ MeV. In such an experiment, the main sources of background, apart from the gamma rays coming from the lithium target, are cosmic ray induced events and pulse pile-up. Typically, the spectrometers used in similar experiments employ a large sodium iodide (NaI) scintillator for efficiently detecting the gamma rays. The crystal is surrounded by more scintillator material for the active suppression of cosmic ray muon events and events where part of the energy has escaped the crystal (to improve the energy resolution of the detector). These scintillators are surrounded by large quantities of passive shielding to reduce the gamma ray and neutron backgrounds, and thus, to reduce the pulse pile-up (see P. Paul [Pa74] and H. Ejiri [Ej89] for examples of such spectrometers).

The spectrometer built for the present experiment houses a 127 mm diameter by 76 mm long bismuth germanate oxide (BGO) scintillator for detecting the gamma rays. The BGO crystal was chosen for its high gamma ray detection efficiency and for its low sensitivity to neutron backgrounds. The crystal is surrounded on five sides by a 13 mm thick plastic veto counter used for suppressing cosmic ray muon events. The scintillators are surrounded on the top and bottom and the two sides by approximately 10 cm of lead to shield them against cosmic ray induced bremsstrahlung and neutron capture gamma rays. There is also approximately 5 cm of lead between the BGO crystal and the ^3He gas target, with a 15 cm diameter hole to collimate the gamma rays entering the spectrometer. Outside of the lead is cadmium, borated polyethylene and paraffin for moderating and capturing neutrons, and the BGO detector is packed in boron carbide powder to further shield it against low energy neutrons. Paraffin was also placed in the space between the

shadowbar and the spectrometer to further moderate the neutrons coming directly from the target. The BGO crystal was situated 60 cm from the center of the ^3He gas target to reduce the neutron flux at the crystal, and to reduce the scattering of neutrons from the heavily shielded spectrometer into the gas target. With these precautions, the count rate in the BGO detector for events above 1 MeV was typically 10-20 kcps (1 kcps = 1000 counts per second), and this kept the counts due to pile-up in the region above 13 MeV at less than 10% of the total.

The decay constant of the light from the BGO crystal is ~ 300 ns, yielding pulses ~ 1.5 μs long from the detector. To reduce the pile-up of pulses, each pulse was clipped to ~ 350 ns using the circuit shown in Figure 2.10 (see page 38). To determine the deadtime of the system, a LED light pulser was constructed to produce green light pulses of known amplitude and with a decay constant similar to those produced in BGO. These pulses were fed into the interface between the BGO crystal and the photomultiplier tube using a fibre-optic cable. The ratio of the number of the LED light pulses detected to the number produced gives the livetime of the whole system directly. The LED light pulser was also used to monitor gain changes in the system.

The data were collected using a Lecroy 9410 digital storage oscilloscope. Each clipped pulse from the BGO detector above ~ 13 MeV that was not vetoed by the cosmic ray suppression shield was digitized at a sampling frequency of 10^8 samples per second over a 2 μs period. The digitized pulses were stored temporarily on high density floppy disks, and were later transferred to a SUN 4/110 computer for off-line analysis. For the analysis, the baseline was subtracted from each pulse, and the remaining shape was fitted with an analytic expression for a single clipped pulse. If the fitted parameters and the chi-square for the fit were within the limits of acceptance for a single pulse, the area under the pulse

(ie. the charge) was calculated and an energy spectrum was incremented. Otherwise, the pulse was re-analysed using a program in which fits to the baseline and to either single or piled-up pulse shapes could be manually controlled and visually inspected. The charges of the corrected pulses were computed and the energy spectrum was incremented.

Some advantages in using such a data collection system are that: i) piled-up pulses can be identified and corrected rather than simply rejected as is the case using pile-up rejectors, ii) afterpulses from the BGO photomultiplier tube can be recognized by their short length and eliminated, iii) baseline restoration circuits that are often used in high-rate experiments are not necessary, and iv) the light pulses from the LED can be recognized and counted for a precise determination of the system livetime. Some of the disadvantages are that the data collection rate is slow (limited to ~ 20 cps by the write time to the floppy disk), large quantities of memory are required to store the pulses (about 7000 pulses are stored on each 1.4 Mbyte floppy disk) and the analysis requires more time than for conventional systems due to the manual correction of the rejected pulses.

Each of the components of the experimental apparatus will now be discussed in more detail.

2.2 Production of Neutrons

The Queen's University Nuclear Physics Laboratory houses an HVEC Van de Graaff accelerator (maximum terminal voltage of 4.0 MV) that is used for producing beams of protons, deuterons and ionized ^3He and ^4He . With such a machine, there are three reactions generally used for producing monoenergetic neutrons in the energy range $120 \text{ keV} < E_n < 6 \text{ MeV}$; the $^7\text{Li}(p, n)$, $^3\text{H}(p, n)$ and $^2\text{H}(d, n)$ reactions. The quantities of interest for each reaction are shown in Table 2.1, as given by [Li75] for the $^7\text{Li}(p, n)$ reaction and by [Li73]

Table 2.1: Neutron Production Reactions

Reaction	Q-value (MeV)	Threshold (MeV)	Q-value (MeV) for radiative capture of incident particle
${}^7\text{Li}(p, n){}^7\text{Be}(\text{g.s.})$	-1.644	1.881 (forward) 1.920 (backward)	17.23
${}^7\text{Li}(p, n_1){}^7\text{Be}(0.43 \text{ MeV})$	-2.075	2.373 (forward) 2.423 (backward)	
${}^3\text{H}(p, n){}^3\text{He}$	-0.764	1.019 (forward) 1.147 (backward)	19.815
${}^2\text{H}(d, n){}^3\text{He}$	+3.269		23.848

Table 2.2: Radiative Capture Gamma Ray Energies

Target Nucleus	E_{incident} (MeV)	E_n (MeV)	E_γ (MeV) from ${}^3\text{He}(n, \gamma)$	E_γ (MeV) from Target
${}^7\text{Li}$	2.90	1.20	21.48	19.76
${}^3\text{H}$	2.00	1.20	21.48	21.32
${}^2\text{H}$	0.50	3.51	23.21	24.10

for the ${}^3\text{H}(p, n)$ and ${}^2\text{H}(d, n)$ reactions.

As can be seen from the Q-values listed in the table, the radiative capture of the incident particles in each of the primary targets produces gamma rays of similar energy to those produced in the ${}^3\text{He}(n, \gamma)$ reaction (Q-value of 20.58 MeV). The cross sections for the radiative capture of the incident particles are of the same order of magnitude as that for the ${}^3\text{He}(n, \gamma)$ reaction. Table 2.2 gives some examples of the gamma ray energies produced in the three types of targets under some typical conditions. The gamma rays produced in the ${}^3\text{H}$ and ${}^2\text{H}$ targets are very close in energy to those produced in the ${}^3\text{He}$ gas target, hence, the use of the ${}^3\text{H}(p, n)$ and ${}^2\text{H}(d, n)$ reactions for producing neutrons was rejected. The gamma rays from the lithium target, however, are low enough in energy to permit the experiment to be done with a spectrometer of moderate energy resolution provided that a shadowbar is placed between the lithium target and the spectrometer to attenuate the background gamma rays.

As can be seen in Table 2.1 above, monoenergetic neutrons are produced only between proton energies of 1.92 and 2.37 MeV using the ${}^7\text{Li}(p, n_0){}^7\text{Be}(\text{g.s.})$ reaction. Above 2.37 MeV, a second group of neutrons is produced through the ${}^7\text{Li}(p, n_1){}^7\text{Be}(0.43 \text{ MeV})$ reaction. The intensity of the second group in the forward direction (into the ${}^3\text{He}$ gas target) is relatively weak, never exceeding $\sim 12\%$ of that of the first group over the energy range of the present experiment. Corrections for the effects of this second group were made, as described in Section 5.5.

The targets were prepared by evaporating natural lithium in a vacuum onto 0.5 mm tantalum backings. The thickness of the lithium layer was typically 100–120 $\mu\text{g}/\text{cm}^2$, as measured using a calibrated quartz crystal. Since lithium metal is highly reactive with water, a layer of gold (typically $\sim 20 \mu\text{g}/\text{cm}^2$) was evaporated over the lithium to protect it during the transfer from the evaporation chamber to the beamline. The targets were prepared in pairs, one for the ${}^3\text{He}(n, \gamma)$ measurement, and the other for the background measurement. Upon removal from the evaporation chamber, each target was mounted using indium metal seals in a stainless steel target holder and quickly placed in the beamline for vacuum pumping. The target holder was designed to facilitate the speed at which the transfer was made. Figure 2.2 shows the end of the beamline in detail. To collect any sputtered ${}^7\text{Be}$ atoms, the target arrangement was lined with aluminum foil that could be removed for activity measurements after each run. To reduce the evaporation of lithium, the target was water cooled and the proton beam was defocussed to a ~ 5 mm spot. Proton beam currents in the range of 13 to 17 μA were used. An electron suppressor held at -200 V was placed between the target holder and the beam collimator to reduce the loss of secondary electrons from the target arrangement.

After each ${}^3\text{He}(n, \gamma)$ or background run the lithium target was removed for measure-

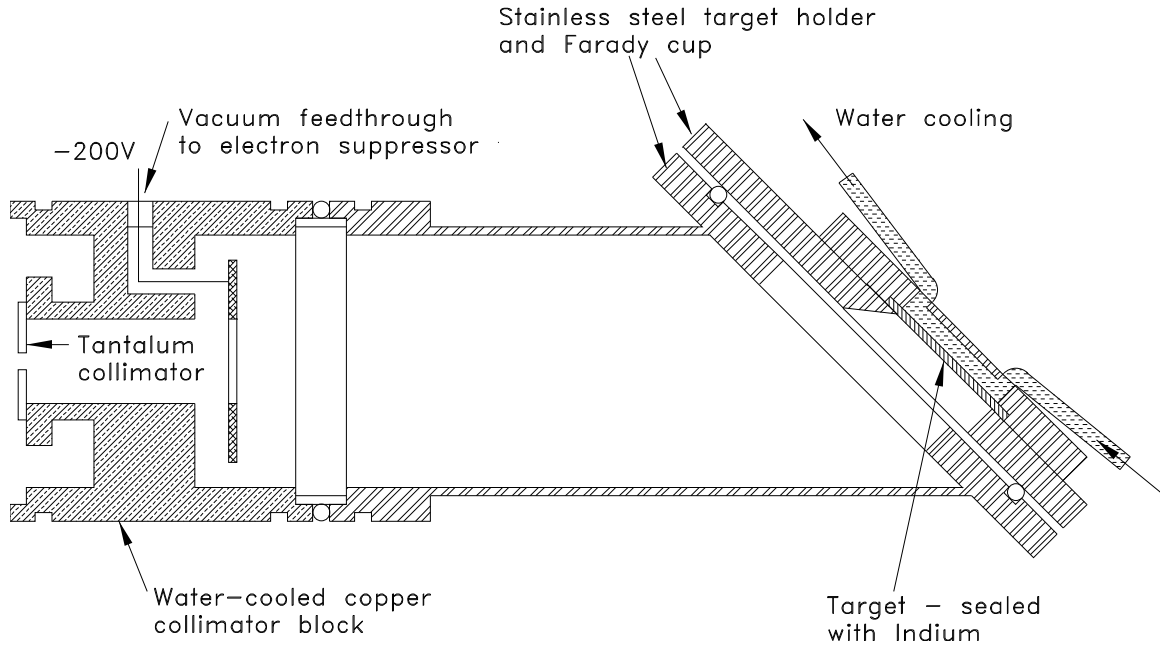


Figure 2.2: Cut-away diagram of the target system at the end of the beamline. For clarity, the fasteners have not been shown.

ments of the ${}^7\text{Be}$ activity. The ${}^7\text{Be}$ produced in the targets decays by electron capture with a half-life of 53.3 d, 10.52% of these decays being to the first excited state of ${}^7\text{Li}$ at 478 keV [Aj88]. The activity of 478 keV gamma rays from each target was measured using a HPGe counter whose absolute efficiency was determined using calibrated sources. The total number of neutrons produced during each experiment was determined from these measurements. The fraction of the neutrons entering the ${}^3\text{He}$ target was calculated using the angular distributions for the ${}^7\text{Li}(p, n)$ reaction provided in the compilation of H. Liskien and A. Paulsen [Li75]. The activities of the aluminum liners were also measured to account for any sputtered ${}^7\text{Be}$ atoms, and were typically less than 1% of the total ${}^7\text{Be}$ activity. The results of the activity measurements were checked against the expected results calculated using the ${}^7\text{Li}(p, n)$ cross sections of [Li75] and the measured target thicknesses, and were found to be in agreement within the $\sim 15\%$ accuracy of the calculations.

During installation in the beamline, discolouration of all of the targets was noted to

some degree, indicating that there was contamination of the targets from water vapour in the air. For the target thicknesses and proton energies used in the experiment, the calculated proton energy loss through pure lithium targets is in the range of 14 to 20 keV (calculated using the stopping powers given by J.F. Janni [Ja82]). A small amount of contamination by water would slightly increase the proton energy loss through the target, and hence, increase the neutron energy spread. However, it will have little effect on the neutron intensity if the added energy loss is on the order of a few keV [Li75]. Evidence that the contamination did not seriously affect the results comes from the lowest energy run. For 1930 keV protons and a $\sim 100 \mu\text{g}/\text{cm}^2$ target placed at 45° to the beamline, the energy loss through the lithium layer is about 20 keV. Small amounts of water react with lithium through the reaction [Do87]



Protons with 1930 keV of kinetic energy traversing a pure LiOH layer with a lithium density of $100 \mu\text{g}/\text{cm}^2$ would lose about 50 keV, and they would lose about 130 keV if $\text{LiOH}\cdot\text{H}_2\text{O}$ was formed in the target. However, the neutron production rate drops sharply at 1890 keV (ie. above the threshold for the reaction) [Li75]. The number of neutrons produced in the 48 hour run with 1930 keV protons was $(5.149 \pm 0.048) \times 10^{13}$, as deduced from the measurement of the ^7Be activity (see Section 5.2). The total number can also be estimated using the $^7\text{Li}(p, n)$ cross sections from [Li75]. The total charge of protons on the target was 2.712 C, and assuming a pure lithium target $100 \pm 10 \mu\text{g}/\text{cm}^2$ thick with a 92.6% abundance of ^7Li , the expected number of neutrons produced is $(5.2 \pm 0.7) \times 10^{13}$. The expected number agrees with the measured number, indicating that the proton energy loss was probably less than 40 keV through the target, and that the water contamination was not serious.

2.3 ^3He Gas Target

The gas target was a ^3He proportional counter purchased from LND, Inc. of Oceanside, New York. The counter is of the simple cylindrical type, 5.0 cm in diameter and 25 cm long. The fill gas is a mixture of ^3He and CO_2 at partial pressures of 19.4 atm and 0.6 atm, respectively, at 70 °F. The manufacturer claims that their device for measuring pressures is accurate to $\pm 0.1\%$. The walls of the counter are made from 0.5 mm stainless steel. The ^3He counter was encased in 1.2 mm of cadmium metal to shield it from thermal neutrons.

The ^3He counter in its cadmium casing was suspended 5 cm from the lithium target with its axis aligned along the beam direction. Following each 48 hour run with the counter in place, a 24 hour run was done with the gas counter removed to measure the backgrounds. The cadmium casing was left in place during these runs, with the ^3He counter replaced by an equal mass of steel pipe.

The ^3He proportional counter was not used for monitoring the neutron production rate during the experiment for two reasons. The first reason is that the counter could not be used for monitoring when it was removed during the background runs. Secondly, the pulse pile-up from the counter would have been too severe. Due to the counter's large diameter and high gas pressure, the pulses from the counter must be integrated with at least a $10\ \mu\text{s}$ time constant to obtain the best energy resolution. This limits the pulse rate to ≤ 1 kcps for a pile-up free spectrum. However, experiments done with thin lithium targets and low beam currents indicate that count rates in excess of 100 kcps could be expected during the $^3\text{He}(n, \gamma)$ data collection runs. Hence, to avoid this pulse pile-up problem and to enable monitoring during the background collection runs, a Bonner sphere, placed 90 cm away from the target at a backward angle of 110° with respect to the beam direction, was used to monitor the neutron flux.

The ^3He proportional counter was used to measure the effects of the passive shielding on the neutron energy distribution in the gas target. The $^7\text{Li}(p, n)^7\text{Be}(\text{g.s.}+0.43 \text{ MeV})$ reaction was used to produce 2.0 and 1.5 MeV neutrons in the forward direction. The shielding geometry was changed in an effort to produce measurable differences in the neutron energy spectra. To reduce the pile-up for these measurements, thin targets and low beam currents of $\sim 0.05 \mu\text{A}$ were used to produce count rates of ~ 100 cps in the counter. Due to the water cooling of the target and collimators, a variable background current of $\sim 0.005 \mu\text{A}$ was present, resulting in an uncertainty of $\sim 10\%$ on the charge integration measurements. Hence, rather than trying to measure differences in each spectrum for a fixed charge of protons on the target, differences in the shapes of the spectra were looked for to indicate changes in the neutron energy distributions.

To determine the effects of the hydrogenous materials (ie. paraffin, polyethylene and concrete), a measurement of the neutron energy spectrum was done with the usual geometry, and with the ^3He counter placed 15 cm from the lithium target along the beam axis to increase the ratio of scattered neutrons to neutrons coming directly from the target. The two spectra are shown in Figure 2.3. The fraction of the counts in the epithermal peak increased as the ^3He counter was pulled back, however, the shape of the spectrum for fast neutron capture is unchanged, indicating that the neutrons scattered from the hydrogenous materials are well moderated. These thermalized neutrons do not contribute to the $^3\text{He}(n, \gamma)$ reaction because those that strike the counter are absorbed by the cadmium ($\Sigma_{n_{th}, \gamma} \simeq 114 \text{ cm}^{-1}$), or by the ^3He through the prolific $^3\text{He}(n, p)^3\text{H}$ reaction ($\Sigma_{n_{th}, p} \simeq 2.3 \text{ cm}^{-1}$).

Fast neutrons are scattered into the gas target by the shadowbar. To determine the contribution of these neutrons to the total spectrum, spectra were measured for i) the usual geometry, ii) the shadowbar removed from the arrangement, and iii) an extra

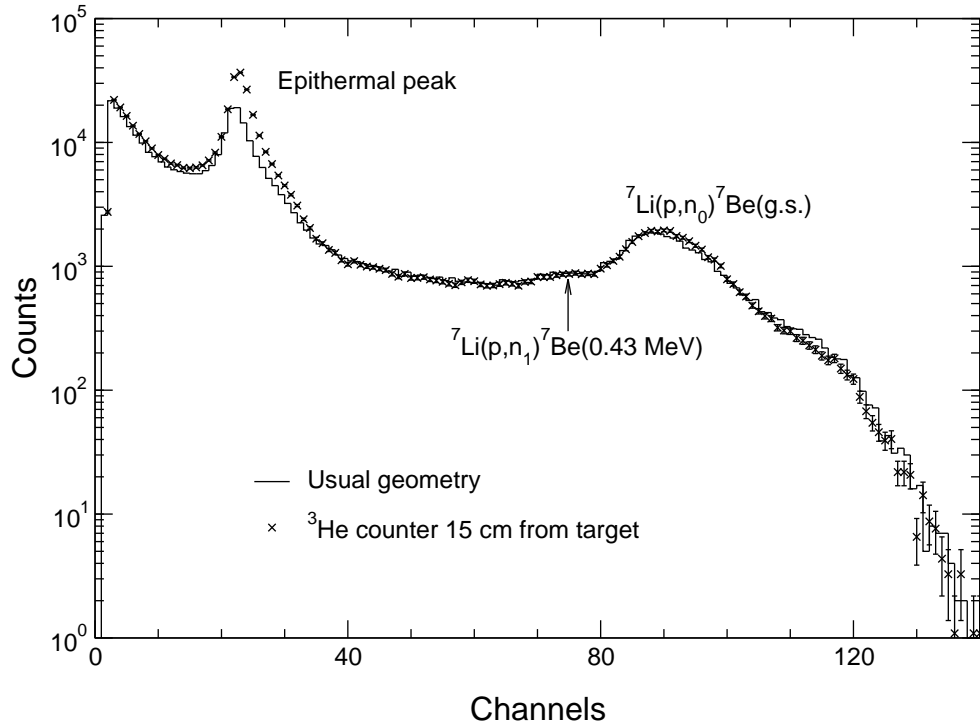


Figure 2.3: Neutron energy spectra corresponding to different positions of the gas target.

shadowbar placed on the opposite side of the target to double the contribution of the scattered neutrons. The results are shown in Figure 2.4, along with the definition of three regions of interest in the spectra. These are: (1) the capture peak for neutrons produced by the ${}^7\text{Li}(p, n_0){}^7\text{Be}(\text{g.s.})$ reaction, (2) the capture peak for neutrons produced by the ${}^7\text{Li}(p, n_1){}^7\text{Be}(0.43 \text{ MeV})$ reaction, and (3) the region where only a fraction of the initial neutron energy is deposited in the gas. Counts in the latter region are due to the capture of partially moderated neutrons, recoiling ${}^3\text{He}$ nuclei produced by the elastic scattering of neutrons, and by the *wall effect* (ie. where the proton or triton from the ${}^3\text{He}(n, p){}^3\text{H}$ reaction in the counter strikes a wall before depositing the full reaction energy into the gas [Kn89, pages 487-490]). The shadowbar is placed at 73° with respect to the beam direction, and the neutrons from the ${}^7\text{Li}(p, n_0){}^7\text{Be}(\text{g.s.})$ reaction emitted in this direction have an energy of 1.5 MeV. If these neutrons are elastically scattered into the gas counter,

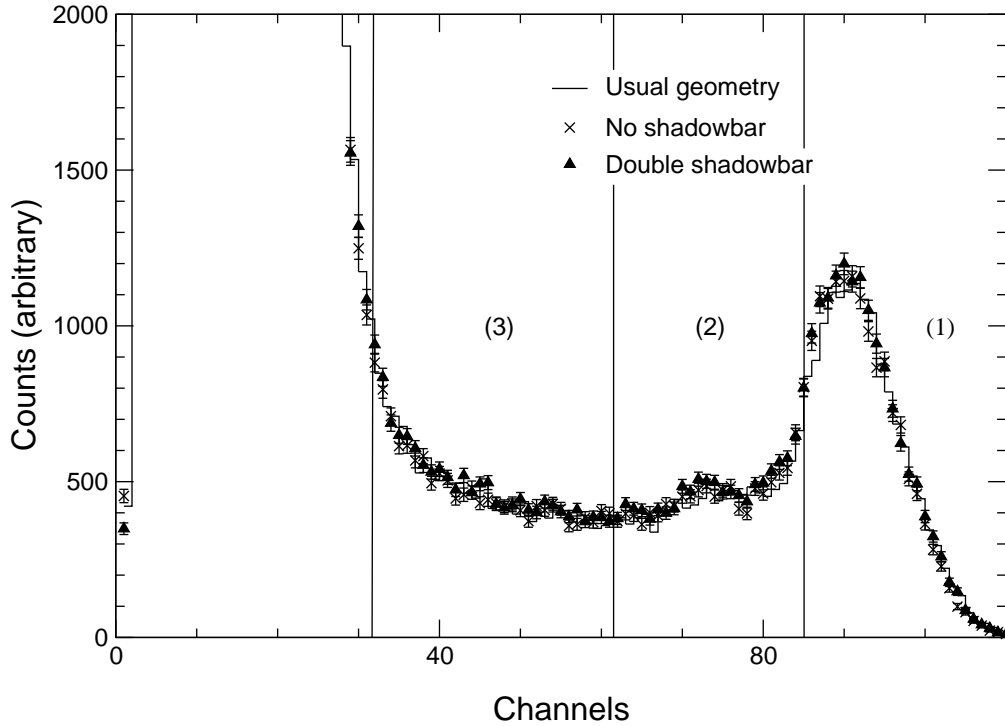


Figure 2.4: Neutron energy spectra for three arrangements of shadowbars

Table 2.3: Ratios of Counts in Peak Regions to Wall Effect Region

Geometry	$\frac{\text{Counts in (3)}}{\text{Counts in (1)}}$	$\frac{\text{Counts in (2)}}{\text{Counts in (1)}}$
No shadowbar	0.724 ± 0.009	0.683 ± 0.009
Usual	0.736 ± 0.009	0.694 ± 0.009
Double shadowbar	0.725 ± 0.009	0.690 ± 0.009

they will contribute to the counts in the region of the capture peak of the neutrons from the ${}^7\text{Li}(p, n_1){}^7\text{Be}(0.43 \text{ MeV})$ reaction. The ratios of the counts in the regions are shown in Table 2.3, and indicate that the shapes of the spectra are identical within statistical uncertainties.

The proportional counter captures neutrons through the ${}^3\text{He}(n, p)$ reaction, which has a cross section that scales with energy as $\sim E_n^{-1/2}$. The cross section for the ${}^3\text{He}(n, \gamma)$ reaction over the energy range of interest increases as $\sim E_n^{1/2}$. Hence, the measurements of the neutron energy spectra are more sensitive to the lower energy neutrons than the

measurements of the gamma ray spectra are. Since no significant indications of neutron scattering into the gas target were seen with the proportional counter, the contribution of these neutrons to the ${}^3\text{He}(n, \gamma)$ reaction is assumed to be negligible.

2.4 The Medium Energy Gamma Ray Spectrometer

The spectrometer was designed and built specifically for measuring the absolute cross section of the ${}^3\text{He}(n, \gamma)$ reaction. The design of the apparatus was driven by the four following requirements:

i) the energy resolution should be good enough to resolve the gamma rays from the ${}^3\text{He}(n, \gamma)$ and ${}^7\text{Li}(p, \gamma)$ reactions, that is, $\Delta E/E \leq 8\%$ at $E=20$ MeV.

ii) a high efficiency detector is required as the ~ 20 MeV gamma rays from the ${}^3\text{He}(n, \gamma)$ reaction are produced at rates of approximately one per second in the present experiment.

iii) the intensity of low energy (≤ 10 MeV) neutron capture gamma rays is typically many orders of magnitude greater than the signal intensity. To reduce the pile-up of these gamma rays the detector should be fast, it should be shielded against capture gamma rays produced outside of the spectrometer, and the spectrometer itself should be constructed from materials that have low radiative capture cross sections or only produce low energy gamma rays from (n, γ) reactions.

iv) the cosmic ray induced background in the gamma ray detector should not exceed a rate of a few counts/MeV/hr in the 20 MeV energy region.

The individual components of the spectrometer are described below along with a brief justification for their choice in light of the design criteria given above.

2.4.1 The Gamma Ray Detector

The requirements for fast signals and a high detection efficiency eliminate germanium detectors as a choice for the gamma ray detector. In the past, sodium iodide (NaI) scintillator has been used extensively (examples of such spectrometers are given by H. Ejiri [Ej89] and by P. Paul [Pa74]). Recently, however, bismuth germanate oxide ($\text{Bi}_4\text{Ge}_3\text{O}_{12}$, or BGO) scintillator is being used in place of NaI for detecting medium energy gamma rays (see, for example, the report by Corvisiero *et al.* [Co90]). A BGO scintillator was chosen for the present experiment, and the reasons for this are given below.

The mean free path for 20 MeV gamma rays in NaI and BGO is 6.1 cm and 2.8 cm, respectively [St70]. To contain the total gamma ray energy, NaI crystals used in medium energy gamma ray spectrometers are typically 25 cm in diameter and 25 to 30 cm long. Due to the shorter mean free path in BGO, the same intrinsic detection efficiency can be achieved using BGO crystals ten times smaller in volume than the typical NaI crystals. There are some important advantages to using smaller BGO crystals, as will be shown below.

The rate at which cosmic ray muons pass through a crystal is roughly proportional to its surface area, hence, this background rate will be about four times lower in the BGO crystal. As the density of BGO is roughly twice that of NaI, through going muons will deposit roughly the same amount of energy in a BGO crystal as in a NaI crystal that is twice the size. Thus, the number of counts/MeV/hr in the BGO detector will be about four times lower than that in a NaI detector that has an equal intrinsic gamma ray detection efficiency.

The main disadvantage of using a BGO detector is that the signal amplitude from the photomultiplier tube is considerably smaller than that obtained using a NaI crystal [Ha86].

Thus, for low energy gamma ray detection where the pulse variations are dominated by photon counting statistics, the energy resolution of a BGO detector is poorer than that of a NaI detector. For 662 keV gamma rays, typical resolutions are 14% for BGO and 7.5% for NaI detectors [Ha86]. However, medium energy gamma rays produce enough light that the resolution of a large BGO or NaI detector becomes dominated by energy losses due to escaping radiation from the crystal and by non-uniformities in the light collection. Hence, for energies above ~ 20 MeV, the energy resolutions of the two types of scintillator become comparable.

The scintillation light output from NaI and BGO crystals decays exponentially with a time constant of ~ 230 ns and ~ 300 ns, respectively, hence, the pulses from photomultiplier tubes coupled to these crystals are typically ~ 1.5 μ s long. These pulses can be clipped shorter using delay line techniques [Kn89, pages 578–580] or with passive RLC filters [Am69] to allow count rates of up to several 100 kcps. NaI is marginally faster than BGO, but either scintillator decays quickly enough for the present experiment. However, due to the low light output from BGO crystals, good energy resolution with a BGO detector can only be achieved if a photomultiplier tube with a high photoelectron collection efficiency is used. This high efficiency comes at the expense of good timing resolution as photoelectrons with widely varying flight paths, and thus flight times, must be collected. The resulting slower risetime (typically ~ 50 ns) means that the resolving time for rejecting pile-up events is poorer than for a NaI detector with fast photomultiplier tubes, where the resolving time can be as short as 15 ns [Bl68]. However, it will be shown below that the lower background rates in the BGO detector result in a lower overall pile-up rate.

The thermal neutron capture rate per unit volume in BGO is less than one quarter of that in NaI [Dr81]. Häusser *et al.* [Ha83] indicate that, for neutrons below 0.5 MeV, the

capture rate per unit volume is at least ten times lower in BGO than in NaI, and the rates become roughly equal over a neutron energy range of 4 to 10 MeV. Thus, for a BGO crystal that is one tenth the volume of a NaI crystal, the neutron capture rate for $E_n \leq 0.5$ MeV will be at least one hundred times lower in the BGO, and the capture rate of fast neutrons will be at least ten times lower. A disadvantage of BGO over NaI is that the maximum energy that can be released in neutron capture is higher in BGO. The Q-value for the radiative capture of neutrons on ^{73}Ge is 10.20 MeV, while that for the capture on ^{127}I is 6.83 MeV [Go72]. Since these reactions take place within the crystals, it is probable that the whole of the energy will be absorbed in each case. The signal from the $^3\text{He}(n, \gamma)$ reaction (~ 21 MeV) can be mimicked by the pile-up of two 10.2 MeV events in the BGO detector, and by the pile-up of three 6.83 MeV events in the NaI detector. A simple calculation shows that the triple pile-up rate in NaI exceeds the double pile-up rate in BGO at a low neutron flux. Assuming a typical size for the NaI detector of 25 cm in diameter and 25 cm long, and a typical size for the BGO detector of 12.5 cm in diameter and 10 cm long, the neutron capture rates in ^{127}I and ^{73}Ge are 29682ϕ and $87.3\phi \text{ s}^{-1}$, respectively, where ϕ is the thermal neutron flux ($\text{cm}^{-2}\text{s}^{-1}$). The rates are calculated using the thermal cross sections and resonance integrals from [Nu89], and assuming a E^{-1} dependence for the flux. Using a resolving time for pile-up rejection of 15 ns for the NaI detector and 50 ns for the BGO detector, the pile-up rate into the region of interest for both detectors is shown in Table 2.4 as a function of the thermal neutron flux. The triple pile-up rate in the NaI exceeds the double pile-up rate in the BGO when the pile-up rate exceeds 0.55 counts/day. Thus, the pile-up rate into the region of interest is higher for the BGO detector only when the rate is practically negligible.

Because a BGO detector can be made physically smaller than a NaI detector, less

Table 2.4: Pile-up rates into the region of interest for NaI and BGO

ϕ ($\text{cm}^{-2}\text{s}^{-1}$)	Pile-up rate in NaI (counts/day)	Pile-up rate in BGO (counts/day)
0.01	2.54×10^{-4}	3.29×10^{-3}
0.1	2.54×10^{-1}	3.29×10^{-1}
1	2.54×10^2	3.29×10^1
10	2.53×10^5	3.29×10^3
100	2.43×10^8	3.29×10^5

active shielding is needed for vetoing cosmic ray muons or events where some of the energy escapes from the crystal, and less passive shielding is needed to reduce cosmic ray induced radiation such as bremsstrahlung or knock-on protons and electrons. The smaller radiative capture cross sections in BGO also mean that less shielding is needed to moderate and capture neutrons before they enter the crystal. Hence, a spectrometer with a BGO detector can be made physically smaller than one with a NaI detector. Apart from the obvious advantage in cost, a smaller spectrometer can be placed closer to the gamma ray target without seriously affecting the neutron flux there. By increasing the solid angle subtended by the smaller detector in this way, comparable absolute efficiencies for measuring medium energy gamma rays can be obtained between the two types of scintillator, along with lower neutron capture backgrounds in the spectrometer with the BGO detector.

For the present experiment, a 127 mm diameter by 76 mm long BGO crystal was purchased from Harshaw/Filtrol. The crystal is coupled to a SRC 125B01 127 mm diameter photomultiplier tube produced by A.D.I.T. Co. (New England). This photomultiplier tube is the slow, efficient type, with a signal risetime of ~ 60 ns. The photomultiplier tube is surrounded by μ -metal for magnetic shielding. The pulse height resolution is 12.5% for 662 keV gamma rays, which is relatively good for a BGO detector. The intrinsic efficiency of the bare crystal for detecting medium energy gamma rays was calculated using the Monte Carlo simulation described in Section 4.1.3. For a point source of 10.76 MeV gamma rays

situated on the axis of the crystal a distance of 30 cm from the face, the calculated intrinsic efficiency for counts between 9.0 and 11.5 MeV is $0.581 \pm 0.001(\text{stat})$. For a similar source of 20 MeV gamma rays, the calculated intrinsic efficiency for counts between 18.0 and 21.0 MeV is $0.437 \pm 0.001(\text{stat})$. The calculated response functions for both gamma ray energies are shown in Figure 2.5.

2.4.2 Active Shielding

The BGO detector is enclosed in a five-sided box of 13 mm thick plastic scintillator (NE102a) for suppressing cosmic ray muon events (see Figure 2.1). Assuming a probable energy loss of ~ 1.7 MeV/cm [Cr64], muons that pass through the BGO crystal leave at least 2 MeV electron equivalent energy in the plastic scintillator (i.e. they produce at least as much light in the scintillator as a 2 MeV electron). If a signal corresponding to an event where more than 0.57 MeV electron equivalent energy is deposited in the plastic scintillator is detected within ± 70 ns of a signal above the threshold from the BGO detector, a blocking signal is produced that inhibits the processing of the BGO detector's signal (see Section 2.4.4 for details on the electronics). In this way, most of the events produced by muons passing through the BGO crystal are actively vetoed.

The response functions of one of the scintillators to gamma rays from a ^{22}Na and a ^{137}Cs source are shown in Figure 2.6. The gamma rays interact predominately by Compton scattering in the plastic. The maximum Compton electron energy is $E_c = 2E_\gamma^2 / (0.511 + 2E_\gamma)$; E_γ in MeV. Guided by the results of Cherubini *et al.* [Ch89], it was assumed that E_c was located about 5% above the maximum in the Compton distribution. Under this assumption, the energy scale was calibrated using the 511, 662 and 1275 keV gamma rays, and the discriminator level for operation of the active shield was set at an electron equivalent energy of ~ 570 keV. This value was chosen for several reasons:

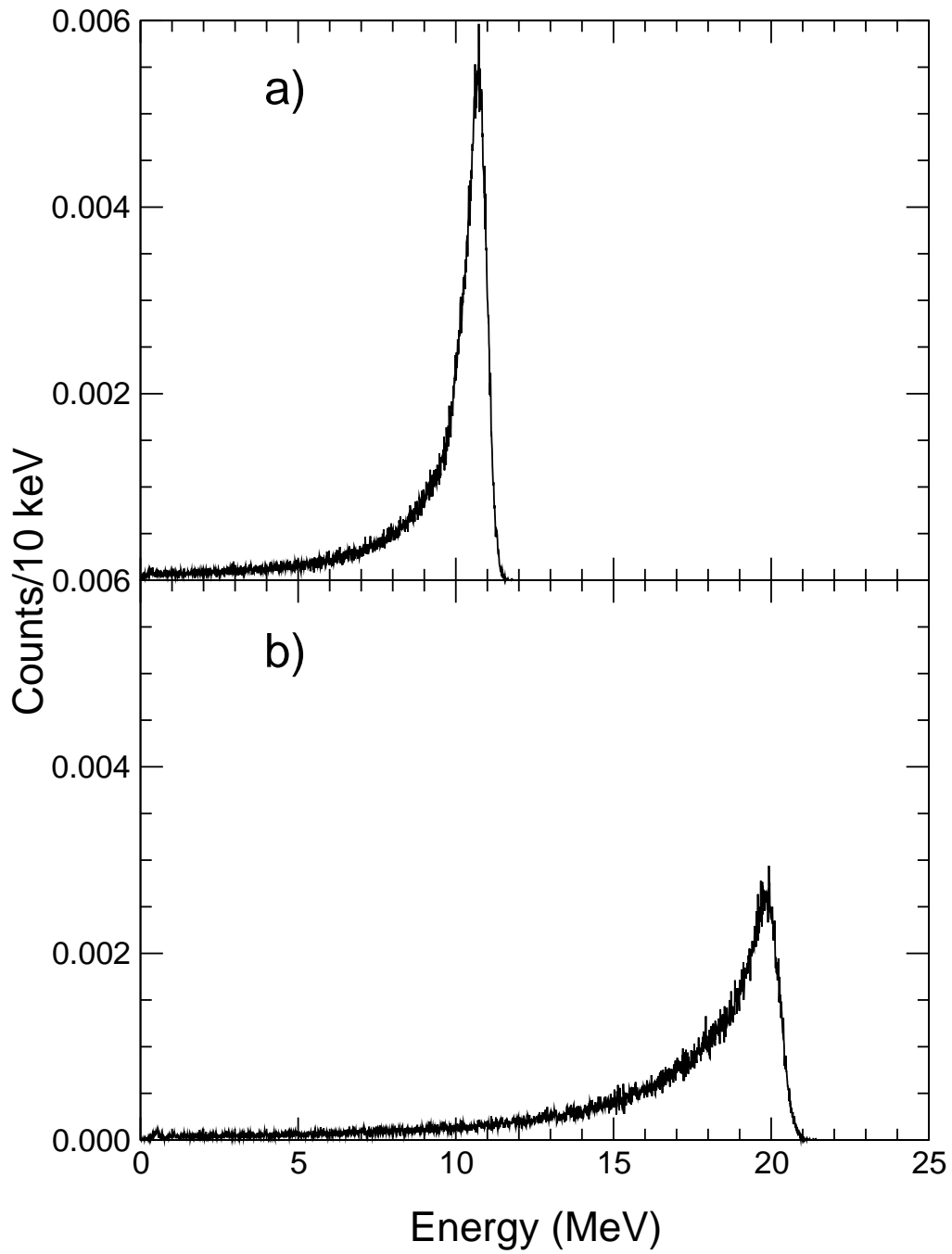


Figure 2.5: The calculated response functions for point sources of a) 10.76 MeV and b) 20.0 MeV gamma rays situated 30 cm from the front face of a bare 127 mm by 76 mm BGO crystal.

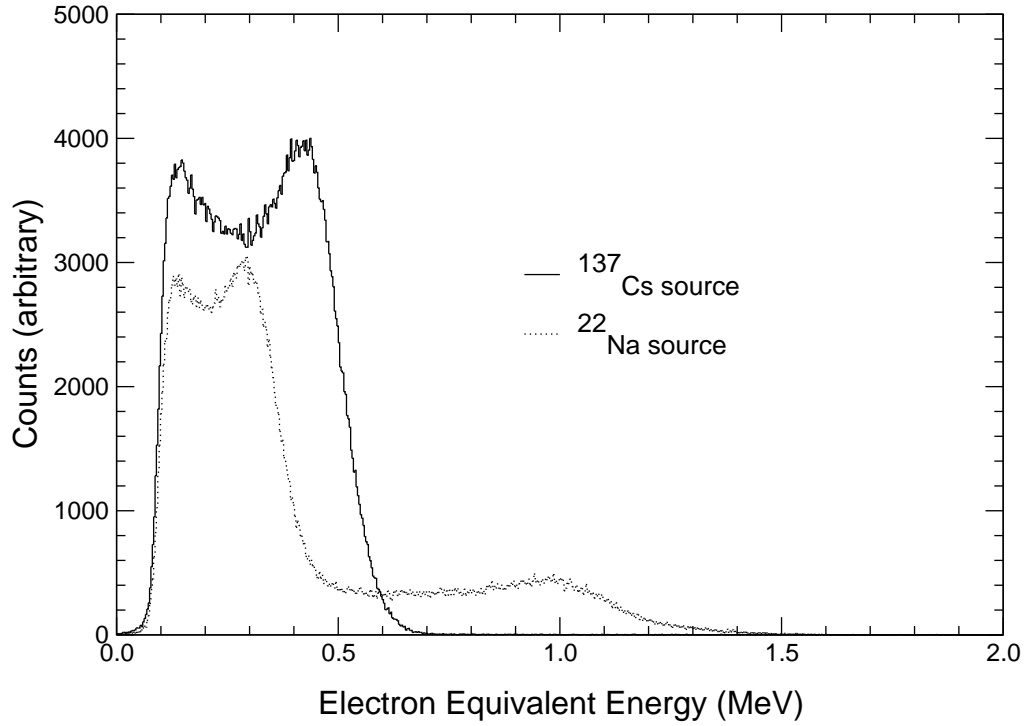


Figure 2.6: The response function of the plastic scintillator to gamma rays from a ^{22}Na and a ^{137}Cs source.

i) Muons that pass through the BGO crystal are expected to deposit at least 2 MeV electron equivalent energy in the plastic scintillator. Even allowing for the statistical nature of the light production, collection and conversion, most muons should produce signals greater than 570 keV electron equivalent energy, making the active shield efficient at suppressing these events.

ii) The shield is insensitive to gamma rays with energies ≤ 660 keV. In particular, the background of 478 keV gamma rays produced via the $^{10}\text{B}(n,\alpha)^7\text{Li}^*$ reaction in the boron carbide powder packed around the BGO detector, and the 511 keV gamma rays that might escape from the BGO crystal will not be likely to veto events. The fast pulses from the plastic scintillator (~ 25 ns long) make pile-up unlikely.

iii) Hydrogen nuclei that are scattered by neutrons in the plastic scintillator are unlikely to produce light pulses that will randomly veto events. Protons with a kinetic energy

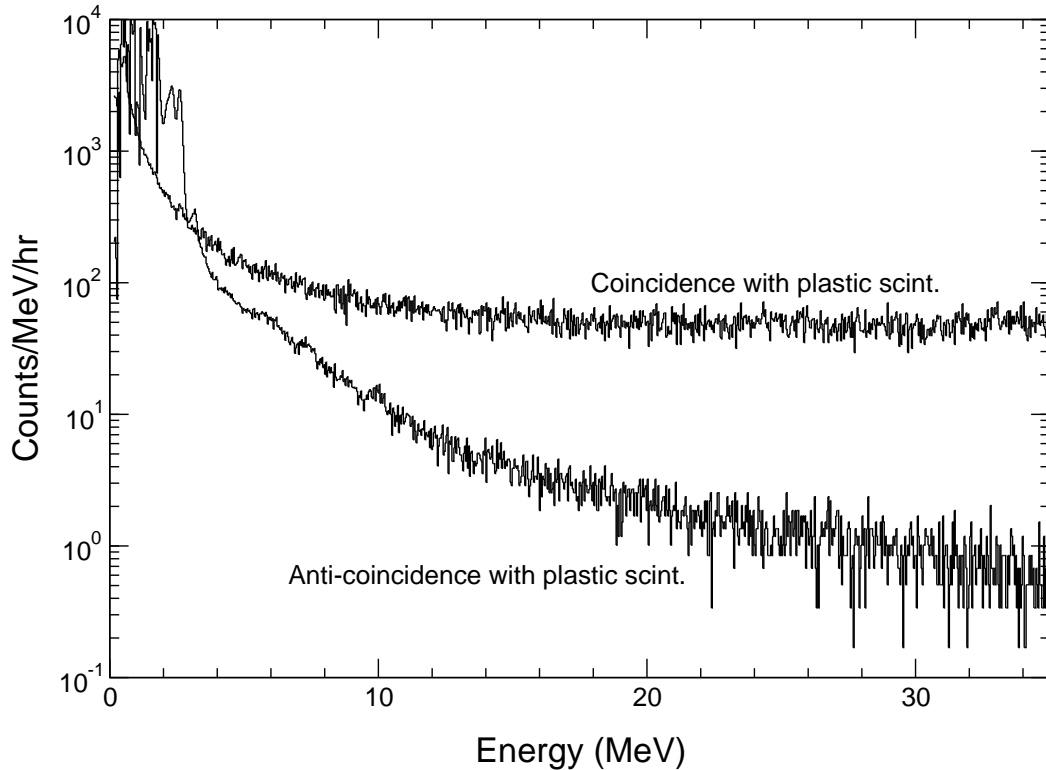


Figure 2.7: The background spectra in the spectrometer collected in coincidence and anti-coincidence with the veto counter.

of 2.1 MeV are required to produce the same amount of light as a 570 keV electron (calculated for NE102 using eqn. 1 given by R. Madey *et al.* [Ma78]). However, it is unlikely that such high energy protons are produced during the measurements since 2 MeV neutrons are only produced during the highest energy data run, and these are produced at 0° with respect to the beam direction. These neutrons would have to be elastically scattered into the plastic scintillator by heavy elements only, and then would have to transfer all of their kinetic energy to a proton upon scattering.

Figure 2.7 shows the background rates in the spectrometer with the beam off, in coincidence and in anti-coincidence with the veto counter. The spectra were collected with a conventional MCA system. The events in coincidence with the veto counter are due predominately to cosmic ray muons, and the characteristic flatness of such spectra can be

seen. Muons that pass through the BGO crystal with or without producing blocking pulses from the veto counter electronics are expected to produce a spectrum of the same shape. However, the shape of the spectrum collected in anti-coincidence with the veto counter indicates that the counts are probably not due to muon events, but due to cosmic ray induced bremsstrahlung instead. This is borne out by the fact that the anti-coincidence background rate at ~ 20 MeV energy was seen to fall by a factor of two when the hole in the collimator in front of the BGO crystal (see Figure 2.1) was blocked with 5 cm of lead. The remaining counts in the anti-coincidence spectrum were probably due to bremsstrahlung photons that entered by the back of the spectrometer, as it is not completely shielded by lead. Assuming that the unvetted muon event rate is less than ~ 0.6 counts/MeV/hr (ie. the minimum anti-coincidence rate measured), the active shielding is seen to be vetoing muon events with an efficiency $\geq 99\%$.

The secondary electrons and positrons produced by medium energy gamma rays within the BGO crystal can produce bremsstrahlung radiation. This radiation is likely to be emitted approximately in the direction of motion of the initial gamma ray, that is, towards the back of the crystal. As high detection efficiency for the ${}^3\text{He}(n, \gamma)$ gamma rays is more important than good energy resolution in this experiment, it is preferable to leave the back unshielded by plastic scintillator to reduce the chance of vetoing counts with the escaping bremsstrahlung radiation. This is also the reason why a thin (13 mm) active shield was built; to reduce the chance of absorbing any escaping photons. A thin active shield also has the advantage that fewer background or signal gamma rays and fewer neutrons will interact within it to randomly veto events. This design is in marked contrast to other medium energy spectrometers (see examples given by P. Paul [Pa74] and H. Ejiri [Ej89]), where active shields typically 10 cm thick surround the main detector in order to achieve

good energy resolution by identifying and rejecting those events in which some of the energy escapes the crystal.

2.4.3 Passive Shielding

The passive shielding is required to reduce the following backgrounds: i) gamma rays from the lithium target, ii) neutron capture within the BGO crystal, iii) neutron capture gamma rays from outside of the crystal, and iv) bremsstrahlung and knock-on protons and electrons produced by cosmic rays. Figure 2.1 shows schematically the shielding used in the spectrometer.

To shield the spectrometer from the medium energy gamma rays produced in the lithium target via the ${}^7\text{Li}(p,\gamma)$ reaction ($E_\gamma(\text{MeV}) \simeq 17.24 + \frac{7}{8}E_p$), a 15 cm long shadowbar of Mallory 1000 was placed next to the lithium target. Mallory 1000 is a high density alloy (19 g/cm³) composed of 90% tungsten and 10% nickel by weight. The mean free path of 20 MeV gamma rays in Mallory 1000 is about 1 cm. The mean free path of fast neutrons in this material is about 2 cm [Si72], so that the shadowbar is also useful for shielding the BGO detector from neutrons coming directly from the target.

The spectrometer is encased in paraffin to moderate the fast neutrons, and paraffin has also been placed between the shadowbar and the spectrometer to further moderate neutrons coming directly from the target. Inside the paraffin is 2.5 cm of borated polyethylene (7% natural boron by weight, produced by Reactor Experiments, Inc. of San Carlos, California) for moderating and capturing neutrons. Between the borated polyethylene and the lead there is ~ 1 mm of cadmium for capturing thermal neutrons.

There is ~ 10 cm of lead around the plastic scintillator for shielding against the cosmic ray secondary radiation and the neutron capture gamma rays produced in the neutron shielding. A 5 cm thick lead collimator with a 15 cm hole allows the BGO detector to

view the whole ^3He gas target while reducing the background gamma rays. The hole in the collimator is filled with boron carbide loaded paraffin. Structural supports within the spectrometer were made from aluminum because of its low (n, γ) cross section [Nu89].

Preliminary measurements showed that it was necessary to reduce the flux of low energy neutrons within the BGO crystal, since the resonance capture of neutrons by ^{73}Ge was producing substantial pile-up above the 13 MeV region. A satisfactorily low pile-up rate was achieved by packing boron carbide (B_4C) powder ($\Sigma_{n_{th}, \gamma} \simeq 60 \text{ cm}^{-1}$) around the BGO detector. The disadvantage of using boron to capture neutrons is that 478 keV gamma rays are produced 95% of the time through the $^{10}\text{B}(n, \alpha)^7\text{Li}^*$ reaction. These gamma rays are too low in energy to trigger the active shield, but they contribute to the pile-up in the BGO detector. Covering the BGO detector in cadmium was tried ($\Sigma_{n_{th}, \gamma} \simeq 114 \text{ cm}^{-1}$), however, it was found to be unsatisfactory because the cross section falls off sharply above $E_n \sim 0.5 \text{ eV}$, and because the high Q-values for the captures ($\sim 7\text{--}9 \text{ MeV}$) resulted in a large background of cascade gamma rays next to the scintillators with typical energies of 2–3 MeV. Lithium carbonate (Li_2CO_3) powder enriched to nearly 100% ^6Li ($\Sigma_{n_{th}, \gamma} \simeq 20 \text{ cm}^{-1}$) was tried, since no gamma rays are released in the capture reaction $^6\text{Li} + n \rightarrow \alpha + t$. However, due to the lower capture cross section, the pile-up rate into the region above 13 MeV was unacceptably high.

2.4.4 Electronics

In the present experiment, the count rate of $\sim 20 \text{ MeV}$ gamma rays from the $^3\text{He}(n, \gamma)$ reaction was ~ 20 counts/hour, while the background rate above 1 MeV was 10–20 kcps. Such conditions are typical in medium energy radiative capture measurements, and the electronic systems developed for such experiments tend to satisfy the same general requirements [Pa74], i.e. that pulse pile-up be minimized, and that gain stabilization or correction

be used over the long measurement periods. In addition to this, the livetime of the system must be known for measurements of absolute cross sections.

Pile-up can be reduced by clipping the $\sim 1.5 \mu\text{s}$ signal pulses shorter, using either delay-line techniques [Kn89, pages 578–580] or passive RLC filters [Am69]. Theoretically, pulses can be clipped down to roughly twice the risetime of the pulses. Practically, however, clipping the pulses to less than the decay time of the scintillator degrades the energy resolution of the system [Di70, Ge91]. Hence, to further reduce pile-up electronically, a pile-up rejection circuit must be used. Figure 2.8 shows an example of a circuit used with a pile-up rejector that was tried in the present experiment (see [Bl68] for a summary of pile-up reduction techniques used in other experiments). These systems typically involve splitting the signal into two branches. In the slow branch, the pulse of length T (which may or may not be clipped) is delayed and sent to an analog-to-digital convertor (ADC) through a linear gate. In the other branch, the signal is clipped as short as possible and sent to the pile-up rejection circuit. This circuit gates the slow pulse through to the ADC only if no other pulse appears within a time T before or after it. Otherwise, neither pulse is gated through. Usually, to reduce ADC deadtime, only pulses that are $\geq 10 \text{ MeV}$ are gated through.

Such systems have been used successfully with NaI detectors (see for example [Su68, Di70, Ha74, We81, Sa84, Ha88]), however, the pile-up rejection system shown in Figure 2.8 did not work satisfactorily with the present detector system. One reason is that the pulses from the BGO detector could not be clipped shorter than $\sim 120 \text{ ns}$. Thus, pulses arriving within 120 ns of each other could not be resolved by the pile-up rejection circuit, and pile-up occurred. On the other hand, pulses from NaI crystals coupled to fast photomultiplier tubes can be clipped much shorter, resulting in resolving times of $\sim 15 \text{ ns}$ [Bl68]. Another

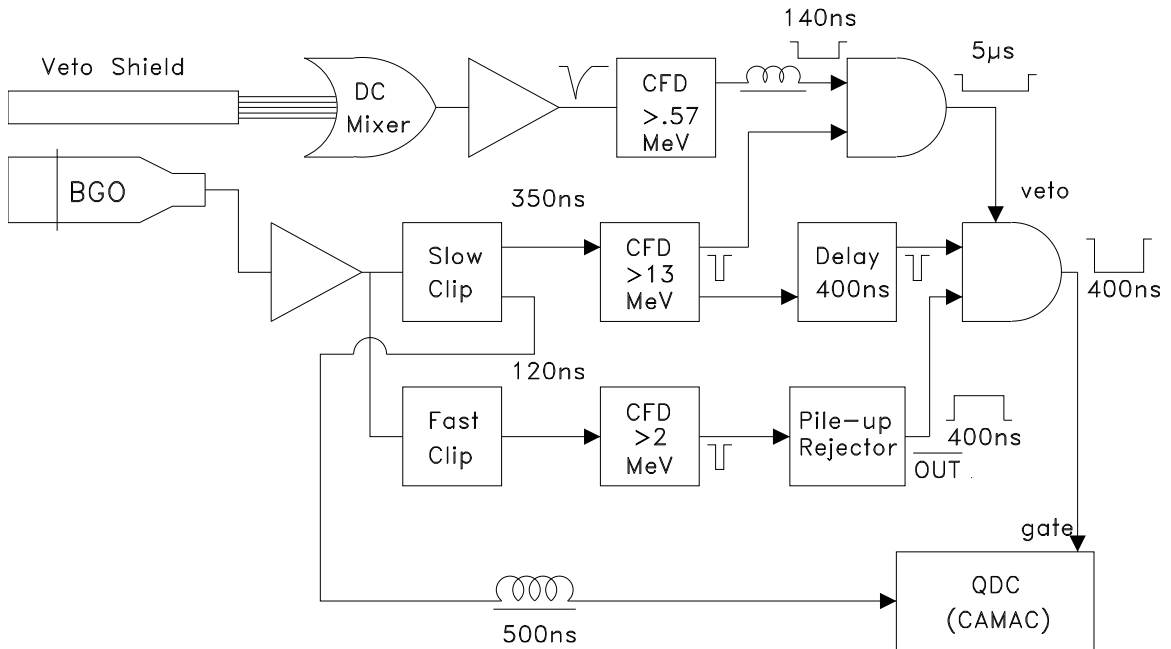


Figure 2.8: Electronics used in conjunction with a pile-up rejection circuit. The standard modules are: dc mixer - EG&G AN102/N, fast amplifiers - Philips Scientific Model 778, constant fraction discriminators - Philips Scientific Model 705, AND logic unit - Philips Scientific Model 755, logic delay - Lecroy Model 222 gate generator, QDC (charge-to-digital convertor) - Lecroy 2249W ADC.

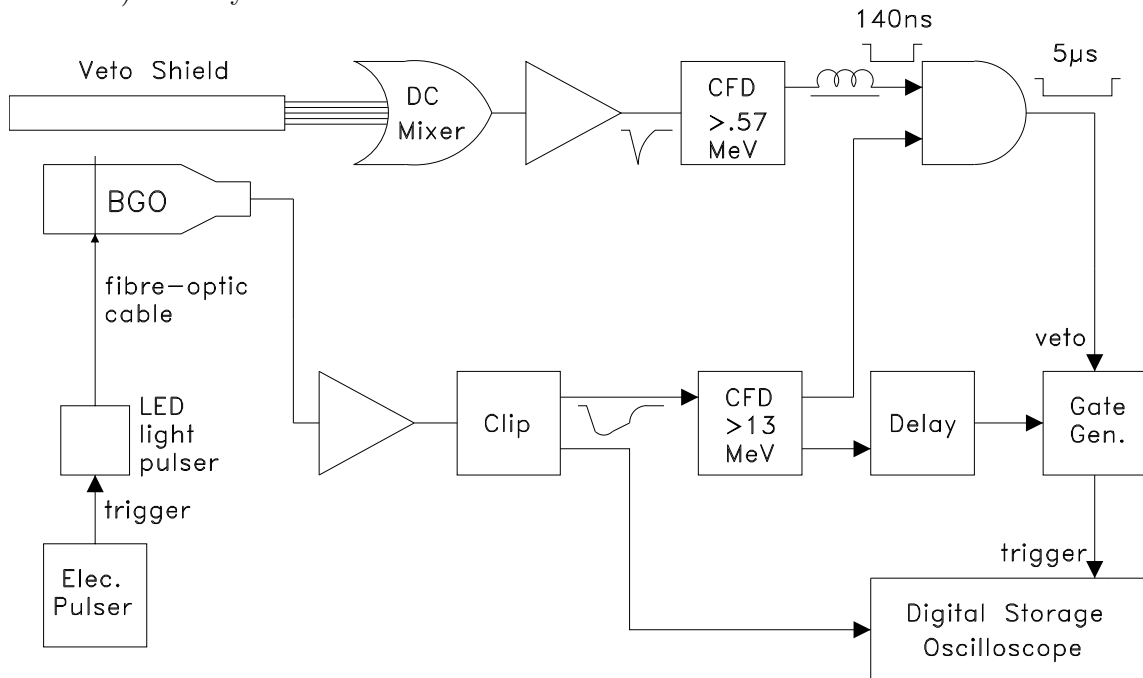


Figure 2.9: Electronics used in conjunction with the digital storage oscilloscope. The standard modules are as given in Figure 2.8, with the addition of: digital storage oscilloscope - Lecroy 9410, electrical pulse generator - Bradley Model 233.

reason why pile-up rejection was unsatisfactory with the BGO detector is that, due to the relatively small amplitudes of the signals, the shot noise is relatively large on the BGO detector pulses. When a scintillator pulse is clipped, the exponential tail is cancelled, but a *wake* of shot noise is left behind [Am69]. On large clipped pulses, this trailing noise can occasionally trigger the pile-up rejection circuit, leading to the spurious rejection of pulses. In addition to this, it is difficult to clip pulses using almost shorted stubs without producing multiple reflections, some of which may trigger the rejection circuit. For these reasons, a pile-up rejection circuit was not used with the present system.

Figure 2.9 shows the electronics used in place of the system described above. The ADC is replaced by a digital storage oscilloscope that digitizes and stores each pulse in memory. The advantage of such a system is that corrections for pulse pile-up, baseline shifting and gain variations can be made during the off-line analysis of each pulse. Thus, the electronics are simpler because on-line pile-up rejectors, baseline restorers and gain stabilizers are not necessary. However, disadvantages of such a system are that large quantities of memory are required to store the pulses, and the analysis of the raw data is complicated and time consuming.

The anode pulses from the BGO detector are amplified by a fast amplifier and clipped to ~ 350 ns using the circuit shown in Figure 2.10. Clipped pulses are sent to the digital storage oscilloscope, and also to a constant fraction discriminator (CFD). The discriminator level on the CFD is set to ~ 13 MeV (i.e. above the low energy background) to reduce the deadtime of the system and to reduce the amount of memory required to store the pulses. If triggered, the CFD produces two ~ 10 ns logic pulses. One pulse is sent to the anti-coincidence circuit, where, if it arrives in coincidence with a 140 ns logic pulse from the active shield circuit, it produces a $5 \mu\text{s}$ blocking pulse to veto the event. The other CFD

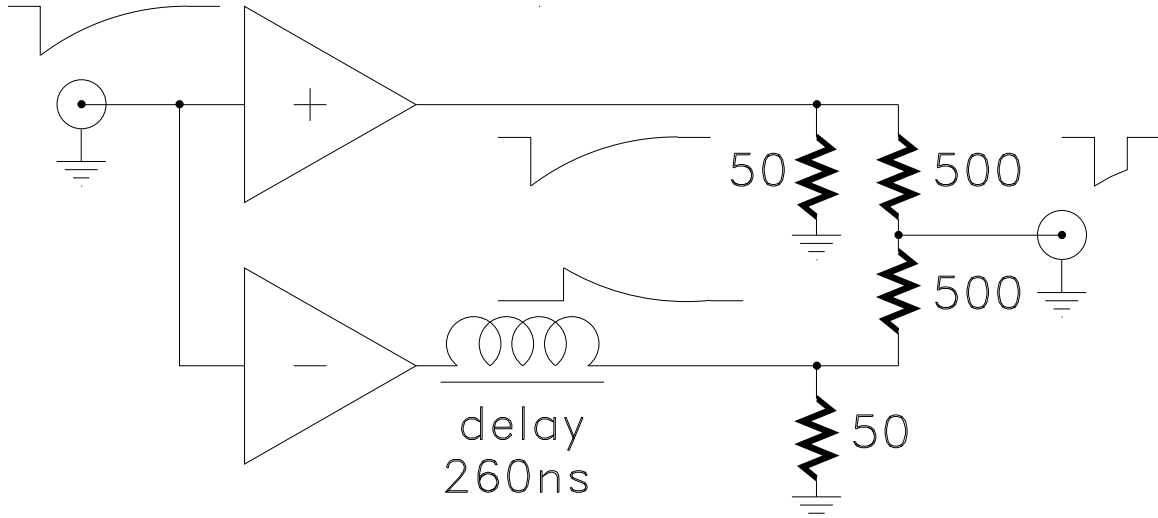


Figure 2.10: Circuit used to clip the anode pulses from the BGO detector. The amplifiers are Ortec 474 Timing Filter Amplifiers. The integration time constants are set at 20 ns to smooth the shot noise, and the gains are set to cancel the tails of the summed pulses. The inverted pulse was delayed by sending it through ~ 52 m of RG/8 cable.

logic pulse is delayed slightly and sent to a gate generator. If the gate generator is not disabled by an anti-coincidence blocking pulse, it triggers the digital storage oscilloscope to record the clipped anode pulse.

A relatively long blocking pulse of $5 \mu\text{s}$ was chosen to reduce the background due to afterpulsing in the BGO detector's photomultiplier tube. A large afterpulse can occur when a residual gas atom near the first dynode is ionized in an electron shower. This positive ion is accelerated into the photocathode, creating a second pulse of electrons a few microseconds after the initial pulse. The large pulses produced by cosmic ray muons traversing the BGO crystal are likely to produce afterpulses in the detector. Hence, to reduce system deadtime and memory usage, pulses from the BGO detector are ignored for $5 \mu\text{s}$ whenever there are coincident events in the BGO and plastic scintillators. Large afterpulses are occasionally produced by events that do not produce blocking pulses, and thus, are stored by the oscilloscope. However, these pulses are easily identified and rejected during off-line analysis because they do not decay exponentially like the BGO scintillator

pulses (see Figure 3.11 on page 54).

A Lecroy 9410 digital storage oscilloscope (DSO) is used to digitize and store the pulses. The input stage has a bandwidth of 150 MHz. The signals are sampled by an 8-bit ADC at a rate of 10^8 samples/s (10 ns/sample). Each sampled point is stored as an integer between +128 and -127. The baseline is offset to +96 to allow larger pulses to be recorded while allowing for some undershoot. Examples of digitized pulses are shown in Figures 3.5 to 3.11 (see pages 51–54). The settings of the DSO are chosen so that pulses corresponding to energies up to 30 MeV can be recorded without driving the ADC off-scale. The DSO has 10 kbytes of memory that can be parsed into 2, 5, 10, 20 or 50 segments, each of which can store a separate event. In the present experiment, the clipped ~ 350 ns pulses are stored in fifty $2 \mu\text{s}$ segments in the DSO's memory. Unclipped $\sim 1.5 \mu\text{s}$ pulses, however, would have to be stored in twenty $5 \mu\text{s}$ segments. Thus, besides reducing pile-up, using clipped pulses also reduces the amount of memory required to store the data.

Once armed, the ADC samples the input continuously, storing its output in successive memory locations in a ring buffer [Le90]. When the DSO is triggered, it stops digitizing after a user-specified number of samples. The contents of the ring buffer are then moved to one of the segments in memory, and the DSO is re-armed if at least one of the segments is unfilled. With this *pre-trigger* capability, signals that precede the trigger can be recorded without resorting to long delay cables that are a point of entry for noise. The transfer of the buffer contents to a segment results in a deadtime of $\sim 100 \mu\text{s}$.

Once fifty pulses are recorded, the contents of the memory are read by a Dell 386 computer through a general purpose interface bus (GPIB). If read into RAM, the data can be transferred at a rate of ~ 3 block/s, where each block consists of 10 kbytes. Writing to hard disk reduces the rate to ~ 1.5 blocks/s, while writing to floppy disk reduces it even

further to ~ 0.42 blocks/s. For the $2 \mu\text{s}$ segments used in the present experiment, the latter corresponds to a data collection rate of 21 cps. Although this is not a high count rate, nevertheless, 1 Mbyte of data would be acquired in four minutes. In addition to this, the off-line analysis program processes pulses at a rate of about seven pulses per second using the SUN 4/110 computer (cf. Section 3.2.2). Thus, for a two day run, the data acquisition rate is practically limited by the amount of available memory and the rate of analysis, and not by the speed of the DSO.

The pre-trigger time is set so that the ~ 350 ns clipped pulses are centered in the $2 \mu\text{s}$ segments, leaving ~ 800 ns before and after the pulses for determining baselines and inspecting for pile-up. The pulses are stored to 1.4 Mbyte floppy disks and then transferred to a SUN 4/110 computer for off-line analysis. A crude on-line analysis is also done on the Dell 386 computer to ensure that the experiment is operating satisfactorily (cf. Section 3.2.1).

A light pulser was built for measuring the livetime of the system. The circuit diagram is shown in Figure 2.11. Every fifty seconds, a $2 \mu\text{s}$ pulse turns on the transistor to saturation, allowing the capacitor to discharge through the LED. The RC time constant of the circuit was chosen to be ~ 300 ns, so that the light pulses produce signals from the photomultiplier tube that can be clipped like the scintillator pulses. The light is produced by a green ECG3003 LED (equivalent to a Litronix GL-56 LED), and is carried to the BGO detector via a fibre-optic cable. The light is introduced into the glass of the photomultiplier tube near to the photocathode via an optically coupled acrylic prism. The risetime of the signals due to the light pulses is ~ 120 ns, thus, they are easily identified during off-line analysis. The ratio of the number of identified pulser pulses to the number of times the pulser circuit is triggered gives the livetime of the system directly.

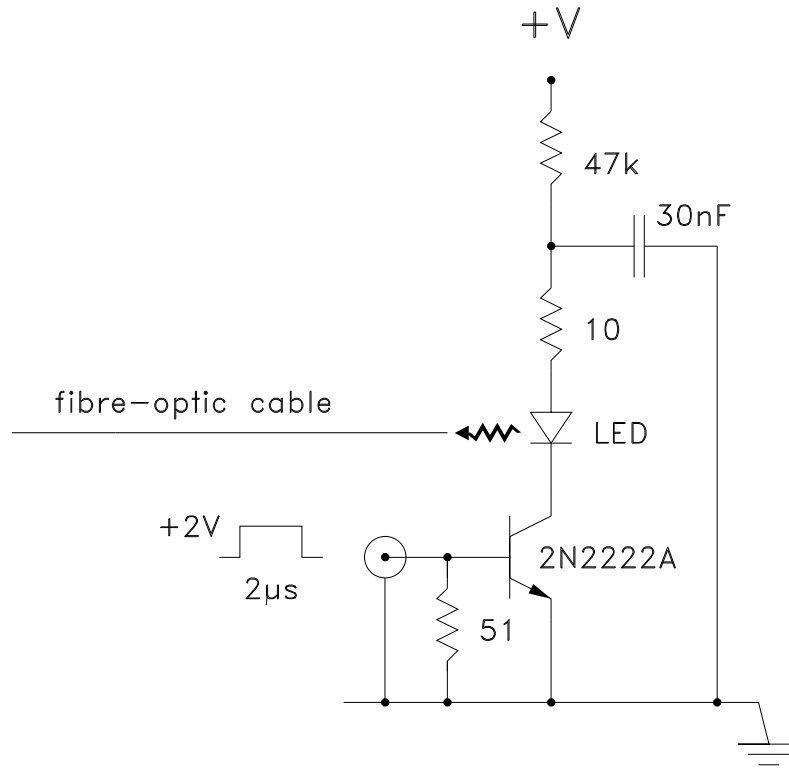


Figure 2.11: Circuit for the LED light pulser.

The light pulser is also used for monitoring long-term gain shifts. The output from the LED is not stabilized as in more complicated systems [Ko79], hence, the intensity of light pulses tends to decrease as the LED ages. The decrease was found to be linearly proportional to the number of pulses, although occasionally a sudden drop in the light output was noted. Changes in amplitude in the signal due to the pulser, other than those given above, are attributed to gain variations in the system. These long-term variations are then compensated for during the off-line analysis (cf. Section 3.2.2).

To reduce short-term gain variations due to high variable count rates and large amplitude pulses, a low-impedance voltage source is required for the last few stages of the photomultiplier tube [Gu67]. For the present experiment, an active transistorized voltage divider was built for the photomultiplier tube coupled to the BGO crystal. The circuit is shown in Figure 2.12, and is based on the system of Kerns [Ke77]. The transistors provide

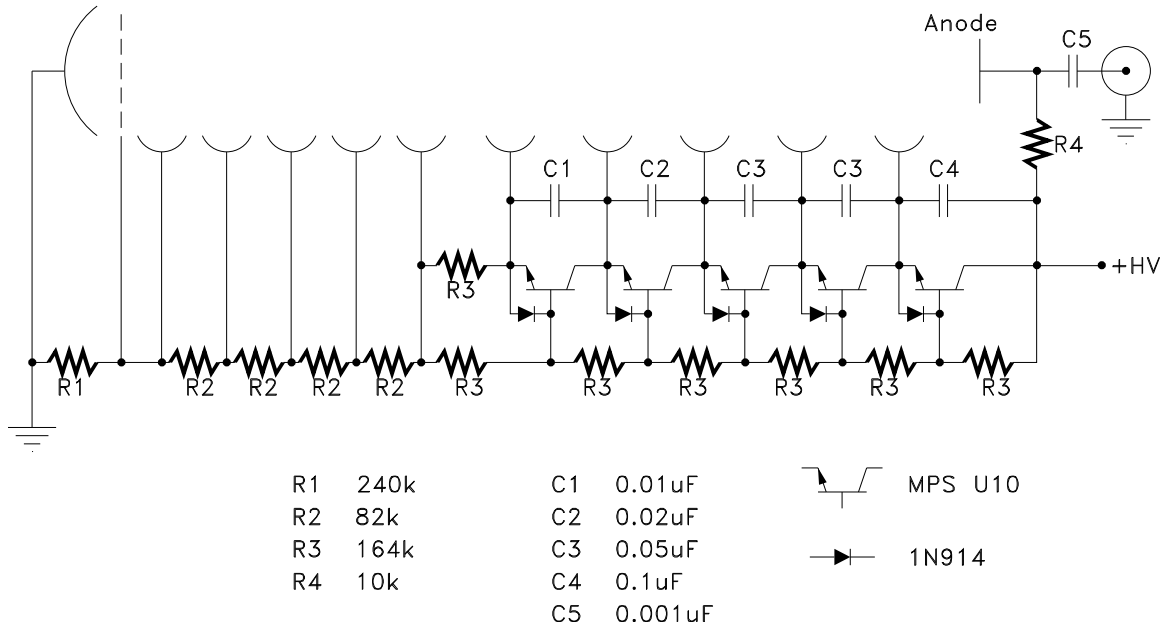


Figure 2.12: Circuit for the active transistor base used with the BGO detector.

a low-impedance voltage source for the last few dynodes which can react to changes in the average current within $\sim 0.5 \mu s$ [Sa84]. The usual decoupling capacitors [Kn89, page 272] are also present between the last few stages for providing the necessary charge for amplifying large amplitude pulses.

Chapter 3

Digital Signal Processing

Digitized waveforms contain pulse-shape information that can be useful for enhancing the signal-to-noise ratio of an experiment. For example, in the present experiment, pulse shapes are used in distinguishing between scintillator signals, LED light pulser signals, afterpulses and signals with pile-up. To extract this information, the waveforms are processed digitally by computer. The complexity of the processing techniques can vary greatly, depending on the amount of information that is to be recovered. In this chapter, pulse processing algorithms previously described in the literature are reviewed, and used as a point of departure for the description of the algorithm used in the present experiment.

3.1 Review of Other Systems

R.E. Chrien and R.J. Sutter [Ch86] describe a simple system used to check the feasibility of digital signal processing for the reduction of pile-up and for baseline restoration. Pulses from a NaI detector are fed into a pre-amplifier, shaped by an amplifier to produce pulses that are $\sim 2 \mu\text{s}$ long, and recorded using a transient digitizer with 8-bit resolution. Data can be collected at a rate of ~ 10 cps. The baseline offset is calculated outside of the region of the pulse. A peak sensing routine is used to check for pile-up. If no pile-up is detected, the charge of the pulse is calculated by integrating over a fixed region in the time frame;

otherwise, the pulse is discarded. It was shown that the system can reduce distortions in the energy spectrum for data rates ≥ 80 kcps.

Drndarevic *et al.* [Dr89] describe a system where the signals from a NaI detector are fed directly into a faster transient digitizer capable of digitizing with 8-bit resolution. The maximum event acquisition rate is ~ 1 kcps. A peak searching routine is used to identify pile-up pulses. If no pile-up is detected, the waveform is processed as in the system described above [Ch86]. However, if pile-up is detected, then the charge of the pulse of interest is calculated assuming the pulse shapes have the form [Kn89, eqn. 9-15a]

$$V(t) = V_0(e^{-\lambda t} - e^{-\theta t}) \quad (3.1)$$

where θ and λ are the anode and scintillator time constants, respectively. The peak position and amplitude (averaged over five channels) of the first pulse are calculated. If it is the pulse of interest, then the charge is integrated up to the point at which pile-up occurred, and the contribution from the tail is calculated using eqn.(3.1). If the first pulse is not the pulse of interest, then its charge is calculated using eqn.(3.1), and subtracted from the total charge. Pulses can be processed off-line on an IBM PC at a rate of 1000 events/s.

3.2 The Present System

The system used in the present experiment is similar to those described above, except that the anode signals from the detector are clipped (see Figure 2.10 on page 38), and an algorithm with a better resolving time than a peak sensing routine is used for identifying pile-up events. As in the system of Drndarevic *et al.* [Dr89], events with pile-up are deconvoluted. The deconvolution is done by a separate program that allows visual inspection of the results. A *two-pass* analysis of the data is done to correct for gain shifts. In the first pass, the charges of the signals produced by the LED light pulser are saved to a file, and used to calculate

gain changes in the system. In the second pass, gain corrections calculated from the first pass are applied to the charges of all of the signals.

3.2.1 On-line Analysis

In addition to the complex off-line analysis, a crude on-line analysis of each event is done on the Dell 386 computer. To reduce the computer processing time, baseline restoration and pile-up corrections are ignored during the on-line analysis. Instead, a fixed baseline is subtracted from each pulse, and the charge is evaluated over a fixed region of the stored waveform and used to increment the energy spectrum. The computer then writes the raw data to floppy disk as a 10 kbyte binary file which can be transferred to the SUN 4/110 computer for off-line analysis.

3.2.2 Off-line Analysis

Fit to a Single Pulse-shape

The first cut in the off-line analysis is to discard large pulses generated by cosmic ray muons that saturate the ADC of the digitizer. The baseline is then determined and subtracted from the pulses that survive the first cut. The baseline is determined from the mean of the flattest portion of the signal preceding the pulse. The region following the pulse is not used in determining the baseline since imperfect clipping and the trailing wake of noise make that region unsuitable for the calculation. The baseline subtracted pulses are then checked for pile-up. The peak searching routines used by [Ch86, Dr89] will only identify pile-up pulses when two pulses are separated by at least the time it takes a single pulse to reach its peak amplitude. For the present experiment, that time is ~ 140 ns (see Figure 3.5 on page 51). The resolving time for pile-up identification can be improved if the pulse shape information is used to identify pile-up events. The algorithm used in the present system

attempts to fit each event using the analytical expression

$$V(t) = \begin{cases} 0 & ; t \leq t_0 \\ V_0(e^{-\lambda(t-t_0)} - e^{-\theta(t-t_0)}) & ; t_0 < t \leq (t_0+t_d) \\ V_0e^{\lambda t_d}e^{-\theta(t-(t_0+t_d))} & ; t > (t_0 + t_d) \end{cases} \quad (3.2)$$

where t_0 is the arrival time of the pulse, t_d is the delay time set by the cable used for clipping the pulses (fixed at $t_d = 260$ ns), and θ and λ are the rise and fall time constants, respectively.

Because of the large variation in the pulse shapes from the BGO detector, no single values for the time constants θ and λ can be used to fit all of the pulses. Hence, their values, along with V_0 and t_0 , are left as parameters in the fit. A least-squares fit is done using the gradient-expansion method described by Bevington (see [Be69] and the references therein). For each pulse, the fitting routine adjusts the values of the four parameters to minimize the value of the reduced chi-square (χ_R^2) given by

$$\chi_R^2 = \sum_i \left(\frac{y_i - V(t_i)}{\sigma_i} \right)^2 / (d.o.f.) \quad (3.3)$$

where y_i is the baseline subtracted amplitude of the pulse at time t_i , $V(t_i)$ is calculated from eqn.(3.2), σ_i is the instrumental uncertainty on each point (taken to be ± 1 -bit), $d.o.f.$ is the number of degrees of freedom for the fit, and the sum runs from the time the pulse leaves the baseline to 300 ns after the peak amplitude has been reached. Due to the pulse-shaping effects of the electronics and imperfect pulse clipping, the observed pulse shape y_i can not be fit exactly by $V(t_i)$. The systematic difference between the two shapes results in a minimum value of χ_R^2 that is roughly proportional to the square of the pulse area. Hence, the quantity $\chi_R^2 / (\text{pulse area})^2$ ($\equiv \chi_{R/A}^2$) is used to determine the goodness of fit. Distributions of $\chi_{R/A}^2$, θ and λ for scintillator pulses are calculated from fits to ${}^7\text{Li}(p, \gamma){}^7\text{Be}$ events (refer to Section 5.3.1 for a detailed description). Similar distributions are calculated for the signals produced by the LED light pulser. Figures 3.1 to 3.3 show distributions of the values of

θ^{-1} , λ^{-1} and $\chi_{R/A}^2$ calculated for the $E_p=2.30$ MeV data. From these distributions, the ranges of the parameters and of $\chi_{R/A}^2$ are determined, and used to set empirical limits on what constitutes an acceptable fit to a pulse. The limits for the $E_p=2.30$ MeV data are also shown in Figures 3.1 to 3.3. These acceptance cuts are then used in the analysis of the ${}^3\text{He}(n, \gamma)$ and the background measurements. Events which fail the cut are set aside for re-analysis by the routine described in the following section. The steps in the analysis described so far are displayed in the flow chart shown in Figure 3.4.

Visual Inspection and Deconvolution

The pulses that fail the acceptance cuts for fits to a single pulse are re-analyzed using an interactive program that allows manual or automatic control of the fitting procedure, and visual inspection of the results. The program allows automatic or manual selection of the region over which the baseline was calculated. The automatic routine (also used in the process described above) occasionally chooses an incorrect region, in which case the region is chosen manually. The calculated baseline is displayed with the signal to allow visual inspection of the results. Signals that appear to be single pulses are fitted using eqn.(3.2), as in the process described above. The results of the fit are plotted with the signal, and the parameter values are displayed. If the parameters are not within the acceptance cuts for single pulses, the signal is fitted by two pulses described by eqn.(3.2). Due to the fact that the measured pulses are not fitted exactly by eqn.(3.2), unconstrained fitting of pile-up events often results in convergence to an incorrect solution. To overcome this problem, the decay constant λ of the smaller pulse is set to a constant value of $(270 \text{ ns})^{-1}$, leaving only seven degrees of freedom in the fitting operation. The starting values of the parameters V_0 and t_0 for the two pulses are calculated from initial estimates of the peak positions. These positions are calculated automatically, and result in successful fits most of the time.

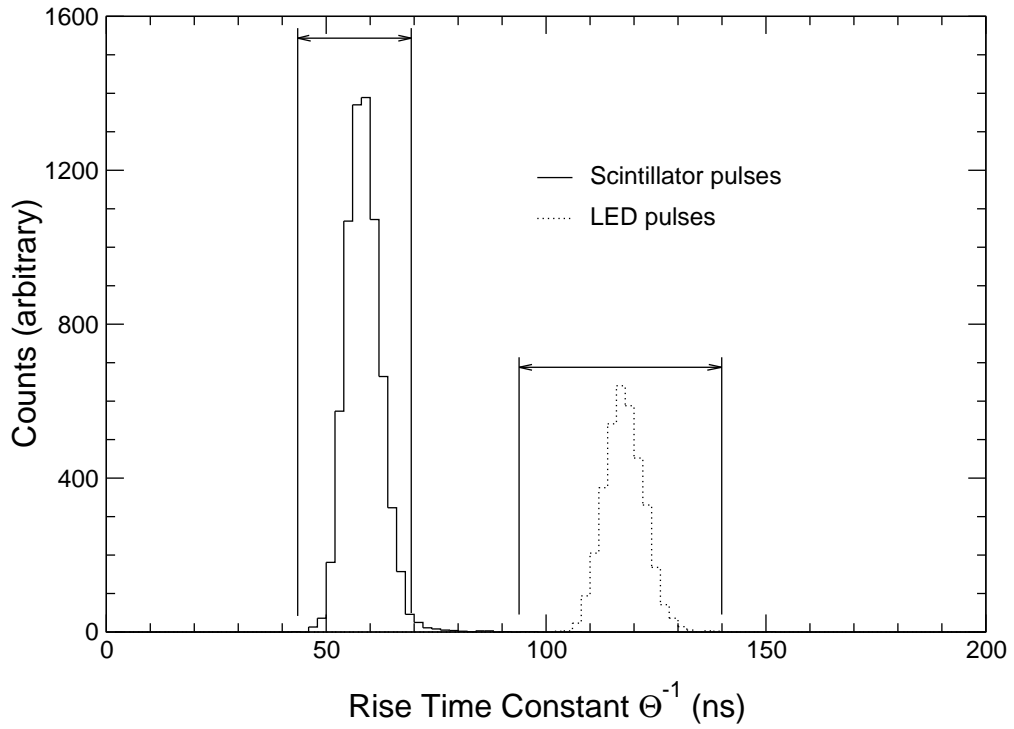


Figure 3.1: Distributions of rise time constants θ^{-1} for ${}^7\text{Li}(p, \gamma)$ and LED light pulser events. The acceptance cuts defined by the distributions are also shown.

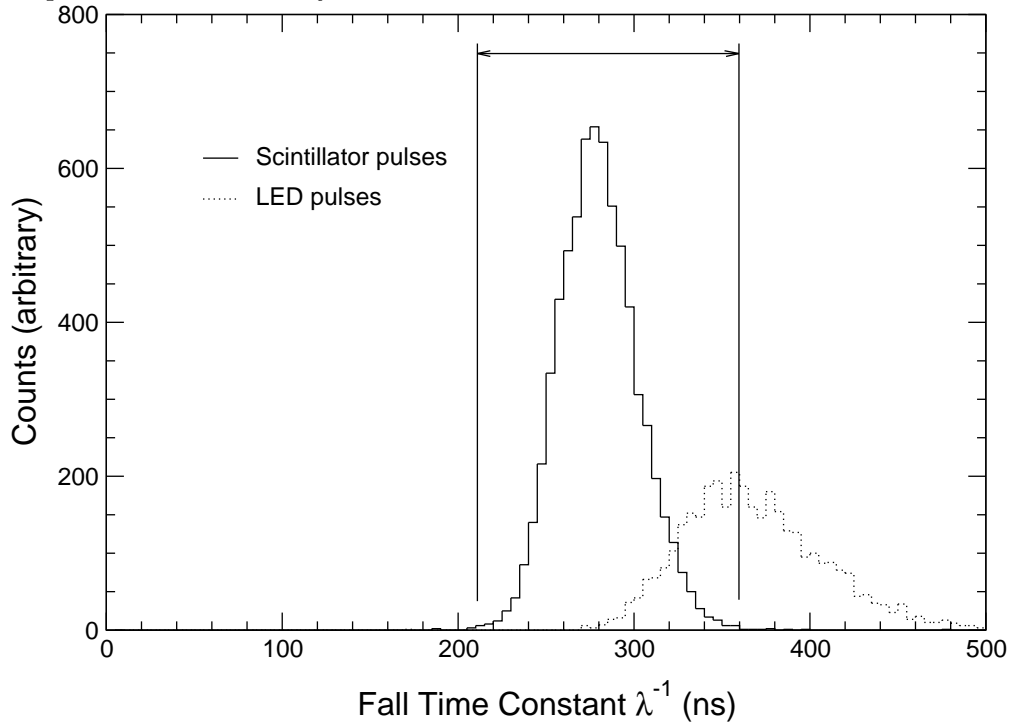


Figure 3.2: Distributions of fall time constants λ^{-1} for ${}^7\text{Li}(p, \gamma)$ and LED light pulser events. The acceptance cut defined for scintillator pulses is also shown.

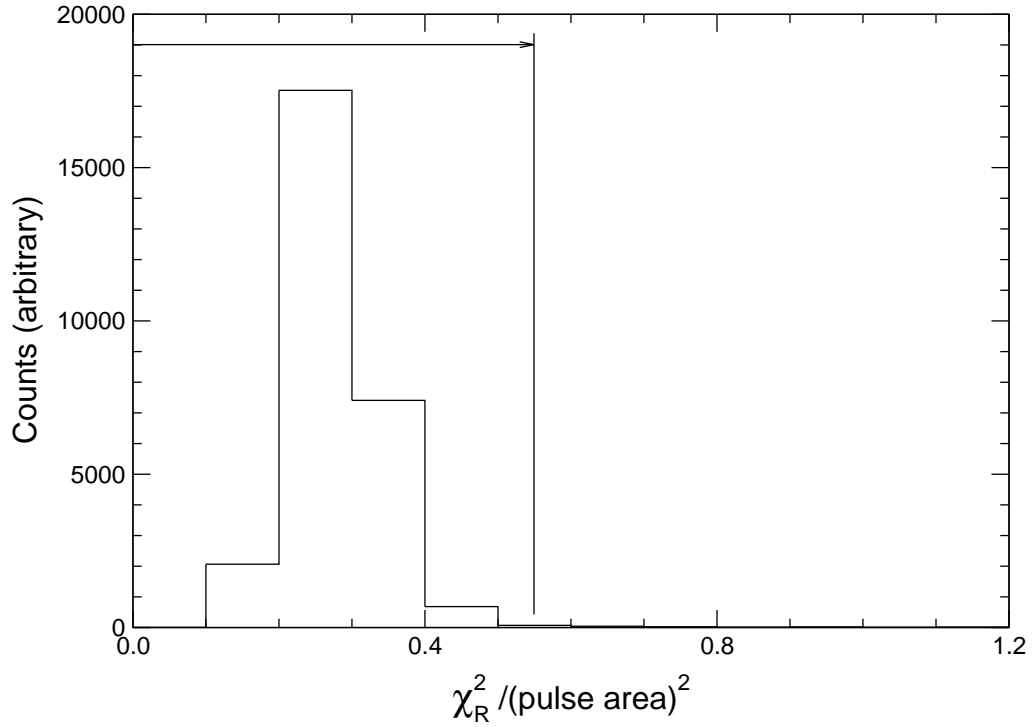


Figure 3.3: Distribution of $\chi_{R/A}^2$ for ${}^7\text{Li}(p, \gamma)$ events, along with the acceptance cut.

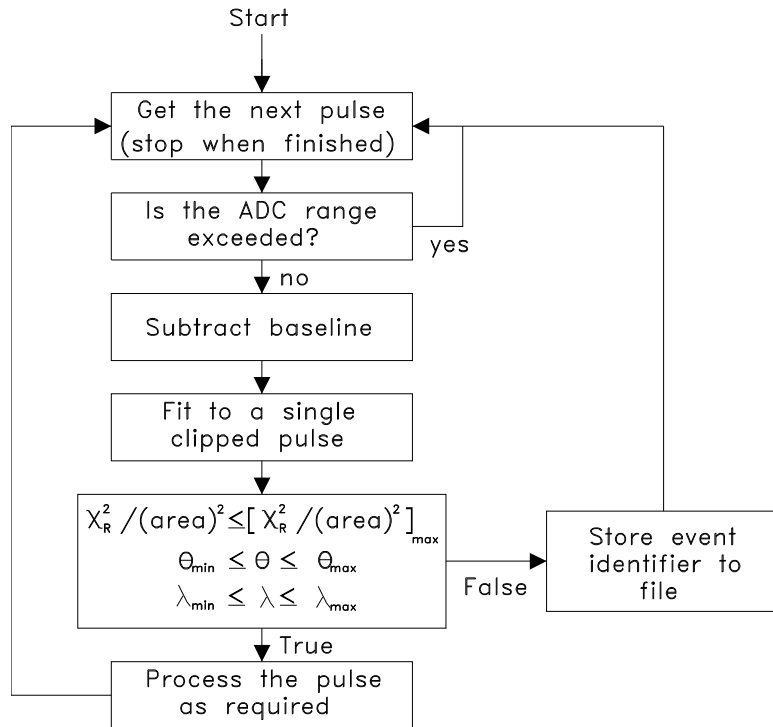


Figure 3.4: Steps in the analysis of raw pulses.

For some pulses, however, the fits converge to incorrect solutions. In these cases, the peak positions are manually selected. The two calculated pulses are plotted with the signal, and the parameter values are displayed. Events such as afterpulses are discarded.

Due to the convergence problem, a fully automatic fitting procedure for pile-up events is impractical for the signals used in the present experiment. Thus, visual inspection of the results is necessary to ensure that incorrect fits are not accepted. Examples of signals and the results of fits are shown in Figures 3.5 to 3.11. The

resolving time of the algorithm is ~ 50 ns, which is an improvement over the estimated resolving time of ~ 140 ns for the peak detection method. However, although the pile-up events can be identified with high certainty, the results of the deconvolution are uncertain when the pulses are separated by little more than the resolving time of the system (see Figure 3.10). This is not a serious problem, though, since most of this type of pile-up occurs between low energy events (≤ 10 MeV), and the integrals of the deconvoluted pulses are well below the region of interest used in the present experiment (15–23 MeV).

Processing of Fitted Pulses

A pulse that is fitted with $\chi^2_{R/A} \leq 0.55$, $90 \leq \theta^{-1} \leq 140$ ns, and corresponds to an event of energy ≥ 28 MeV is assumed to be produced by the LED light pulser. On the first pass, the charges of the LED signals are recorded to a file. The values in the file are averaged, and inspected for variations caused by gain shifts or changes in the LED output intensity (cf. Section 5.3.2). Gain correction factors are calculated to offset the gain shifts, and to make the gain of the system constant over all of the data runs. On the second pass, the gain corrected charges of all single pulses are calculated. Pulses that fail the acceptance

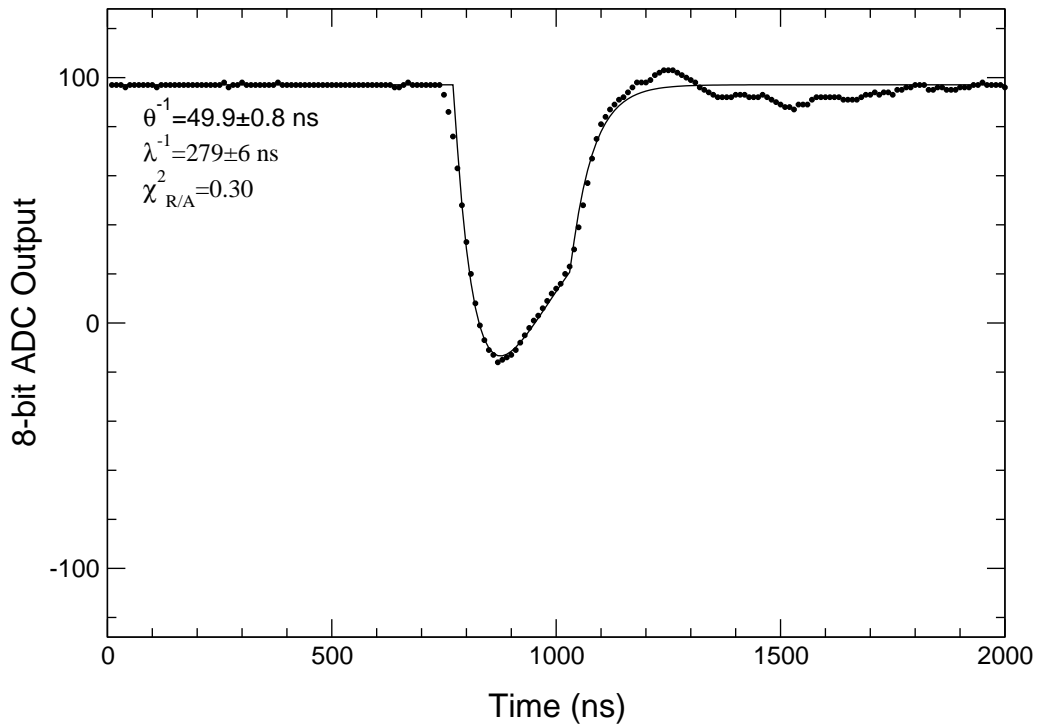


Figure 3.5: Scintillator event and fit to a single pulse.

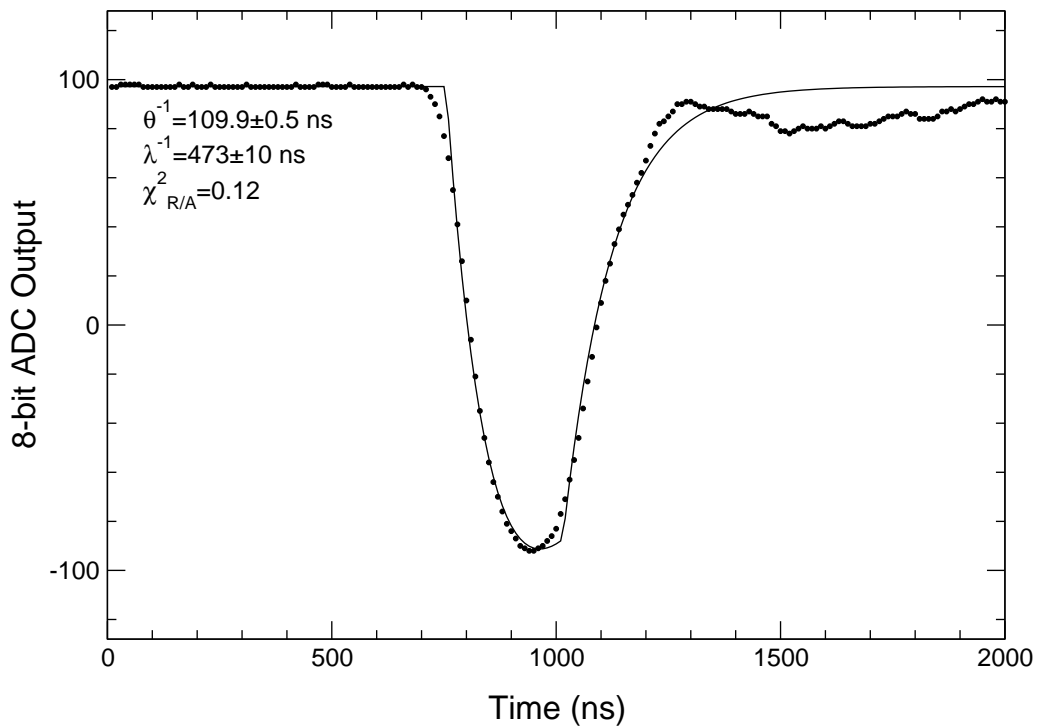


Figure 3.6: LED light pulser event and fit to a single pulse.

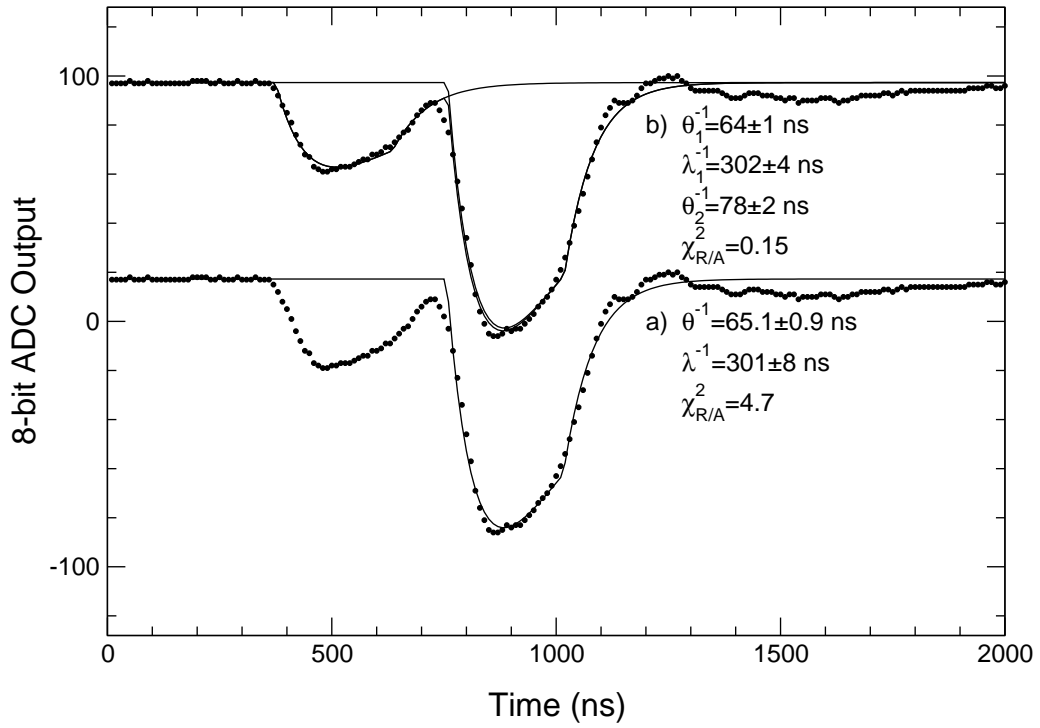


Figure 3.7: Pre-pulse pile-up event and fits to a) single, and b) double pulses.

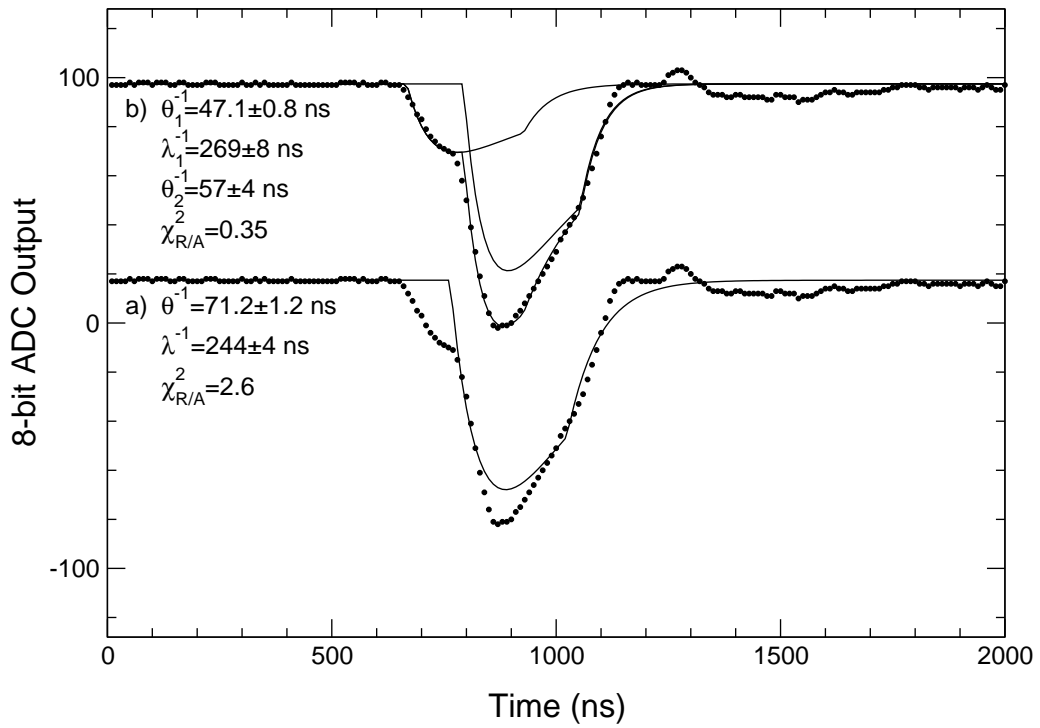


Figure 3.8: Pre-pulse pile-up event and fits to a) single, and b) double pulses.

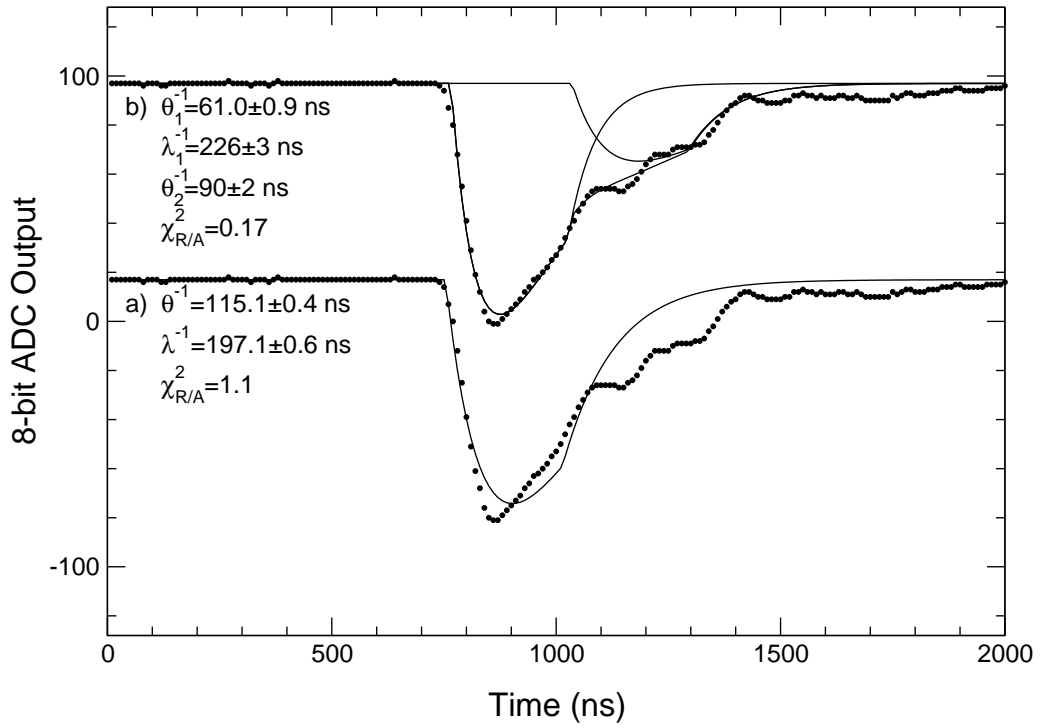


Figure 3.9: Post-pulse pile-up event and fits to a) single, and b) double pulses.

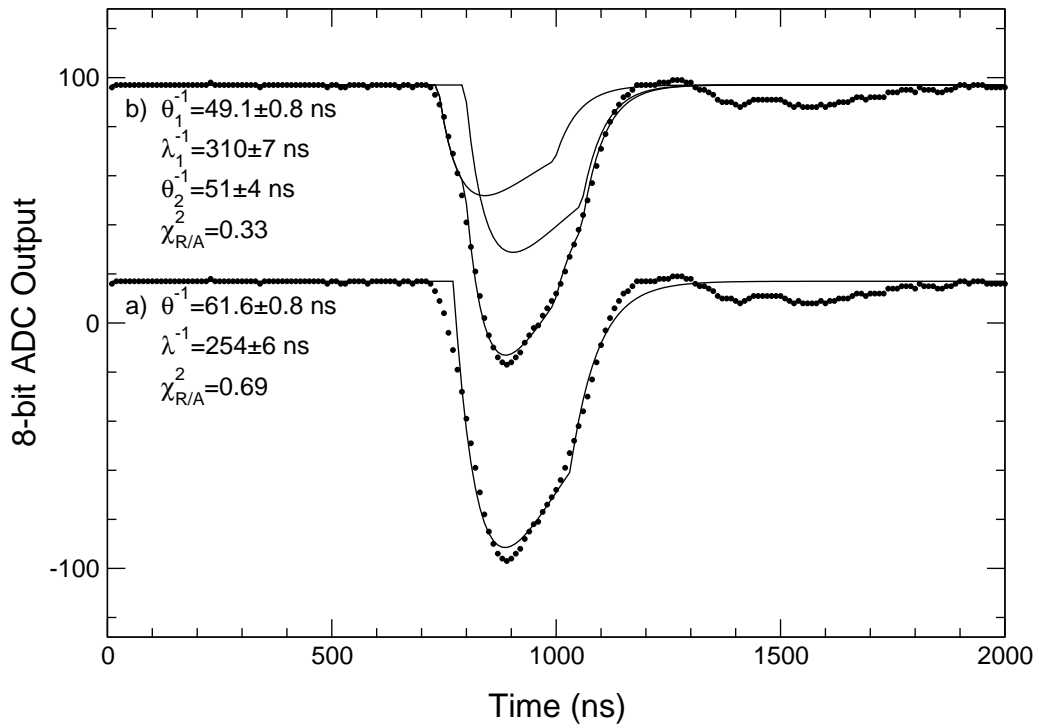


Figure 3.10: Pre-pulse pile-up event and fits to a) single, and b) double pulses.

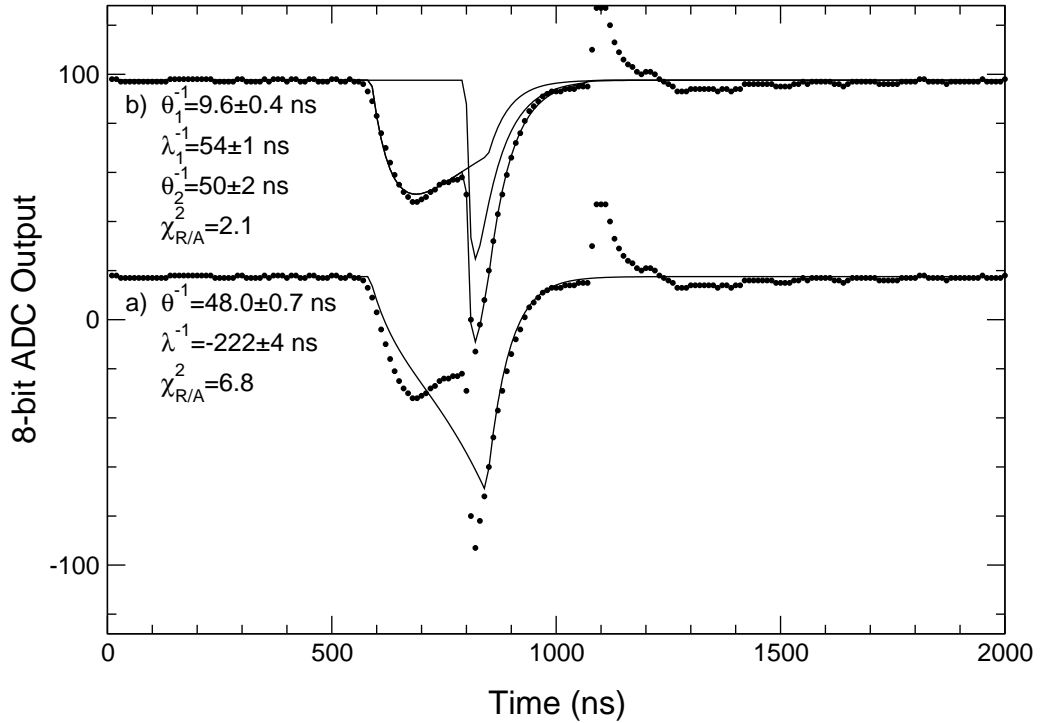


Figure 3.11: Pile-up event with afterpulse and fits to a) single, and b) double pulses.

cuts and are set aside for re-analysis have the gain correction factor stored along with the pulse identifier so that the charges of the re-analyzed events are corrected for gain shifts, as well. The values of θ^{-1} and λ^{-1} are used to increment distributions of the risetime and falltime constants, respectively, and the gain corrected charge is used to increment an energy spectrum. Separate distributions are incremented for those pulses that are produced by the LED light pulser. The steps in the processing are displayed in the flow chart shown in Figure 3.12.

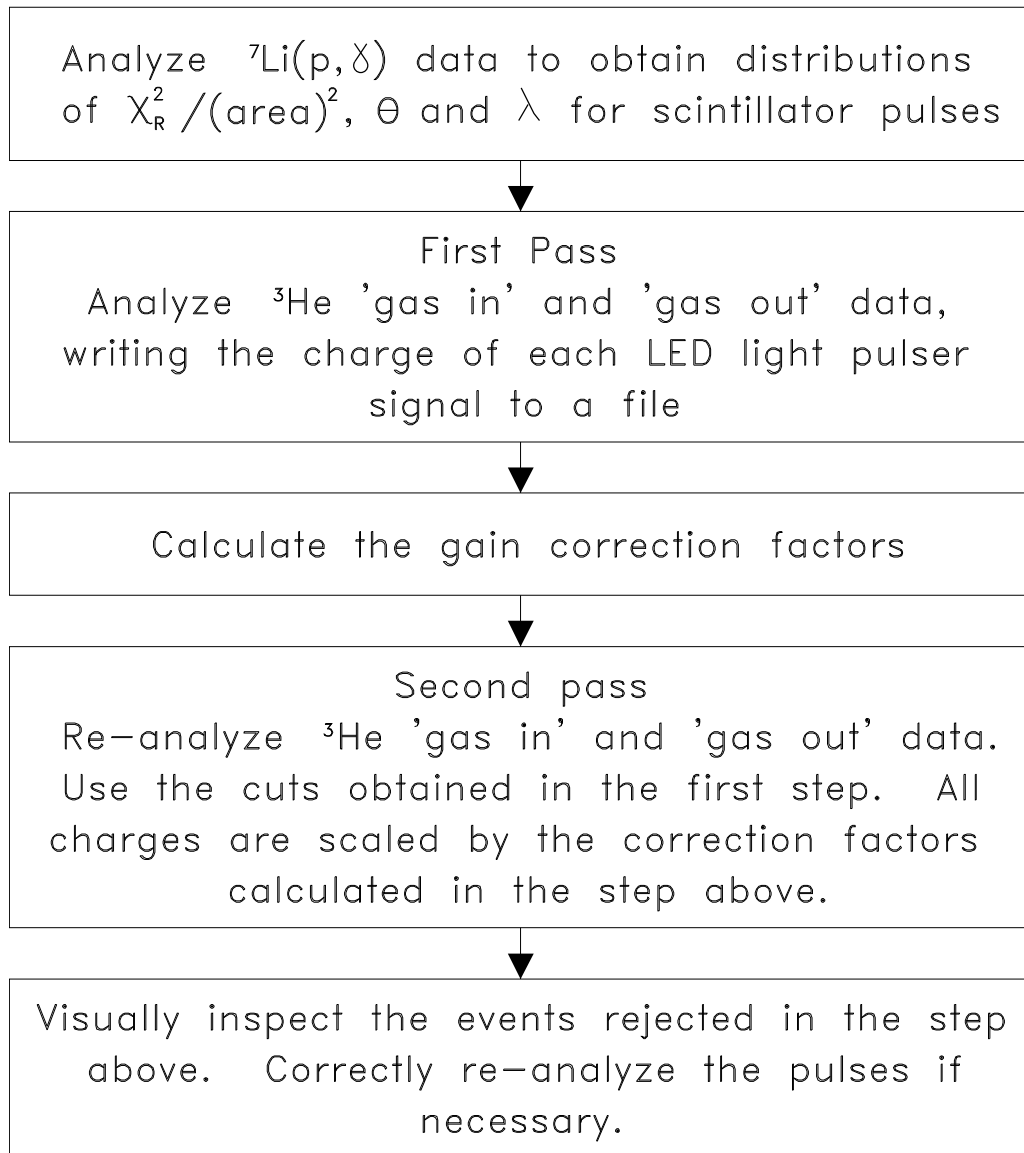


Figure 3.12: Flow chart for the processing of spectra.

Chapter 4

Monte Carlo Simulations

For each of the ${}^3\text{He}(n, \gamma)$ data runs, a gamma ray spectrum was measured with the spectrometer, and the total number of neutrons produced was calculated from the activity measurement of the lithium target. A Monte Carlo simulation of the experiment was used to determine the response function of the BGO detector per neutron per microbarn of the ${}^3\text{He}(n, \gamma)$ cross section. A comparison of the number of counts in the measured spectrum to that in the calculated spectrum gives the cross section of the reaction directly. In this chapter, the calculation of the response function of the BGO detector and the results of tests of the gamma ray tracking part of the simulation are described.

4.1 Description of the Monte Carlo Program

To calculate the response function of the medium energy gamma ray spectrometer for gamma rays produced via the ${}^3\text{He}(n, \gamma)$ reaction, the Monte Carlo program simulates the transport of particles in a geometry similar to that of the present experiment. The calculation can be conveniently divided into three main sections: i) the tracking of neutrons through the target holder and ${}^3\text{He}$ counter, ii) the tracking of gamma rays produced via the ${}^3\text{He}(n, \gamma)$ reaction through the ${}^3\text{He}$ counter and through the materials in the spectrometer around the BGO crystal, and iii) the tracking of photons, electrons and positrons within

the BGO crystal itself. The photons in parts ii) and iii) are tracked using an *analog* Monte Carlo technique [Ze63], in which each photon history evolves under interactions and cross sections that closely represent the true physical situation. Tracking charged particles in a similar manner is not feasible because of the large number of interactions that take place in the medium. Instead, the electrons and positrons in part iii) are tracked using *condensed random walks* [Be63], in which the particles are moved in steps over which the many low-energy, low-angle collisions are treated in a continuous manner. The tracking of neutrons in part i) is similar to that of the photons in parts ii) and iii), except that the small cross section for the ${}^3\text{He}(n, \gamma)$ reaction necessitates the use of some variance reduction techniques to increase the fraction of histories that produce events in the BGO detector (described in [Le84]). For detailed descriptions of methods of Monte Carlo simulations, the reader is referred to the references quoted above, as well as [Me70a, Gr75, Ne85] and the references therein. In the present work, the descriptions of the program are constrained to the physical assumptions upon which the histories are modelled.

4.1.1 Neutron Tracking

The energy and direction of motion of the neutrons produced by the ${}^7\text{Li}(p, n){}^7\text{Be}$ reaction are generated in the following manner. Given the incident energy of the protons (E_p) and the thickness of the deposited gold and lithium layers, the proton energy distribution in the target is calculated using the stopping powers given by Janni [Ja82]. For $E_p \geq 1.95$ MeV, the ${}^7\text{Li}(p, n)$ cross section is assumed to be constant over the range of proton energies within the target ($\Delta E_p \leq 20$ keV). The emission angle θ_{lab} of the neutron relative to the proton beam direction is chosen using the angular distributions given by [Li75], and the energy is calculated from the kinematics. For $E_p < 1.95$ MeV, the cross section can no longer be treated as constant over a range of $\Delta E_p \leq 20$ keV. Therefore, the proton energy for the

reaction is chosen from the distribution in the target, weighted by the value of the energy-dependent cross section. The cross sections are calculated from a fit to the data of J.H. Gibbons and R.L. Macklin [Gi59] tabulated in [Ki66]. The angular distribution is assumed to be isotropic in the center-of-mass reference frame [Gi60]. In both cases, the emission angle is confined to $\theta_{lab} \leq 45^\circ$ to reduce computational time spent tracking neutrons that are likely to miss the ^3He counter. For $E_p \geq 2.5$ MeV, the second group neutrons generated via the $^7\text{Li}(p, n_1)^7\text{Be}(0.43 \text{ MeV})$ reaction are also tracked.

Each neutron is tracked until it either is captured, elastically scatters below 10 keV in energy, or escapes from the vicinity of the lithium and ^3He target systems. The neutron interactions are:

i) elastic scattering with any of the materials in the target systems. The angular distribution for elastic scattering is assumed to be isotropic in the center-of-mass reference frame.

ii) capture via the $^3\text{He}(n, \gamma)$ reaction. When the $^3\text{He}(n, \gamma)$ reaction takes place, a gamma ray is generated and tracked in the next section of the program. At each proton energy, the cross section at energy E_n (MeV) is assumed to be $\sigma_{n,\gamma} = \sigma_0 f_\sigma(E_n)$, where σ_0 μb is the cross section at the maximum neutron energy E_0 produced in the $^7\text{Li}(p, n)^7\text{Be}$ reaction, and the energy dependence $f_\sigma(E_n)$ is

$$f_\sigma(E_n) = \frac{\sqrt{E_n}(20.58 + 3/4E_n)^3 e^{-3E_n/4\varepsilon}}{\sqrt{E_0}(20.58 + 3/4E_0)^3 e^{-3E_0/4\varepsilon}} \quad (4.1)$$

where $\varepsilon \approx 6$ MeV. This energy dependence is derived by B.H. Flowers and F. Mandl [Fl51] assuming a direct E1 transition and central nucleon-nucleon forces. The expression (4.1) is used for $E_n = 0.010$ – 2.0 MeV, and is shown in Chapter 6 to be a reasonable approximation to the cross section measured in the present work over the given energy range.

iii) *other* interactions that include (n, n') , (n, α) and (n, p) . Also included in this

category are (n, γ) reactions that occur in materials other than ${}^3\text{He}$. A neutron history in which one of these interactions takes place is terminated, and another history is started.

The cross sections for the elastic scattering and *other* interactions were obtained from [Sh90] for ${}^3\text{He}$, and from [Mc88] for all other materials.

For a ${}^3\text{He}$ gas pressure of 19.4 atm, a maximum pathlength of 25.9 cm through the gas, and a ${}^3\text{He}(n, \gamma)$ cross section of $100 \mu\text{b}$, the probability of radiative capture is $\sim 10^{-6}$. Thus, it would be impractical to do an analog Monte Carlo simulation of the neutron histories. Instead, a variation of the *forced collision* technique [Le84] is used to increase the number of histories in which a ${}^3\text{He}(n, \gamma)$ reaction occurs. Using the usual forced collision method, each neutron is started with a weighting parameter $W=1$. The neutron is split into two particles each time it enters the ${}^3\text{He}$. The first particle, which is forced to interact via the ${}^3\text{He}(n, \gamma)$ reaction, has the weighting parameter reduced by a factor of $(1 - e^{-\Sigma_{n\gamma}l})$, where $\Sigma_{n\gamma}$ is the macroscopic cross section for the ${}^3\text{He}(n, \gamma)$ reaction, and l is the pathlength through the ${}^3\text{He}$. The second particle, which is tracked to the next point of interaction without a ${}^3\text{He}(n, \gamma)$ reaction, has the weighting parameter reduced by a factor of $e^{-\Sigma_{n\gamma}l}$. Thus, a gamma ray is generated on each step through the ${}^3\text{He}$, with a weighting parameter set to that of the neutron that produced it.

This method is not exactly applicable for the present calculations because $\Sigma_{n\gamma}$ is the quantity that needs to be determined. However, since $\Sigma_{n\gamma}l \sim 10^{-6}$, some assumptions can be made that allow $\Sigma_{n\gamma}$ to be calculated. In the variation of the forced collision technique used in the present work, the weighting parameter of the neutron that does not interact is left unchanged since $e^{-\Sigma_{n\gamma}l} \simeq 1 - \Sigma_{n\gamma}l \simeq 1$. The weighting parameter of the gamma ray is then $(1 - e^{-\Sigma_{n\gamma}l}) \simeq \Sigma_{n\gamma}l$. As $\Sigma_{n\gamma}l = f_{\sigma}(E_n) (l/L) [(\Sigma_{n\gamma})_0 L]$, where L is the maximum pathlength through the ${}^3\text{He}$ counter and $(\Sigma_{n\gamma})_0$ is the cross section at the maximum neutron

energy E_0 produced in the ${}^7\text{Li}(p, n)$ reaction, each gamma ray is weighted by $f_\sigma(E_n)$ (l/L) during the calculation, and the value of $(\Sigma_{n\gamma})_0$ is determined afterwards by scaling the Monte Carlo generated gamma ray spectrum to fit the experimental spectrum. Due to the small cross section, the position of the radiative capture event is chosen from a uniform distribution along the pathlength through the ${}^3\text{He}$.

4.1.2 Gamma Ray Tracking Outside of the BGO Crystal

The first step in the tracking of each gamma ray produced via the ${}^3\text{He}(n, \gamma)$ reaction is to determine its energy and direction of motion. The emission angle θ of the gamma ray relative to the direction of motion of the neutron is chosen from an isotropic distribution in the center-of-mass reference frame, and the energy is calculated from the kinematics. The angle and energy are then transformed into the laboratory reference frame, and the tracking of the gamma ray out of the gas target begins. To reduce the computational time, the production of the gamma rays is confined to a cone of 16° half-angle directed at the BGO crystal. The gamma rays produced outside of this cone that Compton scatter into the crystal can be ignored because their energies are reduced below the threshold of ~ 13 MeV used in the present experiment.

The gamma rays can interact through the photoelectric effect, Compton scattering, Rayleigh scattering or pair production. The cross sections for the interactions are calculated from the tabulated values of E. Storm and H.I. Israel [St70]. To reduce the computational time, electrons and positrons are not tracked outside of the BGO crystal. In the case of Compton scattering, the scattering angle of the gamma ray is chosen from the Klein-Nishina formula using the method of H. Kahn [Ka56], and the Compton electron is ignored. Photoelectrons produced via the photoelectric effect are ignored. Gamma rays that undergo Rayleigh scattering are deflected without losing energy; the scattering angle is chosen as

described in [Ne85]. In the case of pair production within the field of the nucleus or atomic electrons, two oppositely directed 511 keV photons from the annihilation of the positron are produced at the location of the interaction, and subsequently tracked.

Since electrons and positrons are not tracked in this part of the program, neither bremsstrahlung nor positron annihilation-in-flight photons can be generated in the materials outside of the BGO crystal. Thus, the low energy tail of the response function of the spectrometer may not be accurately reproduced. However, this is not a serious problem since the low energy part of the measured spectrum is dominated by background gamma rays produced by the radiative capture of neutrons in the spectrometer, and these are not reproduced by the Monte Carlo calculation. In the region of the ${}^3\text{He}(n, \gamma)$ peak, the response function should be accurately reproduced because the BGO will most likely receive only a small fraction of the initial gamma ray energy after the production of a high energy electron or positron outside of the crystal.

A photon history in this part of the program is terminated if the photon i) is absorbed through the photoelectric effect or pair production, ii) Compton scatters below 15 keV in energy, iii) leaves the vicinity of the spectrometer, or iv) enters the BGO crystal.

4.1.3 Gamma Ray, Electron and Positron Tracking in the BGO Crystal

A typical feature of response functions of medium energy gamma ray spectrometers is the *tail* extending below the peak region, produced predominately by events in which some of the energy is carried off by escaping bremsstrahlung [Pa74]. The Monte Carlo calculation must be capable of simulating such events. This part of the program allows for the production and tracking of e^\pm pairs, delta rays and bremsstrahlung within the BGO crystal. The present program is based on the Monte Carlo simulation developed by B.J. Varley *et al.* [Va81] for calculating response functions of germanium detectors for electrons, positrons

and photons in the energy region of 50 keV to 12 MeV. For a description of the physics embodied in that program, the reader is referred to [Va81] and the references therein. Only the changes required to extend the program to allow for the tracking of medium energy particles in BGO are described below.

The tracking of photons in the BGO is similar to that in the region outside of the crystal in that an analog Monte Carlo calculation is done, and the same interactions are allowed (ie. the photoelectric effect, Compton and Rayleigh scattering, and pair production). Changes to the photon tracking part of the previous code of [Va81] include the addition of Rayleigh scattering, and the calculation of all photon cross sections from the tabulated values of E. Storm and H.I. Israel [St70].

Electrons and positrons are tracked using the Class II mixed procedure of [Be63], wherein the charged particles are moved in steps that reduce the energy logarithmically (5% per step) as they travel between *catastrophic* events such as Mott scattering events in which the particle is deflected by at least 30° , or events in which knock-on electrons or bremsstrahlung photons above the cut-off energies are produced. The cut-off energies are $T_{min} = 190$ keV for charged particles and $P_{min} = 100$ keV for photons, and the secondary particles are set aside for tracking at a later time. The production of knock-on electrons and bremsstrahlung photons below the energy cut-offs is accounted for by the restricted collisional and radiative energy losses calculated over each step, and the Mott scattering interactions that deflect the particles by less than 30° are accounted for over each step by the modified multiple scattering theory of G. Molière [Be53] and by the plural scattering theory of E. Keil *et al.* [Ke60] (also described in the review article by W.T. Scott [Sc63]). One- and two-quantum annihilation-in-flight of positrons is also included. The following changes were made to the code of [Va81] with respect to the tracking of charged particles:

i) In the previous code, to save computational time, a charged particle whose range is too small to allow it to escape the detector is assumed to travel in a straight line to the end of its range. The number and energies of the bremsstrahlung photons emitted over this path are sampled from the distributions calculated by B. Grosswendt [Gr74], and the rest of the energy of the particle is deposited in the detector. This simplification is not used for the present calculations because the distributions of [Gr74] were not calculated for BGO material.

ii) The Mott scattering differential cross sections for electrons and positrons in the previous code are calculated using the McKinley-Feshbach formula [Mc48]. This formula is valid only for materials in which $Z/137 < 0.2$. Because of the presence of bismuth ($Z=83$) in the BGO crystal, the formula could not be used for the present calculations. Instead, the differential cross sections for electron and positron Mott scattering in BGO were calculated using the method of N. Sherman [Sh56], and fits to these results were used in calculating the cross sections during the Monte Carlo simulation.

iii) The relative energy of the electron and positron after pair production is calculated in the previous code using the approximate formula of Hough [Ho48], as described in [Ze63]. For the present calculations, the relative energy of the electron and positron is sampled using the more accurate method of J.C. Butcher and H. Messel [Bu60] for compounds. Below 2 MeV, the method becomes inefficient, hence, to save computational time, the total available energy is divided evenly between the electron and positron.

iv) The one-quantum annihilation-in-flight cross section is calculated in the previous code using the first Born approximation as described in He54. The results of this calculation are known to be too large by a factor ≥ 4 [Jo64]. Hence, for the present calculations, the cross section for a positron kinetic energy below 1.28 MeV is obtained from interpolation

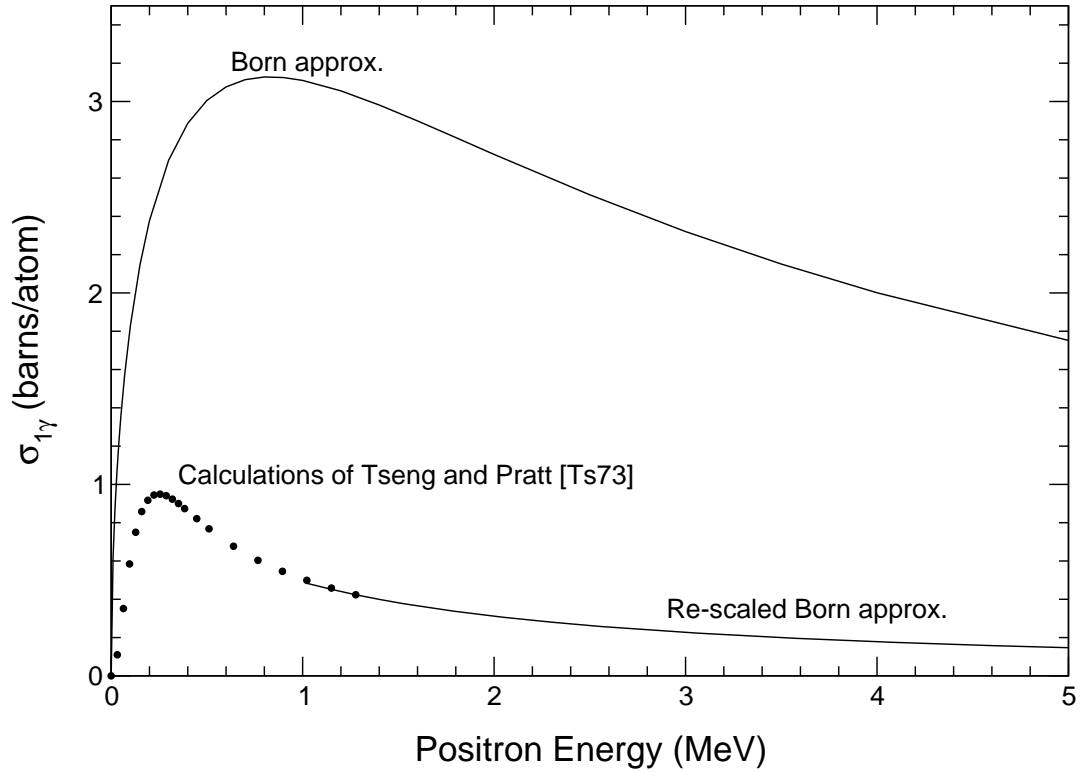


Figure 4.1: The calculated one-quantum annihilation-in-flight cross section for capture by the K and L shell electrons of bismuth. The calculated results of [Ts73] and the re-scaled Born approximation results were used to compute the cross section in the Monte Carlo simulations. The Born approximation results are shown for comparison.

of the more accurate calculated results of H.K. Tseng and R.H. Pratt [Ts73] for capture by K shell electrons. The cross section is increased by 20% to account for capture by the L shell electrons [Br72]. The calculations of [Ts73] do not extend above 1.28 MeV, however, a reasonable fit to the values in the region below this energy is obtained using the Born approximation if the positron kinetic energy is scaled up by a factor of two, and the cross section is scaled to match at 1.28 MeV (see Figure 4.1). This expression is used to approximate the cross section above 1.28 MeV. As this interaction is rare, an error in the cross section above 1.28 MeV is not likely to affect the results of the simulation. The cross section is calculated for bismuth only, as it scales as the fifth power of the atomic number of the element.

v) The restricted collisional stopping powers for electrons and positrons are calculated in the present code using the improved evaluation of the density effect given by S.M. Seltzer and M.J. Berger [Se84].

vi) The differential cross sections $\frac{d\sigma}{dk}$ (k is the photon energy) for the emission of bremsstrahlung by electrons are obtained from the tables of S.M. Seltzer and M.J. Berger [Se86a] for the present calculations, and are assumed to be the same for positrons. These replace the cross sections suggested by H.W. Koch and J.W. Motz [Ko59] that are used in the previous code. Also, where in the previous code bremsstrahlung photons were emitted isotropically, the angle of emission in the present calculations is sampled from formula 2BS given by Koch and Motz [Ko59]. This formula is derived under the assumptions of extreme relativistic particles and small angles ($\sin \theta = \theta$), hence, the angular distribution will not be correct for lower particle energies. However, this is unlikely to affect the results of the simulation as the cross sections for the generation of bremsstrahlung at lower energies are small, and the lower energy bremsstrahlung photons are less likely to escape the BGO crystal. It is more important that the higher energy photons that are more likely to escape the detector are treated accurately. The angular distribution is calculated for bismuth only, since the cross section scales as Z^2 .

Each particle is tracked until: i) it is absorbed, in which case any particles produced in the interaction are set aside for later tracking, ii) it elastically scatters below the cut-off energy, in which case the remaining energy of the particle is deposited in the BGO crystal, and if it is a positron, a pair of oppositely directed 511 keV photons are produced and set aside for later tracking, and iii) it escapes the BGO crystal. A photon that escapes is set aside for tracking in the second part of the program, whereas an electron is discarded, and a positron is assumed to produce two 511 keV photons just outside of the crystal. In the

latter case, the two photons are tracked later in the second part of the program.

4.1.4 Calculating the Response Functions

The inputs required for the calculations are the geometrical factors specifying the relative positions of the targets and the spectrometer, the incident proton energy, the thickness of the gold and the lithium layer in the target, and the required number of events of interest. During the calculation, each event is tracked, starting with the production of a neutron, until all the particles are either absorbed, escape, or are scattered below the energy cut-offs. Over each event, the total amount of energy deposited in the BGO crystal is calculated. The total amount of the energy deposited in the plastic scintillator veto shield is also calculated, and if the total exceeds the threshold of ~ 570 keV for the anti-coincidence electronics, the event is vetoed. In the simulations, typically 2.4% of the total counts are vetoed in this way. To determine the effects of scattering in the experiment, the events are flagged if the neutrons or photons were scattered before capture in the regions of interest, and if the gamma rays were aimed directly at the crystal. Separate distributions of the deposited energy in the BGO crystal, emission angles of the gamma rays and energies of neutrons captured through the ${}^3\text{He}(n, \gamma)$ reaction are incremented depending on how the event is flagged. For each event, the relevant spectra are incremented by the weighting factor of the gamma ray.

The program is run on a Sparc 10 computer, and produces events of interest at a rate of $\sim 2 \text{ s}^{-1}$. When the required number of events that deposit energy in the crystal has been reached, the program outputs the various spectra along with the total number of neutrons that were tracked. Each BGO energy spectrum is then convolved with a suitable gaussian function to match the resolution of the experimental data. The results of the calculations for the various distributions, along with such quantities as the neutron and photon attenuation

through the shielding materials, and the intrinsic efficiency of the BGO detector are given in Section 5.4.

4.2 Testing of the Program

The gamma ray and charged particle tracking part of the calculation was tested by comparing the results of simulations with measurements using known fluxes of gamma rays. The known fluxes were produced using $^{27}\text{Al}(p, \gamma)^{28}\text{Si}$ and $^7\text{Li}(p, \gamma)^8\text{Be}$ resonance reactions, as described below. Modifications to the experimental set-up and to the Monte Carlo program, along with the results of the measurements and simulations, are described as well.

4.2.1 Modifications

The ^3He counter and Mallory 1000 shadowbar were removed from the set-up, and the target assembly was rotated by 90° and moved directly in front of the spectrometer (see Figure 4.2). The spectrometer and the paraffin shielding in front of it were left unchanged. To decrease the deadtime of the data acquisition system during the $^7\text{Li}(p, \gamma)$ yield curve measurements, the digital storage oscilloscope was replaced by a Lecroy Research System 2249 W charge-to-digital converter (QDC) in a CAMAC crate. The rest of the electronics were left unchanged, except that the signal to the QDC was sent through ~ 70 m of doubly-shielded cable to delay it with respect to the trigger pulse.

The program was modified to reflect the changes in the apparatus. The tracking of neutrons, and the generation and tracking of gamma rays within the ^3He counter were removed from the program. Instead, the gamma rays from the resonance reactions are produced on the tantalum blank, and tracked out of the target assembly. The center-of-mass energy of a reaction is fixed at the resonance energy E_R , since the widths of the resonances studied (≤ 12 keV) are much smaller than the resolution of the spectrometer. The

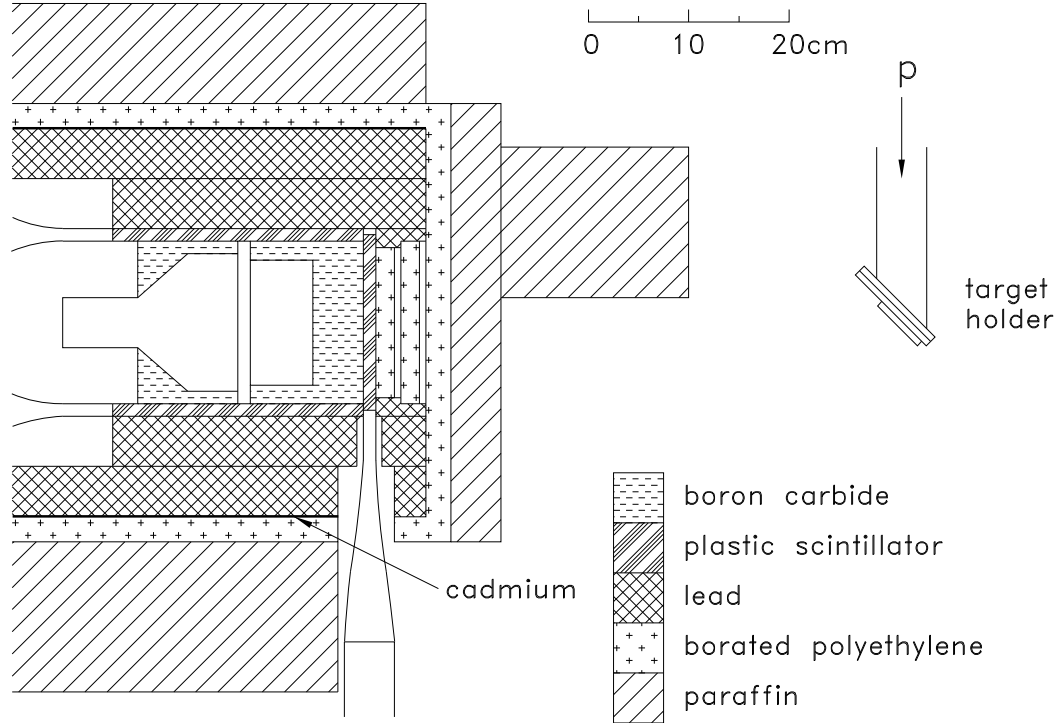


Figure 4.2: Schematic diagram of the spectrometer and target system used for the resonance reaction measurements.

emission angles of the gamma rays are sampled from the published angular distributions.

4.2.2 Experimental and Calculated Results

The $^{27}\text{Al}(p, \gamma)^{28}\text{Si}$ Reaction

The 992 keV resonance of the $^{27}\text{Al}(p, \gamma)^{28}\text{Si}$ reaction was used to produce 10.76 MeV gamma rays. A thick target was prepared by evaporating aluminum onto a 0.5 mm thick tantalum blank in an evacuated chamber. The target was mounted at an angle of 45° with respect to the beam direction. The measured yield curve (150 μC per point) is shown in Figure 4.3. Also shown in the figure is the calculated yield curve for a 60 $\mu\text{g}/\text{cm}^2$ thick target, scaled to the same area. The calculated yield was obtained by numerically evaluating the integral [Go59]

$$y(E_b, t) = n \int_{x=0}^t \int_{-\infty}^{+\infty} \int_{-\infty}^{+\infty} \sigma(E) g(E_b - E_1) W_{ER}(E_1 - E, x) dE dE_1 dx \quad (4.2)$$

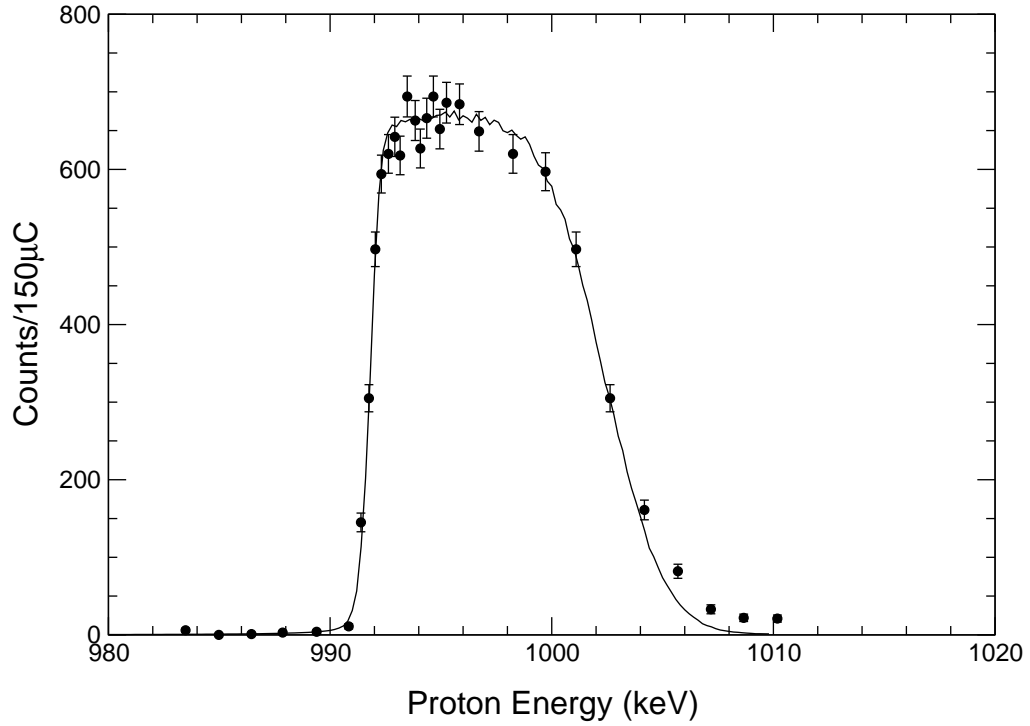


Figure 4.3: Measured and calculated yields for the $^{27}\text{Al}(p,\gamma)^{28}\text{Si}$ reaction at $E_p=992$ keV. The calculations are for a $60 \mu\text{g}/\text{cm}^2$ thick target.

where E_b is the mean beam energy, t is the target thickness (g/cm^2), and n is the density of the target atoms (atoms/g). The function $g(E_b - E_1)dE_1$ is the probability that an incident particle has an energy between E_1 and E_1+dE_1 , and is taken to be a normalized gaussian distribution centered on E_b with full width at half maximum of 0.7 keV. The function $W_{E_R}(E_1 - E, x)dE$ is the probability that an incident particle of energy E_1 has an energy between E and $E+dE$ at a depth of $x \text{ g}/\text{cm}^2$, and is assumed to be a normalized gaussian distribution centered on the expected energy $\langle E(x) \rangle$ of the proton at position x . The expected energy was calculated using the range-energy tables of J.F. Janni [Ja82]. The standard deviation of the distribution is the energy straggle Ω , calculated using the empirical formula given by Q. Yang *et al.* [Ya91]. The cross section $\sigma(E)$ is expressed using

the Breit-Wigner formula

$$\sigma(E) = \sigma_R \frac{(1/4)\Gamma^2}{(E - E_R)^2 + (1/4)\Gamma^2} \quad (4.3)$$

where $E_R = 991.88$ keV [En78] and $\Gamma = 105$ eV [Ma82] in the laboratory frame of reference. The cross section at resonance σ_R ($= \lambda^2 \omega_\gamma / \pi \Gamma$, where λ is the wavelength of the incident proton in the center of mass frame, and ω_γ is the partial width [Go59]) is assumed to be constant over the resonance. The target thickness t is varied in the calculations until the best fit to the data is obtained.

The shape of the measured yield curve is reproduced reasonably well by the calculations. The discrepancy in the high energy end of the curve is probably due to the tilting of the target, which makes the spread in the pathlengths through the target dependent on the divergence of the proton beam. The average proton energy loss through the target was 10.6 keV, which is much greater than the 105 eV width of the resonance. Hence, the thick target yield was measured at $E_b = 994.6$ keV for 5333 ± 1 μC of charge on the target. The digital storage oscilloscope was used to acquire the data. A. Anttila *et al.* [An77] give the yield of 10.76 MeV gamma rays to be $(8.27 \pm 0.49) \times 10^{-10}$ per incident proton. Thus, the total number of 10.76 MeV gamma rays produced during the measurement is expected to be $(2.75 \pm 0.16) \times 10^7$. The measured gamma ray spectrum is shown in Figure 4.4, along with the results of the Monte Carlo calculation for 10.76 MeV gamma rays only. The measured spectrum is corrected for deadtime losses, and the Monte Carlo results are normalized to the expected number of gamma rays produced in the target. The angular distribution of the gamma rays in the calculation was taken from [An77]. The Monte Carlo calculation reproduces the measured lineshape reasonably well. However, there is some indication that the first escape peak is too prominent in the calculated lineshape, and that some of the escaping energy should be deposited in the detector.

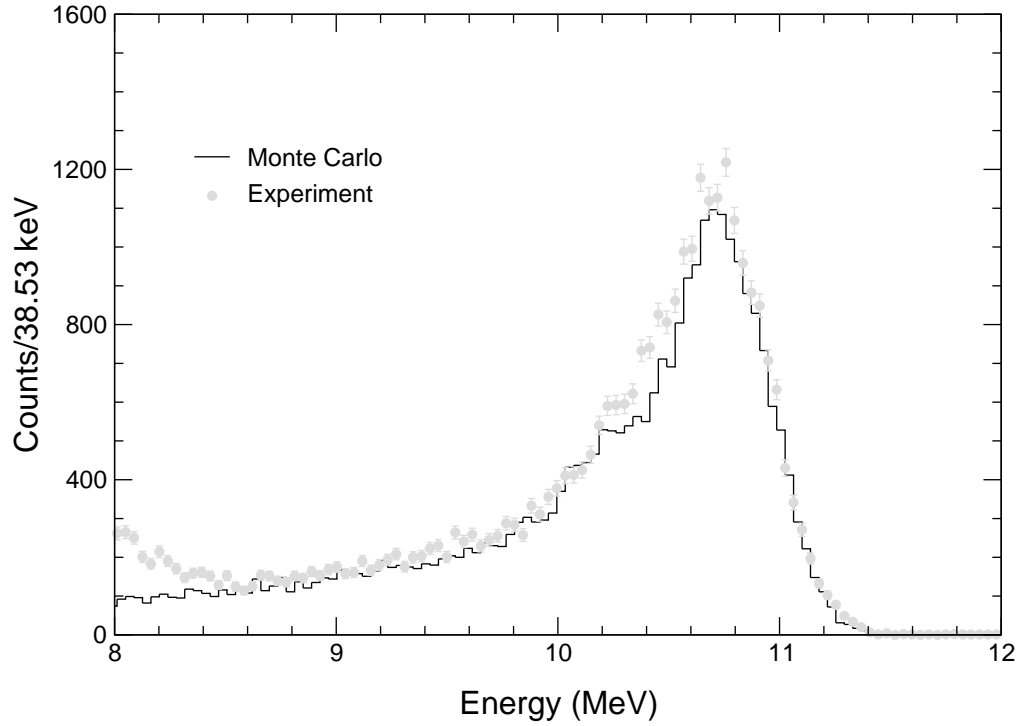


Figure 4.4: Measured and calculated spectra for 10.76 MeV gamma rays produced via the $^{27}\text{Al}(p,\gamma)^{28}\text{Si}$ resonance reaction at $E_p=992$ keV. The calculated spectrum is scaled to the expected number of gamma rays produced in the target.

The ratio of the number of counts within the region of interest between 8.81 and 11.49 MeV to the expected total number of 10.76 MeV gamma rays produced was measured to be $(1.064 \pm 0.063) \times 10^{-3}$, and was calculated from the Monte Carlo simulation to be $(1.005 \pm 0.006) \times 10^{-3}$ (statistical uncertainty only). Thus, the two results agree within one standard deviation.

The Monte Carlo program developed for the present work was also checked against the EGS4 code [Ne85] for the case of a bare $5'' \times 3''$ BGO crystal situated 30 cm from a point isotropic source of 10.76 MeV gamma rays. The spectra generated in the calculations were identical within the statistical uncertainties.

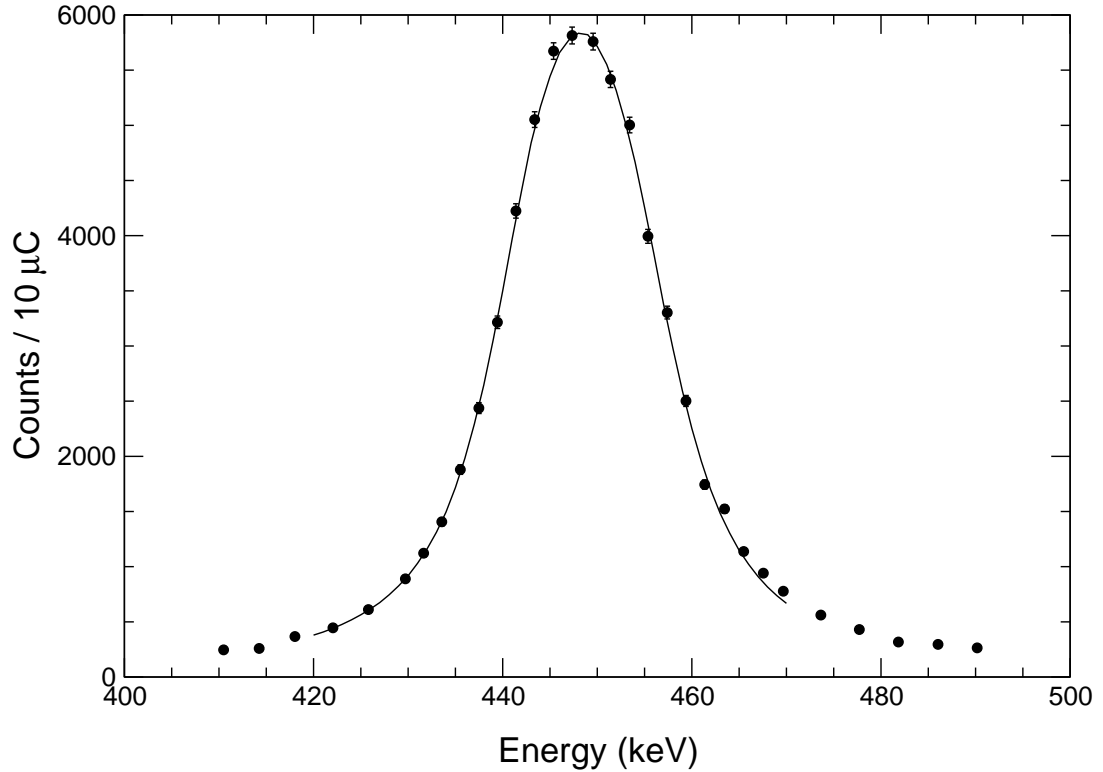


Figure 4.5: Measured and calculated yields for the ${}^7\text{Li}(p, \gamma){}^8\text{Be}$ reaction at $E_p=441$ keV. The calculations are for a $43 \mu\text{g}/\text{cm}^2$ thick LiF target.

The ${}^7\text{Li}(p, \gamma){}^8\text{Be}$ Reaction

The 441 keV resonance of the ${}^7\text{Li}(p, \gamma){}^8\text{Be}$ reaction was used to produce 17.6 MeV gamma rays. Due to the larger width of the resonance ($\Gamma_{lab} = 12.2$ keV) [Aj88] and a non-negligible off-resonance contribution to the yield [Fo48], a thin target was used for the measurement. The target was prepared by evaporating LiF onto a 0.5 mm thick tantalum blank, and was mounted in the same set-up as the aluminum target. To decrease the amount of sputtering of the target, the yield curve was measured using a $4'' \times 5''$ NaI detector, placed ~ 10 cm from the target at an angle of $\sim 110^\circ$ with respect to the beam direction. The measured yield curve (10 μC per point) is shown in Figure 4.5. The best fit to the data was obtained with the calculated yield curve for a $43 \pm 1 \mu\text{g}/\text{cm}^2$ thick target. The results are also shown in Figure 4.5, scaled to the same area. The proton energy loss through the target is ~ 14.5 keV.

The angular distribution of the radiation is isotropic only at the resonance energy, while the anisotropy varies with proton energy [De49]. Since the detector was placed at a backward angle, the measured yield may be skewed, and thus, the deduced thickness of the target may be inaccurate. However, it is shown below that the results of the calculation of the gamma ray yield are not sensitive to the deduced target thickness.

W.A. Fowler and C.C. Lauritsen [Fo49] measured the thick target yield for the ${}^7\text{Li}(p, \gamma)$ resonance from a lithium target (92.6% ${}^7\text{Li}$) to be $Y_{max}(\infty) = 1.90 \times 10^{-8} \gamma/\text{proton}$ (corrected for the non-resonant background), and the width to be $\Gamma = 12 \text{ keV}$. No uncertainties on the results were given. Using the expression for the cross section at resonance [Fo48]

$$\sigma_R = \frac{2\varepsilon Y_{max}(\infty)}{\pi\Gamma} \quad (4.4)$$

where ε is the stopping cross section (eV-cm²/target atom), a value of $\sigma_R = 6.0 \text{ mb}$ was calculated. However, the value of $\varepsilon = 5.95 \times 10^{-15} \text{ eV-cm}^2/{}^7\text{Li atom}$ used (obtained from [Li37]) is larger than the value $\varepsilon = 4.88 \times 10^{-15} \text{ eV-cm}^2/{}^7\text{Li atom}$ calculated from modern values of the stopping power [Ja82]. Using the modern value of ε , and $\Gamma = 12.2 \text{ keV}$, a value of $\sigma_R = 4.83 \text{ mb}$ is obtained for use in eqn.(4.2).

To calculate the yield of gamma rays, the atomic density n (atoms/g) of the ${}^7\text{Li}$ must be known. This quantity was deduced from measurements of the ${}^7\text{Be}$ activity produced in the target via the ${}^7\text{Li}(p, n){}^7\text{Be}$ reaction. The ${}^7\text{Be}$ decays by electron capture to ${}^7\text{Li}$ with a half-life of $53.29 \pm 0.07 \text{ d}$ [Aj88], 10.52% of the decays being to the first excited state at 477.6 keV [Aj88]. The target was bombarded by $Q = 3 \times 10^{-3} \text{ C}$ of 2.00 MeV protons. The gamma ray activity of the target was measured afterwards using the method described in Section 5.2, and the number of ${}^7\text{Li}(p, n)$ reactions produced was deduced to be $N_{pn} = (4.16 \pm 0.05) \times 10^9$. The cross section for the reaction is $\sigma_{pn} = 269 \pm 13 \text{ mb}$ [Li75],

hence, the areal density of the ${}^7\text{Li}$ atoms was

$$\frac{N_{pn}}{(Q/e)\sigma_{pn}} = (8.26 \pm 0.43) \times 10^{17} \quad (4.5)$$

Thus, the atomic density of ${}^7\text{Li}$ atoms was $n=(8.26\pm 0.43)\times 10^{17}/t$, where t (g/cm^2) is the target thickness.

The calculated yield from eqn.(4.2) depends explicitly on the target thickness t since it is one of the limits of the integration. W.A. Fowler et al [Fo48] show that, for a ξ keV thick target ($\xi \simeq t(-dE/dx)$), the maximum yield $Y_{max}(\xi)$ is proportional to $\arctan(\xi/\Gamma)$. The yield is also implicitly dependent on the thickness in the present calculations through the measured density of the target atoms $n=(8.26\pm 0.43)\times 10^{17}/t$. Hence, the calculated maximum yield is proportional to $\arctan(t(-dE/dx)/\Gamma)/t$. For a deduced target thickness $t = 43\pm 1 \mu\text{g}/\text{cm}^2$, $-dE/dx = 0.338 \text{ keV}/(\mu\text{g}/\text{cm}^2)$ [Ja82], and $\Gamma = 12.2 \text{ keV}$, the uncertainty in the maximum yield is $\pm 1.0\%$. Thus, the calculated value for the maximum yield is not sensitive to the deduced target thickness.

The 441 keV resonance reaction populates the 1^+ state of ${}^8\text{Be}$ at $E_x = 17.642 \text{ MeV}$ [Aj88]. The nucleus subsequently decays predominately to either the 0^+ ground state or the broad 2^+ first excited state at $E_x = 2.94 \text{ MeV}$ with branching ratios on resonance of 67% and 33%, respectively [Aj88]. The total branching ratio for all other decays is $\sim 0.1\%$. The angular distribution of the radiation is nearly isotropic [Aj88]. For the decay to the first excited state, the multipolarity of the radiation is predominately M1 [Aj88]. Hence, the probability of emitting a gamma ray of energy E_γ in the center-of-mass frame is proportional to E_γ^3 , and to the spectral density function $\chi(E_x)$ for the first excited state ($E_x(\text{MeV}) = 17.642 - E_\gamma$). During the Monte Carlo simulation of this decay, the gamma ray energy in the center-of-mass frame is sampled from a E_γ^3 distribution convolved with a fit [No91] to the spectral density function calculated by G.J. Clark *et al.* [Cl69] from the β -decay of

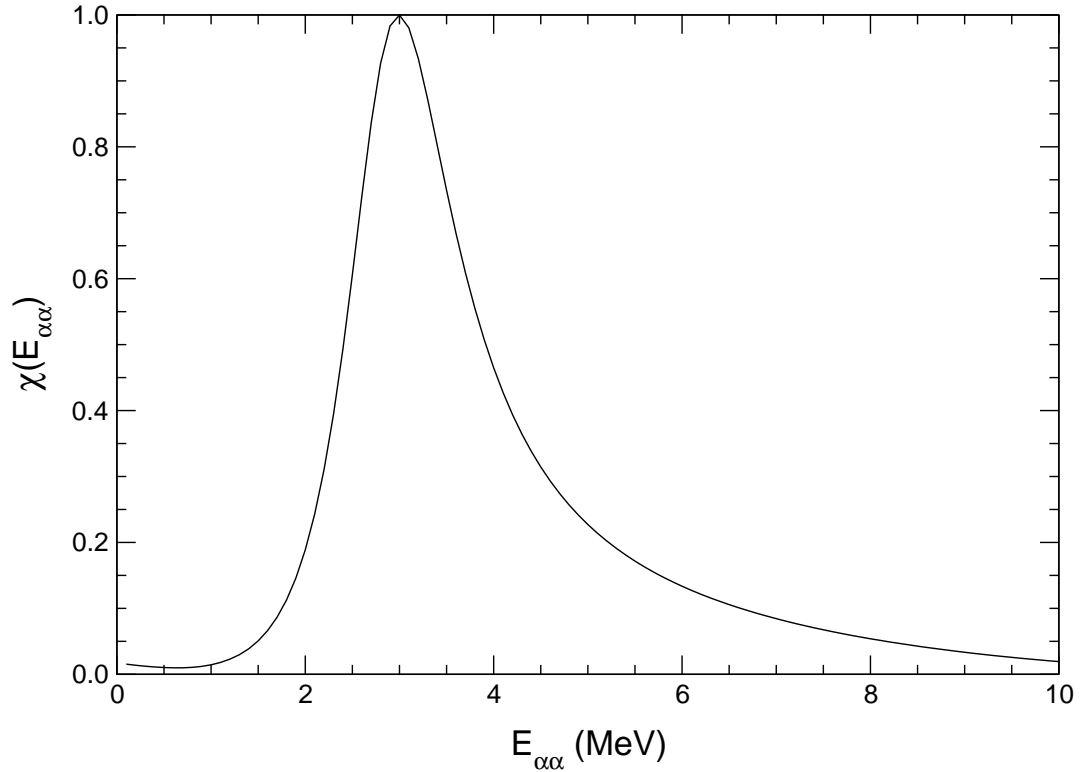


Figure 4.6: The fitted spectral density function $\chi(E_{\alpha\alpha})$ for the first excited state of ${}^8\text{Be}$ ($E_{\alpha\alpha}=E_x+0.092$ MeV), from [No91].

${}^8\text{B}$. The fit to the spectral density function is shown in Figure 4.6. The gamma rays from the decay to the ground state are given an energy of 17.642 MeV in the center-of-mass frame. The initial direction of motion of each gamma ray is sampled from an isotropic distribution in the laboratory reference frame, and the energy in that frame is calculated from the transformation of E_γ selected above.

The gamma ray spectrum was measured for 1000 ± 1 μC of 448.4 keV protons on target using the QDC in the CAMAC system. The expected number of gamma rays produced in a 43 ± 1 $\mu\text{g}/\text{cm}^2$ LiF target calculated using eqn.(4.3) is $(1.82\pm 0.10)\times 10^7$ (the uncertainty does not include the unknown contribution from σ_R). Figure 4.7 shows the deadtime corrected spectrum, along with the results of the Monte Carlo simulation normalized to the expected number of gamma rays. The ratio of the number of counts within the region of interest be-

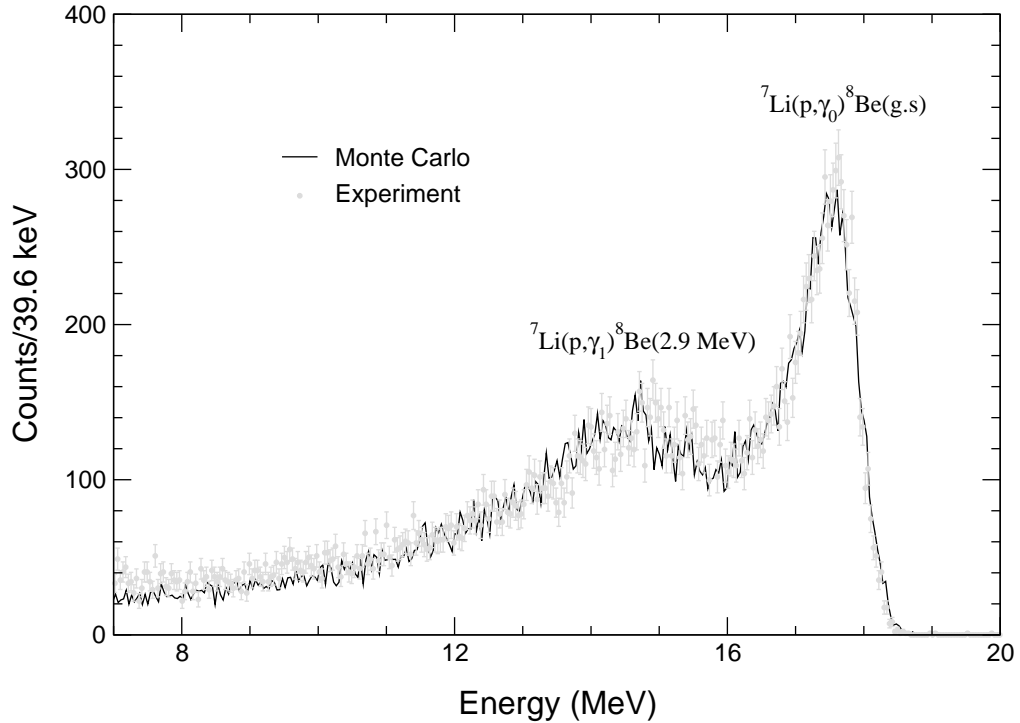


Figure 4.7: Measured and calculated ${}^7\text{Li}(p, \gamma){}^8\text{Be}$ spectra for the usual geometry.

tween 7.73 to 18.68 MeV to the expected number of gamma rays produced is measured to be $(1.430 \pm 0.076) \times 10^{-3}$. The Monte Carlo simulation predicts a ratio of $(1.385 \pm 0.007) \times 10^{-3}$ (statistical uncertainty only). The two results agree within one standard deviation.

The last measurement was repeated with the paraffin, borated polyethylene and borated paraffin between the BGO detector and the target system removed. The deadtime corrected spectrum and the results of the Monte Carlo calculation scaled to the same expected number of gamma rays produced are shown in Figure 4.8. The measured ratio of the counts between 7.73 to 18.68 MeV to the expected number of gamma rays produced is $(1.66 \pm 0.09) \times 10^{-3}$, and is in good agreement with the Monte Carlo simulation prediction of $(1.662 \pm 0.006) \times 10^{-3}$ (statistical uncertainty only). The ratio of the results with and without the shielding materials is measured to be 0.861 ± 0.008 , and is calculated from the simulation to be 0.833 ± 0.005 . Hence, it can be seen that the Monte Carlo simulation

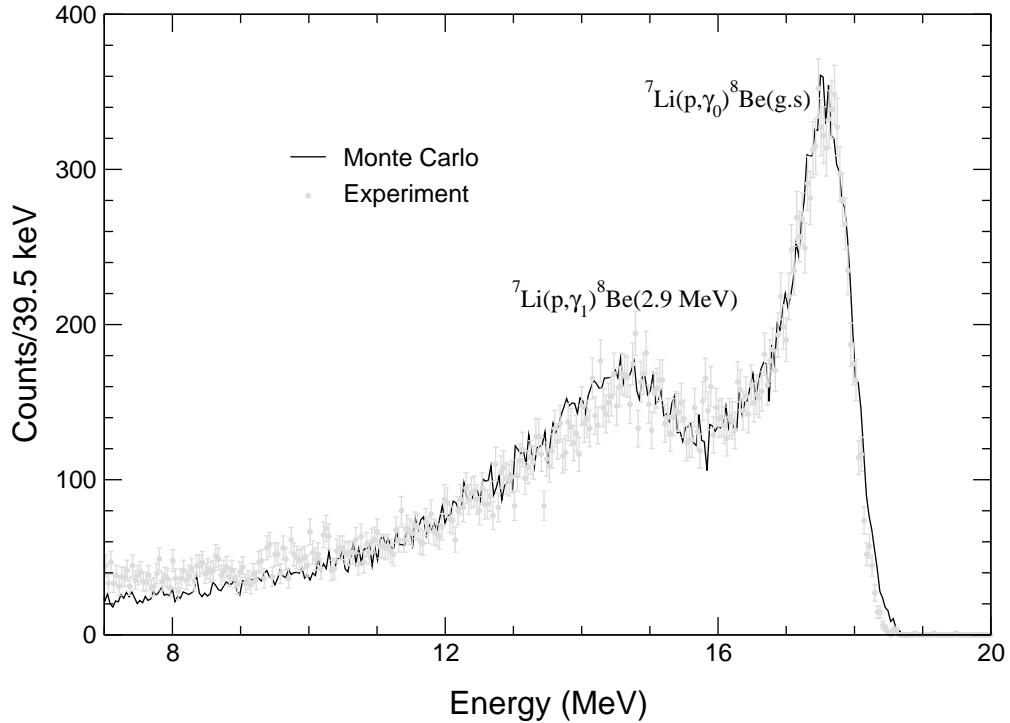


Figure 4.8: Measured and calculated ${}^7\text{Li}(p, \gamma){}^8\text{Be}$ spectra with some of the shielding removed.

overestimates the attenuation of the gamma rays through the shielding materials by $3 \pm 1\%$.

This is discussed in more detail in the next section.

4.3 Systematic Uncertainties

From the results of the tests, it appears that the physics embodied in the program for gamma ray tracking simulates the actual interactions with reasonable accuracy. The largest contributions to the systematic uncertainties in the gamma ray tracking come from the cross sections and the geometry used in the program. For gamma ray energies above 15 MeV, the microscopic cross sections are accurate to $\pm 3\%$ for Compton scattering and $\pm 5\%$ for pair production [St70]. The geometry and atomic composition of the ${}^3\text{He}$ target system, borated polyethylene, plastic scintillator and boron carbide powder are well known, and the uncertainty in the attenuation of the gamma rays through that part of the system is

estimated to be $\pm 0.9\%$. The 3% overestimation of the gamma ray attenuation through the front shielding materials seen in the ${}^7\text{Li}(p, \gamma)$ resonance measurements is due in part to the fact that the complex geometry of the paraffin shielding is modelled less accurately than the other components. Also, for the sake of convenience, the borated paraffin is assumed to have the same cross section as the borated polyethylene, and this causes the attenuation of 20 MeV gamma rays to be underestimated by $\sim 0.8\%$. The results of the simulations of the ${}^3\text{He}(n, \gamma)$ experiments were corrected for the 3% excess attenuation. The overall uncertainty in the corrected attenuation is estimated to be $\pm 1.3\%$.

The uncertainty in the calculation of the response function of the detector includes the uncertainty in the probability of interaction of gamma rays within the crystal, and the uncertainty in reproducing the shape of the spectrum. From the microscopic cross sections given in [St70], the mean free path of 20 MeV gamma rays in BGO is $0.357 \pm 0.015 \text{ cm}^{-1}$, hence, the probability of interacting in 7.62 cm of BGO is 0.934 ± 0.008 . It is difficult to determine the uncertainty in reproducing the shape of the spectrum, since a source of monoenergetic gamma rays with $E_\gamma \sim 20 \text{ MeV}$ was not readily available for direct comparison. However, the comparisons with the results of the resonance reaction measurements indicate that the spectral shape is reproduced with reasonable accuracy.

The largest uncertainty in the simulation is due to the neutron tracking. For the materials in the target systems such as tantalum, water, cadmium and ${}^3\text{He}$, the cross sections are relatively smooth over energy scales of $\sim 50 \text{ keV}$ (ie. the spread in neutron energies in the ${}^3\text{He}$). Hence, the uncertainty in the attenuation of the neutrons through these materials is dominated by the uncertainty in the microscopic cross sections. If the spread in the microscopic cross section data is used as the uncertainty on the recommended value, the uncertainty in the attenuation of the neutrons through the materials given above

is typically $\leq 1\%$. The uncertainty in the attenuation through the steel, however, is larger for several reasons:

i) to simplify the calculation of the cross sections, the steel is modelled as pure iron in the simulations.

ii) there are many narrow resonances between 10 keV and 2 MeV. The evaluated experimental cross sections vary by as much as a factor of two or more over this region [Mc88], and thus, the uncertainty in the cross sections is large.

iii) the cross sections are calculated during the simulations by interpolating from tables compiled from the graphical data in [Mc88]. Due to the high density of the resonances, it is difficult to accurately reproduce the recommended cross sections for iron in tabular form. Instead, near the neutron production energies, the cross sections at the peak and dip of large resonances are included in the tables, and groupings of smaller resonances are averaged over before inclusion in the tables. Away from the neutron production energies, the cross sections are crudely averaged over energy scales of hundreds of keV.

iv) the cross sections can change substantially over an energy scale of 10 keV. Thus, the calculated attenuation of neutrons will depend on the neutron energy distribution, which depends on the proton energy loss through the lithium target. Water contamination in the target would increase the spread in the neutron energies, and thus, could affect the attenuation calculations if there is a narrow resonance in the cross section nearby.

Due to these factors, it is estimated that the uncertainty in the neutron flux after passing through the steel is $\pm 5\%$.

The total number of neutrons passing through the ^3He gas target during each run was deduced from the activity measurement of the lithium target, and from the angular distribution for the $^7\text{Li}(p, n)$ reaction. The latter was obtained from [Li75] in the form of

coefficients for an expansion in Legendre polynomials, as given by

$$\left(\frac{d\sigma}{d\Omega}(\theta)\right)_{CofM} = \left(\frac{d\sigma}{d\Omega}(0^\circ)\right)_{CofM} \cdot \sum_i A_i P_i(\cos\theta) \quad (4.6)$$

The sum of the coefficients A_i is equal to one. The uncertainty on each coefficient was stated to be ± 0.03 , however, the correlations between the coefficients are not known. As an estimate of the uncertainty on the total number of neutrons entering the gas target, the standard deviation of the total number was calculated assuming random correlations between the coefficients. The uncertainty in the total was typically $\pm 1.3\%$.

Unlike the gamma ray tracking part of the simulation, the neutron tracking part was not verified experimentally. The ^3He proportional counter used as the gas target could have been used to measure the neutron flux, however, this was not done for two reasons. Firstly, the response function of the counter is not known. This can be calculated using a Monte Carlo simulation, however, the calculation would be difficult and was not attempted here. Secondly, the resolution of the counter is poor ($\sim 11\%$ for the epithermal peak), and the measured spectrum would not reveal the details in the neutron energy distribution on the scale of ~ 10 keV necessary for verifying the program. Examples of measured spectra are shown in Figures 2.3 (page 21) and 2.4 (page 22), and reveal the difficulty in measuring small differences in neutron fluxes with the present system. Hence, the neutron tracking part of the code was not verified experimentally because the measurements would not be accurate enough.

Combining the uncertainties from the neutron production and tracking, and from the gamma ray tracking parts of the simulation results in an overall systematic uncertainty of $\sim 5.7\%$ in the Monte Carlo calculation of the response of the gamma ray spectrometer.

Chapter 5

Procedure, Results and Analysis

In this chapter, the procedure, results and analysis for each step in the experiment are given. The steps are described under the broad headings of data collection, activity measurements, pulse processing into spectra, Monte Carlo simulations, and extraction of the cross section.

5.1 Data Collection

Measurements of the ${}^3\text{He}(n, \gamma)$ cross section were made at five proton energies. Table 5.1 shows the proton energy, target thickness and beam current used in each run. Also shown are the maximum neutron energies from the ${}^7\text{Li}(p, n_0){}^7\text{Be}(\text{g.s.})$ and ${}^7\text{Li}(p, n_1){}^7\text{Be}(0.43 \text{ MeV})$ reactions, labelled $(E_{n0})_{max}$ and $(E_{n1})_{max}$, respectively. The thicknesses were measured using a calibrated quartz crystal during the production of the targets, and were multiplied by $\sqrt{2}$ to account for the 45° tilt of the targets relative to the proton beam direction. The thicknesses are estimated to be accurate to $\pm 10\%$. The spectra collected over each run are shown in Section 5.3. In the following descriptions, the measurements of the ${}^3\text{He}(n, \gamma)$ cross section performed with the ${}^3\text{He}$ gas counter in place are referred to as *gas in* measurements, and the background measurements performed with the ${}^3\text{He}$ counter removed are referred to as *gas out* measurements.

The following steps were taken during each measurement: i) At the start of each run,

Table 5.1: Particulars of each data run

E_p (MeV)	Li thickness ($\mu\text{g}/\text{cm}^2$)	Gold thickness ($\mu\text{g}/\text{cm}^2$)	$I(\mu\text{A})$	$(E_{n0})_{max}$ (MeV)	$(E_{n1})_{max}$ (MeV)
1.93	140	25	16	0.135	-
2.30	140	42	15.5	0.571	-
2.77	170	25	17	1.068	0.576
3.22	170	34	13	1.530	1.060
3.68	170	25	13	1.999	1.538

the shadowbar was replaced by paraffin, the ^3He gas target was removed, and a spectrum (7000 events) of the gamma rays from the $^7\text{Li}(p, \gamma)$ reaction was acquired over a period of ~ 5 min. These spectra are used in calibrating the energy response of the spectrometer.

ii) The shadowbar and ^3He gas target were replaced, and the *gas in* data were collected over a period of ~ 48 hours. iii) The ^3He target was removed and the shadowbar was replaced by paraffin again, and a second $^7\text{Li}(p, \gamma)$ spectrum was acquired. iv) The lithium target and the aluminum foil liner in the target holder arrangement were removed and replaced with a new target and liner. v) A third $^7\text{Li}(p, \gamma)$ spectrum was acquired. vi) The shadowbar was placed in position, and an equal mass of steel pipe was used to replace the ^3He gas target. The *gas out* data were then collected over a period of ~ 24 hours. vii) The shadowbar was replaced by paraffin, the steel pipe was removed, and a fourth $^7\text{Li}(p, \gamma)$ spectrum was acquired. viii) The target and liner were removed and put aside for the activity measurements.

Figure 5.1 shows the dead-time corrected energy spectrum above ~ 1 MeV for a $^7\text{Li}(p, \gamma)$ measurement at $E_p=2.30$ MeV. The spectrum was collected using the Lecroy 2249 W QDC and CAMAC system used for the resonance reaction measurements (cf. Section 4.2.1). The count rate in the BGO detector was ~ 20 kcps, and was almost entirely due to the neutron capture background. The spectrum shows that data collection using a discriminator level set below 11 MeV would be impractical with the present pulse digitizing

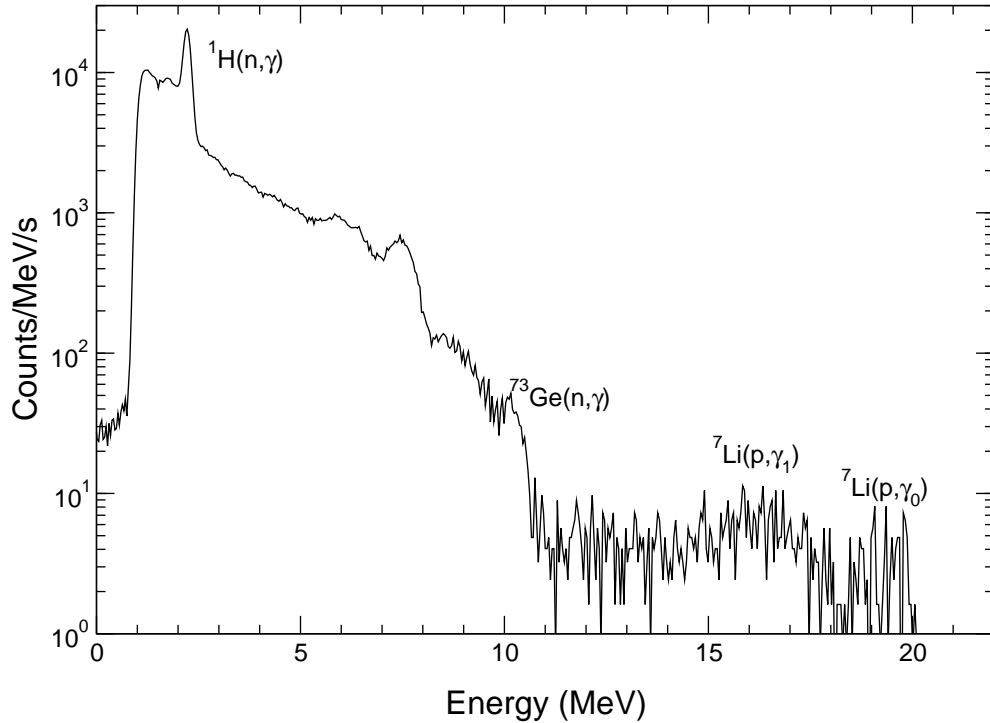


Figure 5.1: The deadtime corrected ${}^7\text{Li}(p, \gamma)$ spectrum and background above ~ 1 MeV, collected using the Lecroy 2249 W QDC and CAMAC system.

and analysis system.

The activities of the targets and aluminum liners were measured afterwards (see below) to determine the total number of neutrons produced with each target. The number of neutrons detected in the Bonner sphere, the charge on target and the elapsed time were recorded after each data collection step, so that the fraction of the neutrons produced during the actual *gas in* or *gas out* measurements (ie. apart from the ${}^7\text{Li}(p, \gamma)$ measurements) could be calculated. This fraction was typically 0.9920 ± 0.0007 .

While removing the target from the *gas in* run at $E_p = 2.77$ MeV, some water which had condensed on the outside of the target holder arrangement ran over the outside part of the surface of the target, missing most of the area hit by the beam. It is not known how much, if any, of the ${}^7\text{Be}$ was washed off, however, the measurements of the activity of flakes from other targets (see below) indicate that most of the ${}^7\text{Be}$ is implanted in the

target backing upon production. Hence, it is not expected that much of the ${}^7\text{Be}$ was lost. A conservative estimate of the loss is $10\pm 10\%$, based on the affected area of the target. This estimate was used to correct the deduced number of ${}^7\text{Li}(p, n)$ reactions which had occurred in the target.

With the beam off, a cosmic ray spectrum was collected over a period of 119 hours. The collection was started immediately after one of the ${}^7\text{Li}(p, \gamma)$ resonance reaction measurements was completed, allowing a calibration of the energy response of the spectrometer at the start of the collection period.

5.2 Activity Measurements

The ${}^7\text{Be}$ produced through the ${}^7\text{Li}(p, n){}^7\text{Be}(\text{g.s.}+0.43 \text{ MeV})$ reaction in the targets decays by electron capture to ${}^7\text{Li}$, 10.52 \pm 0.06% of the decays being to the first excited state at 447.6 keV [Aj88]. By measuring the gamma ray activity of the targets and aluminum liners, the total number of ${}^7\text{Be}$ atoms produced can be deduced. The activities were measured using a closed-ended coaxial germanium detector with a volume of 84 cm³. The samples were placed 58.4 cm from the detector along its axis. The absolute full energy peak efficiency of the detector for this geometry was measured using calibrated ${}^{133}\text{Ba}$, ${}^{22}\text{Na}$, ${}^{137}\text{Cs}$, ${}^{54}\text{Mn}$ and ${}^{60}\text{Co}$ sources. The half-lives and branching ratios for all of the decays were obtained from [Le78]. The results of the measurement are shown in Figure 5.2, along with the results of a least-squares fit with the six-parameter function [Kn89, and the references therein]

$$\varepsilon = \left(\frac{a_1}{E}\right)^{a_2} + a_3e^{-a_4E} + a_5e^{-a_6E} \quad (5.1)$$

From the fit, the absolute full energy peak efficiency for detecting 477.6 keV gamma rays is $\varepsilon=(10.881\pm 0.069)\times 10^{-5}$.

If N_γ counts are detected in the photopeak with a fractional detector livetime of FLT ,

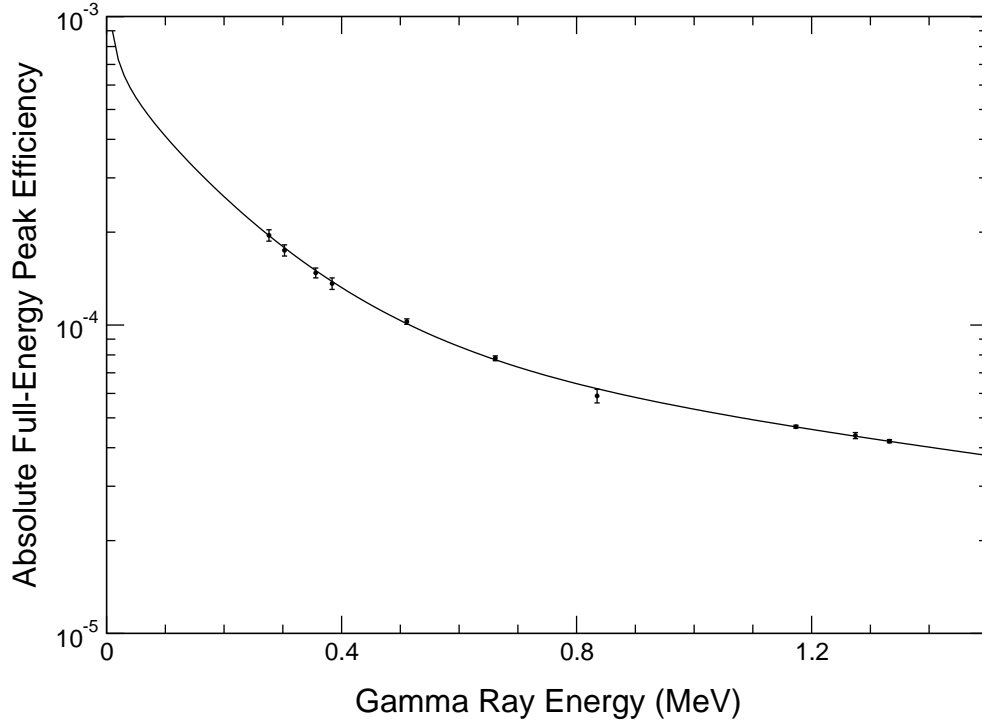


Figure 5.2: Absolute full energy peak efficiency of the germanium detector used to measure the target activities, and the results of a fit to eqn.(5.1).

the number of decays N in the target was

$$N = \frac{N_{\gamma}}{\varepsilon \cdot BR \cdot FLT} \quad (5.2)$$

where $BR=0.1052\pm 0.0006$ is the branching ratio for the decay to the first excited state.

Assuming a constant rate of production of ${}^7\text{Be}$ in the target, the number of ${}^7\text{Be}$ atoms produced N_{Be} is calculated from

$$N_{Be} = \frac{N\lambda t_{bo}}{(1 - e^{-\lambda t_{bo}})e^{-\lambda t_1}(1 - e^{-\lambda \Delta t})} \quad (5.3)$$

where $\lambda=(1.5055\pm 0.0020)\times 10^{-7} \text{ s}^{-1}$ is the decay constant for the decay of ${}^7\text{Be}$ [Aj88], t_{bo} is the time over which the ${}^7\text{Be}$ was produced, t_1 is the time at which the activity measurement was started with respect to the time at which the ${}^7\text{Be}$ production was ended, and Δt is the true time over which the activity was measured.

The amount of ${}^7\text{Be}$ sputtered from each target was calculated from the activity of

Table 5.2: Neutron Production During Data Collection

E_p (MeV)	N_{Be} (^3He gas in)	N_{Be} (^3He gas out)
1.93	$(5.149 \pm 0.048) \times 10^{13}$	$(2.859 \pm 0.034) \times 10^{13}$
2.30	$(1.157 \pm 0.011) \times 10^{14}$	$(6.603 \pm 0.068) \times 10^{13}$
2.77	$(8.39 \pm 0.94) \times 10^{13}$	$(3.418 \pm 0.050) \times 10^{13}$
3.22	$(6.597 \pm 0.062) \times 10^{13}$	$(3.323 \pm 0.039) \times 10^{13}$
3.68	$(4.949 \pm 0.052) \times 10^{13}$	$(2.887 \pm 0.035) \times 10^{13}$

the aluminum liner, and was typically less than 1% of the total amount. However, for the $E_p=3.22$ and 3.68 MeV data runs, some flaking of the lithium from the targets was observed. The flakes were collected on the aluminum liners, and their activity was measured along with that of the sputtered atoms. In both cases, the amount of ^7Be measured on the liner was less than 2% of the total amount in the target. Hence, most of the ^7Be is probably implanted into the tantalum backing on production, and little is lost to sputtering or flaking.

Table 5.2 shows the total number of ^7Be atoms produced during each data collection run. The figures include the contribution from the sputtered atoms and those in the flakes, but exclude the fraction produced during the $^7\text{Li}(p, \gamma)$ measurements. The value of N_{Be} for the target used during the *gas in* run at $E_p=2.77$ MeV was corrected for the estimated loss of $10 \pm 10\%$ of the ^7Be .

5.3 Pulse Processing into Spectra

5.3.1 $^7\text{Li}(p, \gamma)$ Spectra

The first step in the analysis of the raw data is the processing of the $^7\text{Li}(p, \gamma)$ events. These events were collected over a short period of ~ 5 min each time, hence, it is assumed that there were no gain variations during the measurements. The event rate above the 13 MeV discriminator level during these measurements was ~ 30 cps. The rate with the shadowbar in place was ~ 0.15 cps, and most of the counts are due to $^7\text{Li}(p, \gamma)$ gamma rays

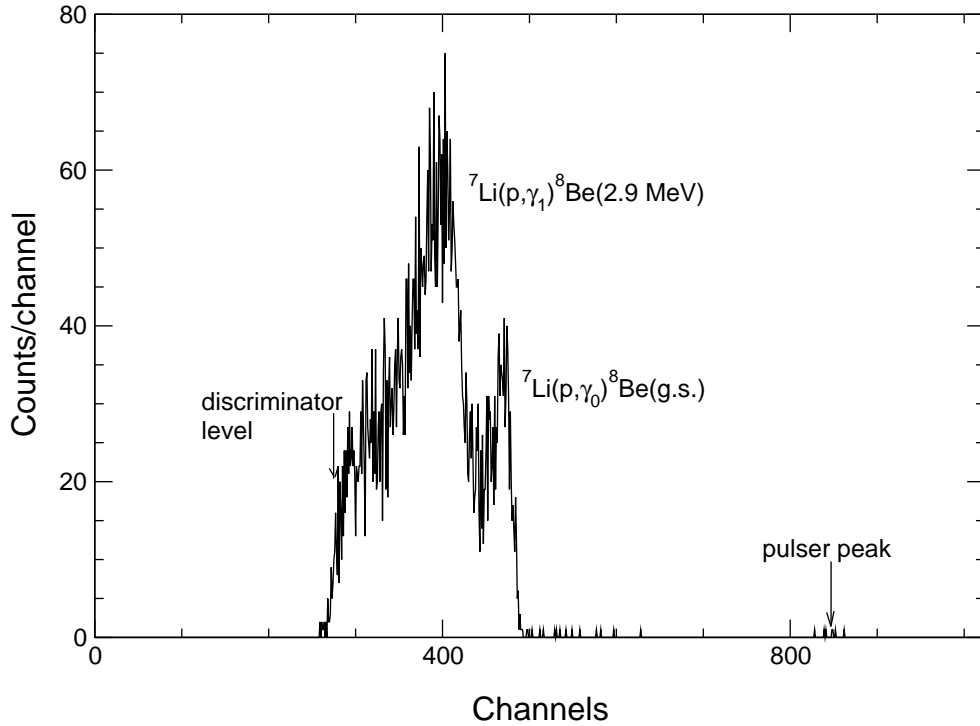


Figure 5.3: ${}^7\text{Li}(p, \gamma)$ spectrum from the start of the $E_p=2.30$ MeV run. The discriminator level is at ~ 13 MeV.

that leak through the shadowbar. Hence, it is assumed in the analysis that all of the pulses are produced by gamma rays from the ${}^7\text{Li}(p, \gamma)$ reaction. Also, the analysis of the data collected with the shadowbar in place indicates that $\leq 10\%$ of the counts are due to pile-up, that is, the pile-up rate is ≤ 0.015 cps. The pile-up rate with the shadowbar removed should be similar, since most of the pile-up is due to the neutron capture background. Hence, it is assumed in the analysis that all of the pulses collected without the shadowbar are pile-up free.

The events were processed as single pulses, and distributions of the charge of the pulse (ie. deposited energy), rise time and fall time constants, and $\chi_R^2/(\text{pulse area})^2$ ($\equiv \chi_{R/A}^2$) were obtained for each measurement. Figure 5.3 shows a typical energy spectrum obtained at $E_p=2.30$ MeV; all of the other ${}^7\text{Li}(p, \gamma)$ spectra are similar. From the positions of the ${}^7\text{Li}(p, \gamma_0){}^8\text{Be}(\text{g.s.})$ peak in the spectra, the gain of the system is determined before and

after each *gas in* and *gas out* data run. The average charge of the LED pulser events is also calculated for each measurement, however, the uncertainty in the result is relatively large ($\pm 2-5$ channels) because there are typically only six LED pulser events detected over the 5 min collection period. Hence, to improve the statistics, LED pulser events collected at the beginning and end of each *gas in* and *gas out* run were also included in the calculation of the average charge.

The distributions of θ^{-1} and λ^{-1} , and of $\chi_{R/A}^2$ are shown in Figures 5.4 and 5.5, respectively, for the ${}^7\text{Li}(p, \gamma)$ events collected over each run. From these distributions, the acceptance cuts for the fitting parameters were defined as $44 \text{ ns} \leq \theta^{-1} \leq 69 \text{ ns}$, $\chi_{R/A}^2 \leq 0.55$, and $210 \text{ ns} \leq \lambda^{-1} \leq 360 \text{ ns}$ for the first four data runs ($E_p=2.30$ to 3.68 MeV), and $220 \text{ ns} \leq \lambda^{-1} \leq 400 \text{ ns}$ for the last data run ($E_p=1.93$ MeV). The distributions of λ^{-1} indicate that the decay constant of the BGO crystal increased with each run. However, the value of the decay constant is strongly temperature dependent ($d\lambda/dT \simeq -6.5 \text{ ns}/^\circ\text{C}$ at room temperature [Me85]), and the values obtained during the measurements are consistent with those measured by [Me85] between 15 and 25 $^\circ\text{C}$. Hence, the different values for the decay constant are probably due to different ambient temperatures during the measurements.

5.3.2 ${}^3\text{He}(n, \gamma)$ and Background Spectra

As described in Section 3.2.2, the raw data from the ${}^3\text{He}$ *gas in* and *gas out* runs were processed twice. On the first pass, the gain correction factors were determined from the LED pulser events and the results of the ${}^7\text{Li}(p, \gamma)$ measurements. On the second pass, the charges of the fitted and the deconvoluted scintillator pulses were gain corrected and sorted into spectra. Both passes will now be described in more detail.

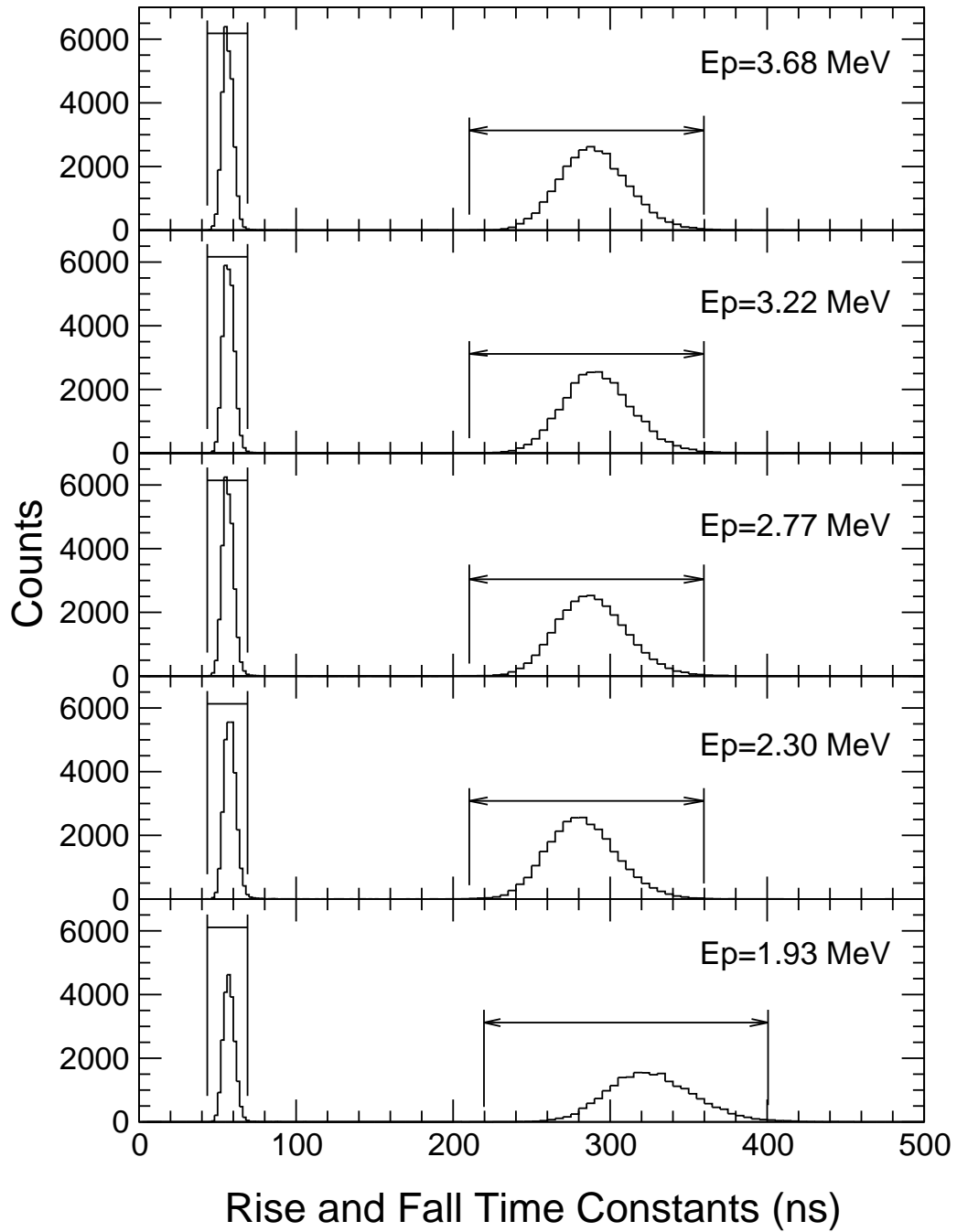


Figure 5.4: The sum of the distributions of θ^{-1} and λ^{-1} from the ${}^7\text{Li}(p, \gamma)$ events for each experiment. The θ^{-1} distributions are centered around ~ 60 ns, and the λ^{-1} distributions are centered around ~ 300 ns. The acceptance cuts for scintillator pulses defined by the distributions are also shown.

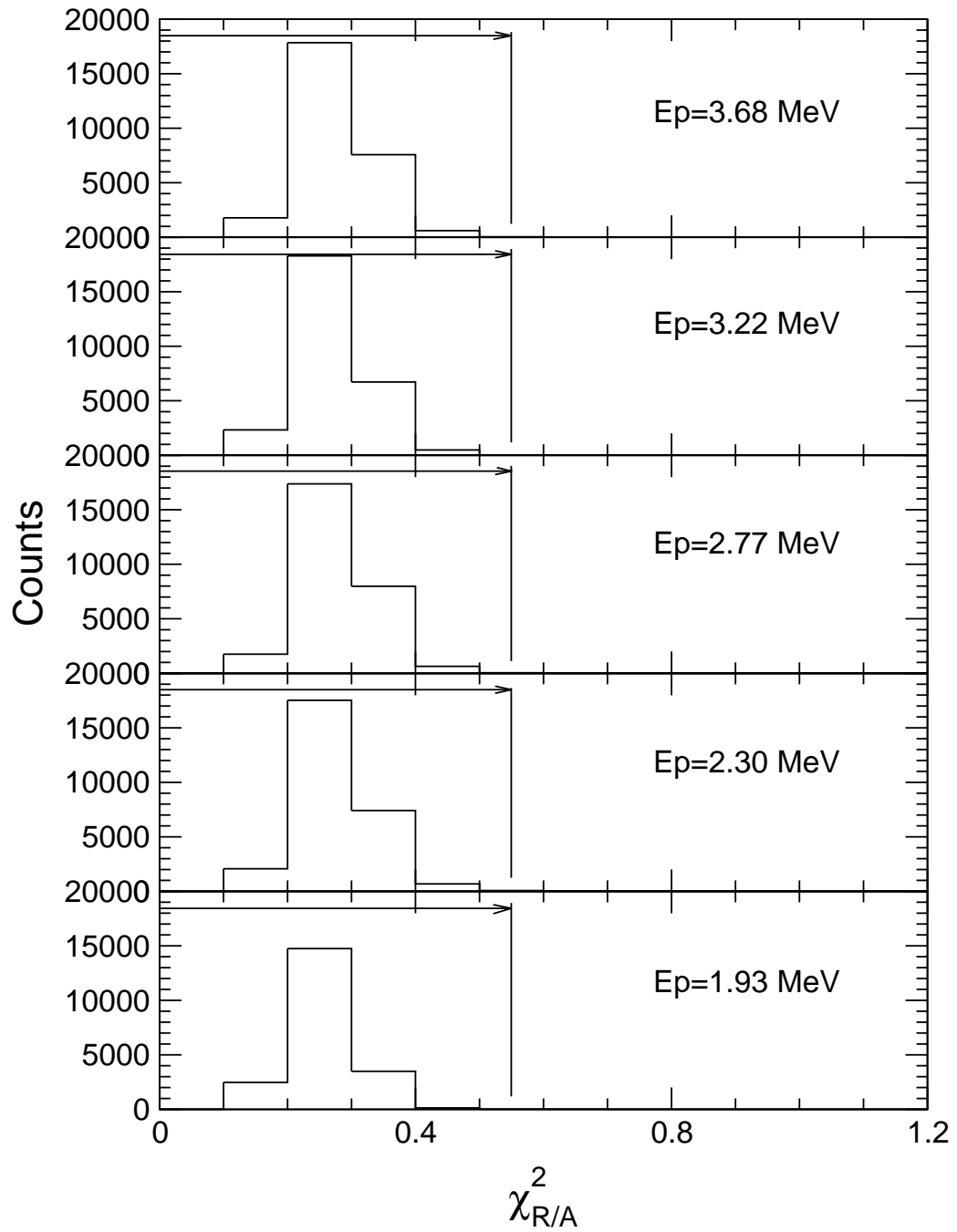


Figure 5.5: The sum of the distributions of $\chi^2_{R/A}$ from the ${}^7\text{Li}(p, \gamma)$ events for each experiment. The acceptance cut for a single pulse is also shown.

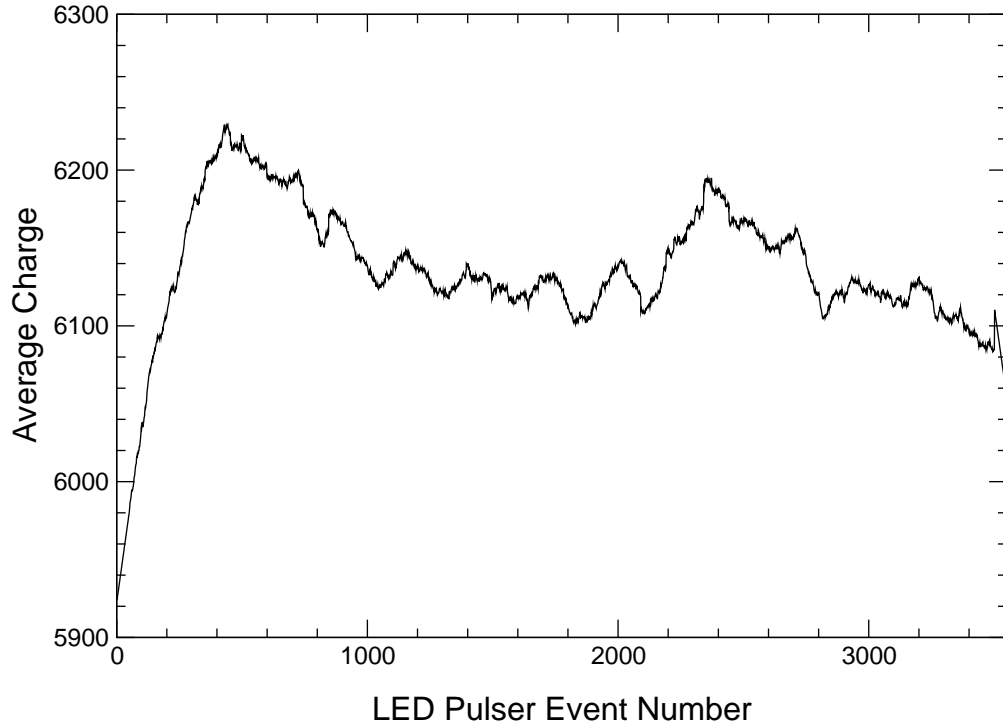


Figure 5.6: The average charges of the LED pulser events from the *gas in* run at $E_p=2.30$ MeV.

The First Pass

For each data run, the charges of the identified LED pulser events were recorded in consecutive order to a file. To reduce the spread in the results caused by the resolution of the system, an average charge was determined for each event by i) fitting the first and last fifty charges in each file by straight lines, and ii) smoothing the remaining charges using a 101-point average. The latter corresponds to an average over 5000 s. The average charges for the $E_p=2.30$ MeV ${}^3\text{He}$ *gas in* and *gas out* runs are shown in Figures 5.6 and 5.7, respectively, and are typical of those calculated from the other runs. The average charges are denoted by $\bar{p}(n)$ below, where n is the number of the event in the file.

Assuming a linear decrease in the LED light output with the number of pulses, and

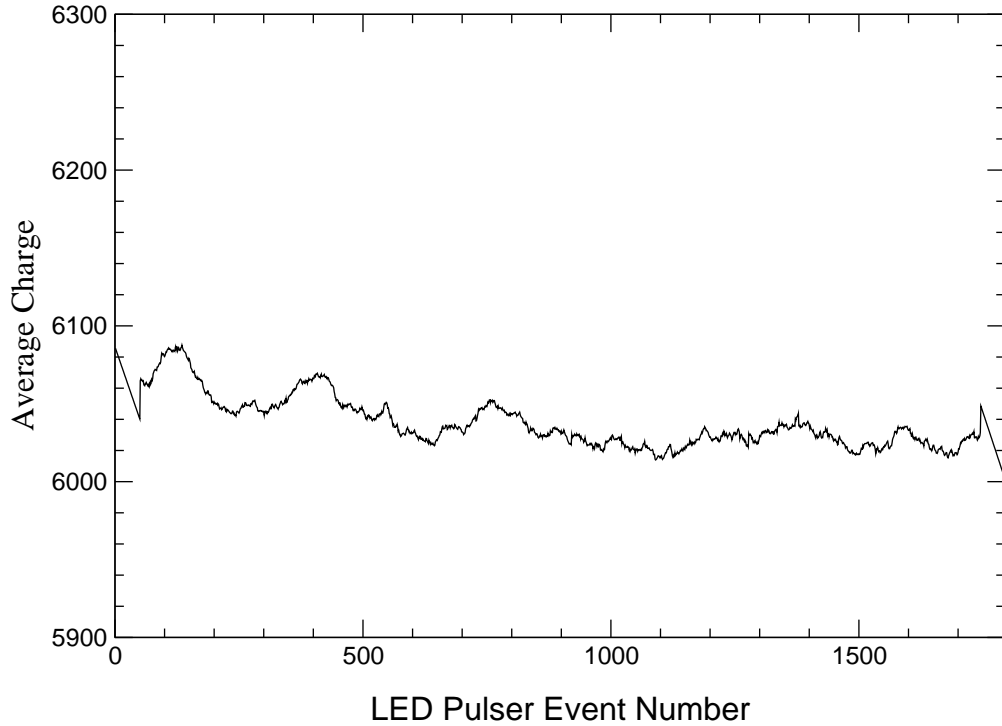


Figure 5.7: The average charges of the LED pulser events from the *gas out* run at $E_p=2.30$ MeV.

a constant gain in the electronics, the average charge of the n 'th LED pulser event is

$$p(n) = p_0(1 - an) \quad (5.4)$$

where p_0 is the average charge of the LED pulser event before the start of the measurement, and $p_0 a$ is the decrease in the average charge per pulse. The gain correction factor for the n 'th LED pulser event is given by the ratio of the expected and measured average charge $p(n)/\bar{p}(n)$. The gain correction factors for each run are also multiplied by a constant factor to produce the same overall gain in all of the runs.

The value of $p_0 a$ is chosen from the slope of the line that best fits the linear portions of $\bar{p}(n)$. It was assumed that $p_0 a$ is the same for the *gas in* and *gas out* data. From the positions of the peak in the ${}^7\text{Li}(p, \gamma_0){}^8\text{Be}(\text{g.s.})$ spectra taken before and after each run, and from the general behaviour of $\bar{p}(n)$ (see Figures 5.6 and 5.7), it was determined that the gain of the

system increased by 3–8% over the first six hours of the measurements, but was relatively stable during the *gas out* measurements 48 hours after the start of the experiments. Hence, the value of $p_0 a$ for each experiment was determined from the measurements of $\bar{p}(n)$ during the *gas out* run, and checked against the results from the *gas in* run.

In some cases, a sudden change in the average charge of the LED pulser events was observed that was inconsistent with a gain change in the system. Similar changes were commonly observed during the testing of the LED light pulser system at higher rates (~ 1 Hz). These were due to sudden changes in the LED light output. Sandorfi *et al.* [Sa84] also reported discontinuous changes in the LED light output of up to $\sim 20\%$ from a stabilized system that was used. Hence, in such cases, it is assumed that the changes in the average charges are due to sudden changes in the LED light output, and thus, a new value of p_0 is calculated for determining the expected charges $p(n)$ after such changes.

With the calculated values of $\bar{p}(n)$, p_0 and a , the gain correction factor for each LED pulser event was calculated and stored to a file. These factors were then used in the calculations of the corrected charges for all the pulses during the second pass of the analysis. Due to the uncertainty in the unstabilized LED light output, the gain correction factors are not exact. However, as will be shown below, the positions of the peaks in the gain corrected ${}^3\text{He}(n, \gamma)$ spectra as compared to the Monte Carlo simulated spectra indicate that the corrections are reasonably accurate.

The Second Pass

Using the acceptance cuts for the fits to scintillator pulses defined from the ${}^7\text{Li}(p, \gamma)$ events (cf. Section 5.3.1), and using the gain correction factors calculated over the first pass of the analysis, the pulses from the ${}^3\text{He}$ *gas in* and *gas out* runs were fitted and deconvoluted if necessary, and the corrected charges were sorted into energy spectra. The total spectra for

Table 5.3: Fractional Livetime For Each Run

E_p (MeV)	Run	#identified LED pulser events	#light pulser triggers	Fractional livetime
2.30	${}^3\text{He}(n, \gamma)$	3565	3578	0.9964 ± 0.0010
	Bkgd	1797	1806	0.9950 ± 0.0017
2.77	${}^3\text{He}(n, \gamma)$	3487	3492	0.9986 ± 0.0006
	Bkgd	1733	1736	0.9983 ± 0.0010
3.22	${}^3\text{He}(n, \gamma)$	3535	3542	0.9980 ± 0.0007
	Bkgd	1736	1739	0.9983 ± 0.0010
3.68	${}^3\text{He}(n, \gamma)$	3481	3487	0.9983 ± 0.0007
	Bkgd	1776	1779	0.9983 ± 0.0010
1.93	${}^3\text{He}(n, \gamma)$	3700	3705	0.9987 ± 0.0006
	Bkgd	1783	1785	0.9989 ± 0.0008

each experiment are shown in Figure 5.8. For comparison, the *gas out* spectra are scaled in each case by the ratio of the number of neutrons produced in the *gas in* run to the number produced during the *gas out* run, as given in Table 5.2. Deadtime corrections (on the order of $\sim 0.2\%$) have not been applied. LED pulser events are not included in the spectra.

The fractional livetime is given by the ratio of the number of identified LED pulser events to the number of times the light pulser circuit was triggered, and is shown in Table 5.3 for each run.

5.3.3 Cosmic Ray Spectrum

The cosmic ray data was processed in a similar manner to the *gas in* and *gas out* data as described above, except that an energy calibration for the system was only available at the start of the measurement. Figure 5.9 shows the average charges $\bar{p}(n)$ of the LED pulser events collected over a period of 118.75 hours, and shows that the gain varied considerably over the measurement. These variations are probably due to changes in the temperature of the target room over the measurement period. No definite linear region of $\bar{p}(n)$ is seen in Figure 5.9 for determining the value of $p_0 a$. Hence, the LED light output is assumed to decay at the same rate as in the following run at $E_p = 1.93$ MeV. Figure 5.10 shows the gain

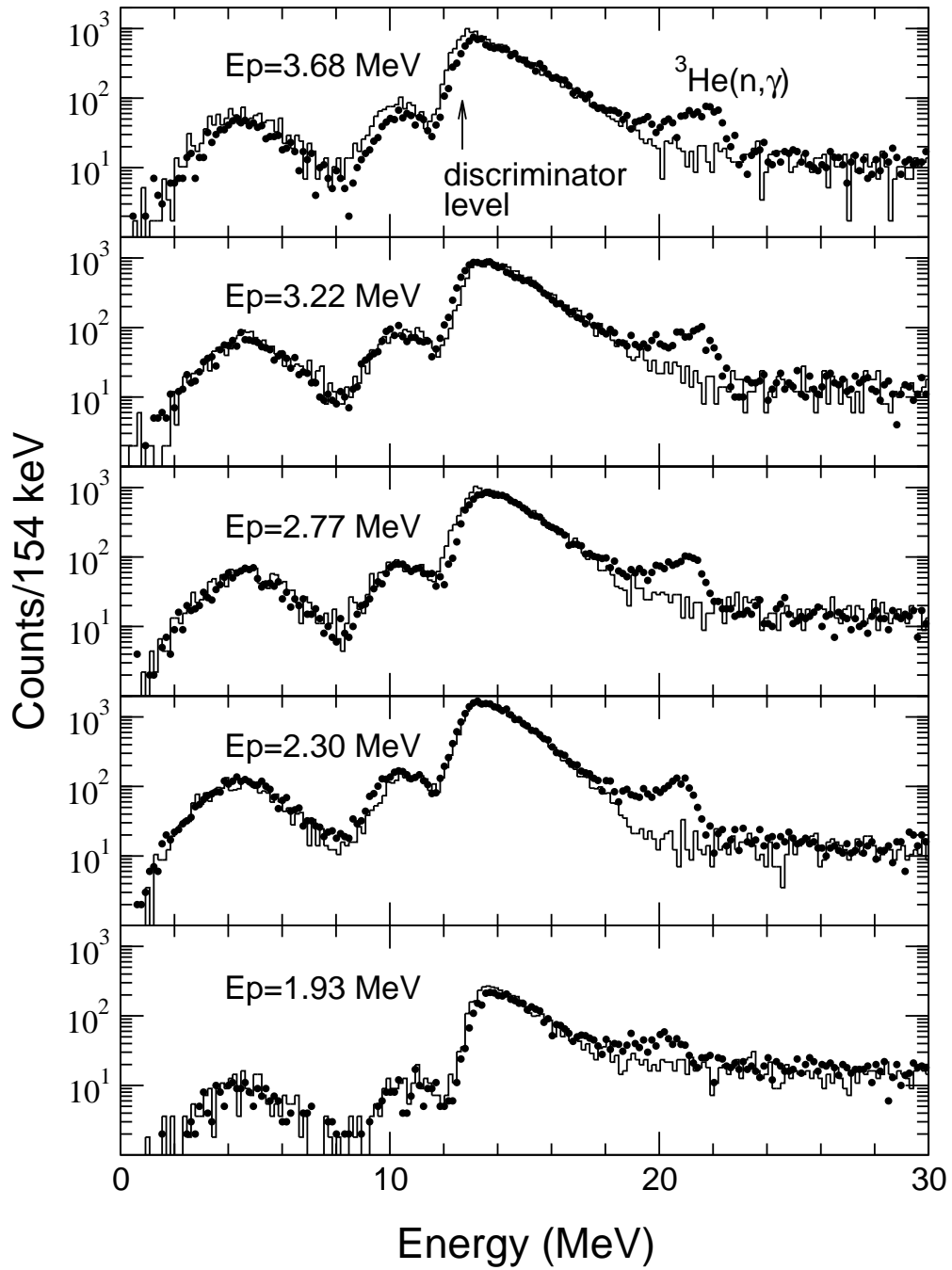


Figure 5.8: The gain corrected energy spectrum for each run, squashed to 256 channels. The solid points represent the *gas in* data, and the *gas out* spectra are shown as lines. The *gas out* spectra have been re-scaled, as explained in the text. The discriminator level was at ~ 13 MeV during the experiments, and counts below this energy are due to deconvoluted pile-up events.

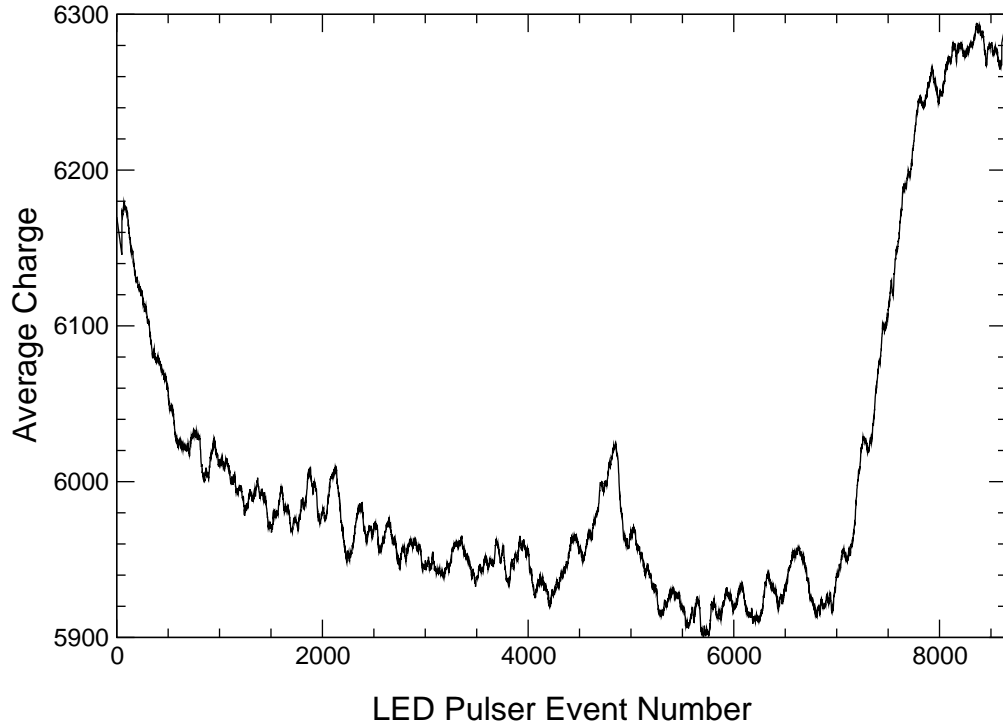


Figure 5.9: The average charges of the LED pulser events from the cosmic ray measurement.

corrected cosmic ray energy spectrum over the region of interest, along with the results of a fit to the data of the form

$$f_{CR}(x) = a_1 e^{-\frac{1}{2} \left(\frac{x-a_2}{a_3} \right)^2} + a_4 \quad (5.5)$$

The fit is used in subtracting the cosmic ray component from the ${}^3\text{He}(n, \gamma)$ and background spectra (see Section 5.5).

Although the use of the LED pulses for gain corrections may not be correct, a small shift in the gain will not significantly alter the shape of the spectrum. The cosmic ray background subtraction depends only on the shape of the spectrum in Figure 5.10, and thus, is insensitive to small errors in the gain correction.

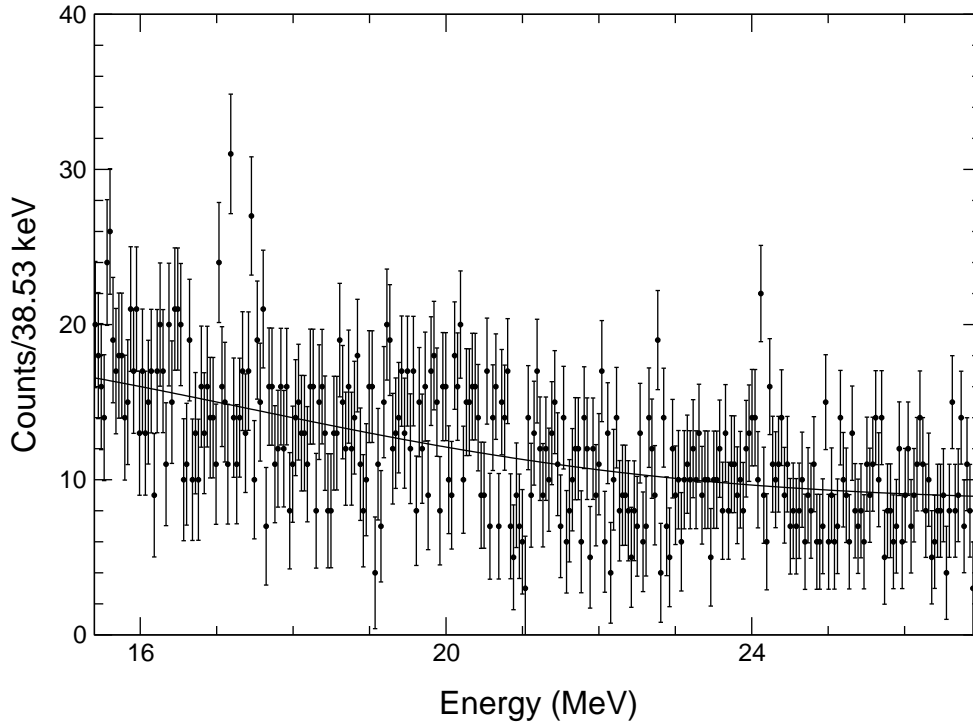


Figure 5.10: The energy spectrum for cosmic ray events over the region of interest, along with the results of a fit with eqn.(5.6).

5.4 Monte Carlo Simulations

The thicknesses of the gold and lithium layers given in Table 5.1 were used to calculate the proton energy spread through the targets for the Monte Carlo simulations. The simulations were run until there were $\sim 50 \times 10^3$ events in which ≥ 0.6 MeV was deposited in the BGO crystal. Figure 5.11 shows the calculated energy distributions of the neutrons from the ${}^7\text{Li}(p, n_0){}^7\text{Be}(\text{g.s.})$ reactions that produced gamma rays via the ${}^3\text{He}(n, \gamma)$ reaction. The angular distribution of the gamma rays aimed at the BGO crystal that generated counts in the region of interest above 15.4 MeV was also calculated in each case. Figure 5.12 shows the results from the $E_p=2.30$ MeV calculation, and is typical of the results from the other calculations. The distributions are slightly skewed to angles below 90° ($\bar{\theta} = 84.5^\circ$) due to the flux of neutrons being greatest in the part of the ${}^3\text{He}$ counter closest to the

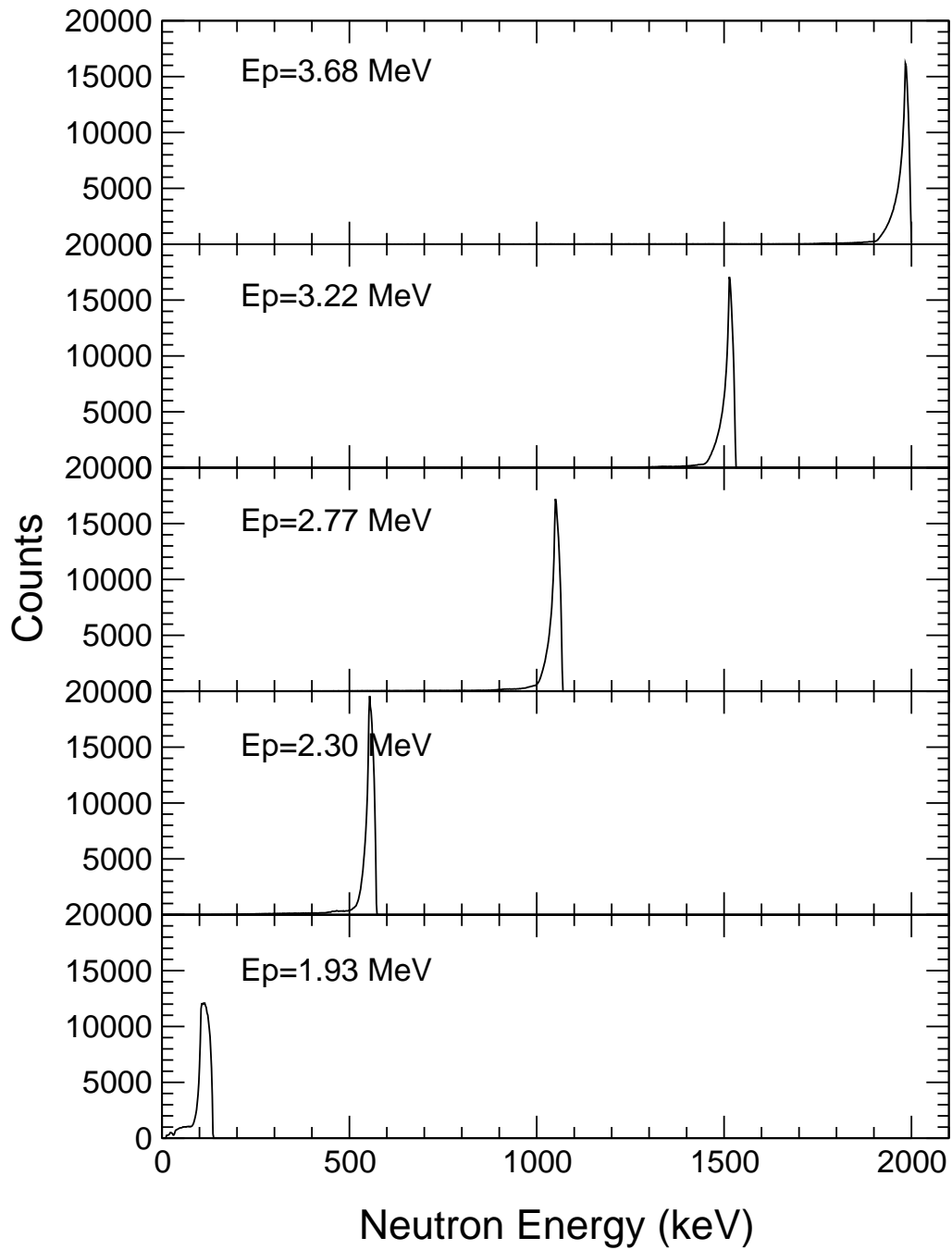


Figure 5.11: The Monte Carlo simulated energy spectra for the neutrons from the ${}^7\text{Li}(p, n){}^7\text{Be}(\text{g.s.})$ reactions that are captured via the ${}^3\text{He}(n, \gamma)$ reaction.

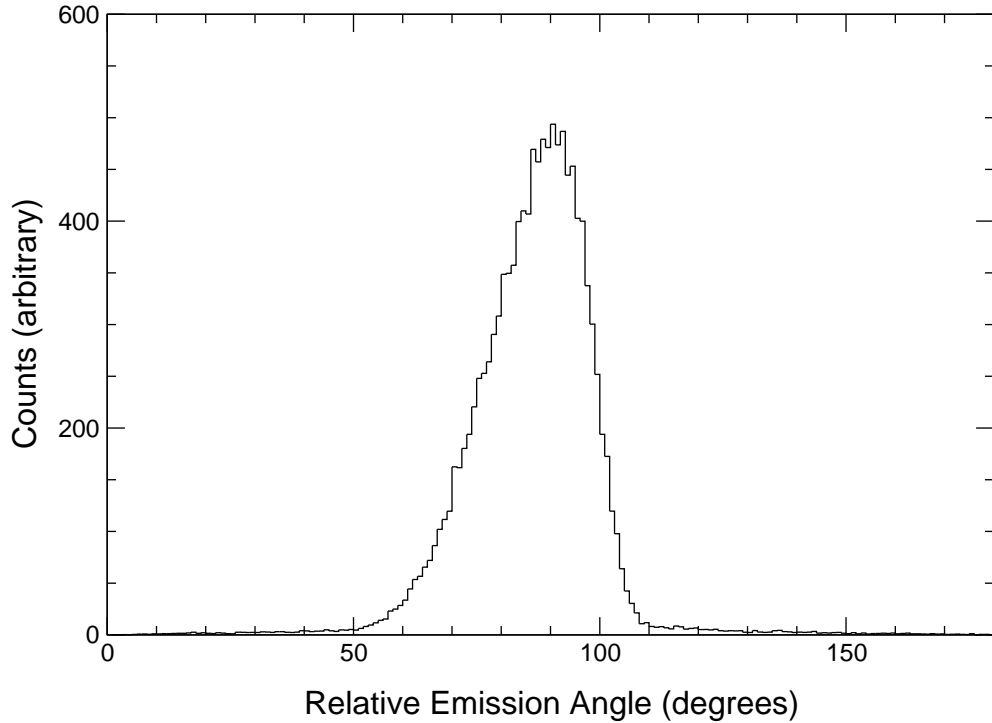


Figure 5.12: The calculated angular distribution of the gamma rays aimed at the BGO crystal that produced counts above 15.4 MeV, from the $E_p=2.30$ MeV calculation.

neutron source. The total energy deposited in the BGO crystal over each event was used to increment spectra with the same energy calibration as the experimental results. These spectra were subsequently smeared using a gaussian distribution with a standard deviation of $\sigma = 2.022E^{0.5155}$ (σ and E in keV) to match the resolution of the experimental data. Figure 5.13 shows the spectrum for the $E_p=2.30$ MeV calculation, and is typical of the results generated in the other calculations.

The neutron tracking part of the simulations indicates that the fraction of neutrons shot in the direction of the ^3He counter that interact between the neutron production target and the gas target ranges from 52% for the $E_p=1.93$ MeV run to 27% for the $E_p=3.68$ MeV run. However, some of the neutrons that interact in the target arrangement are forward scattered into the ^3He gas, and produce gamma rays through the $^3\text{He}(n, \gamma)$ reaction. Including the contribution of neutrons that scatter back into the gas off the walls of the

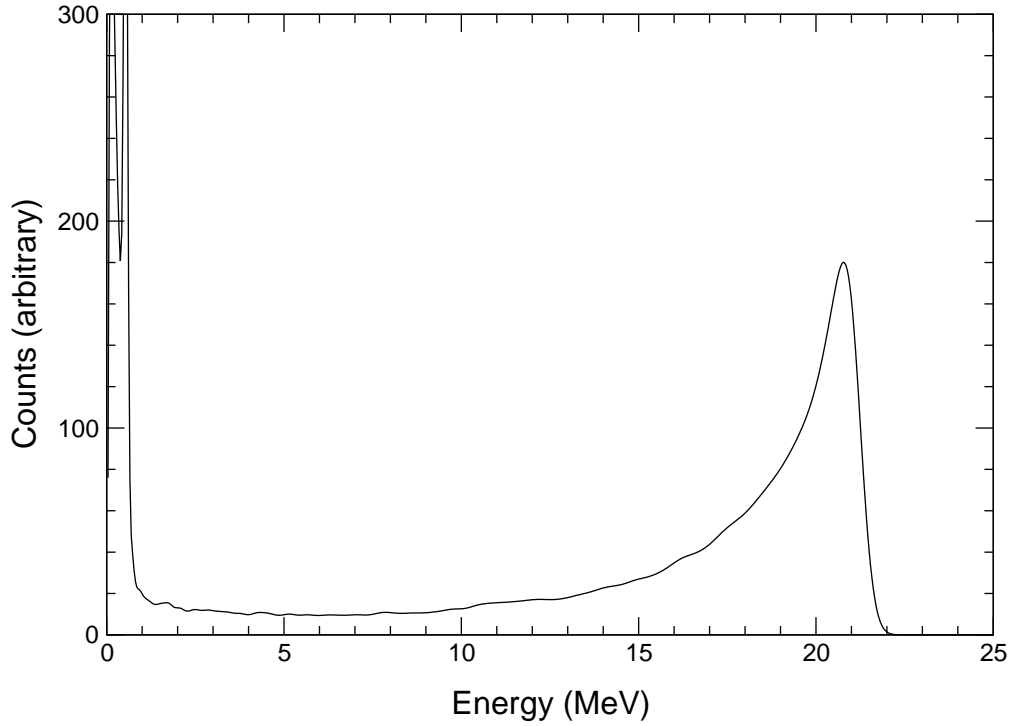


Figure 5.13: The Monte Carlo simulated energy spectrum for the ${}^3\text{He}(n, \gamma)$ reaction at $E_p=2.30$ MeV. The peak at 0.511 MeV is due to the pair production events outside of the BGO crystal.

counter, the fraction of gamma rays produced by scattered neutrons ranges from 26% for the $E_p=1.93$ MeV run to 12% for the $E_p=3.68$ MeV run.

The gamma ray tracking part of the simulation indicates that about 52% of the gamma rays aimed at the BGO crystal enter the detector without interacting in the shielding materials in between. Of these, about 70% deposit at least 15.4 MeV of energy in the crystal. Another $\sim 8\%$ of the gamma rays initially aimed at the BGO crystal are scattered into the detector, and $\sim 12\%$ of these deposit at least 15.4 MeV of energy. Hence, $\sim 37\%$ of the gamma rays aimed at the crystal produce counts in the region of interest of the spectrum. Gamma rays that were not initially aimed at the BGO crystal but scattered into the detector account for less than 0.34% of the total number of counts in the region of interest. Hence, these gamma rays were ignored in the calculations of the angular distributions and effective

solid angles of the BGO crystal.

5.5 Extracting the ${}^3\text{He}(n, \gamma)$ Cross Section

With the measured *gas in*, *gas out* and cosmic ray energy spectra, the calculated response of the spectrometer, and the results of the target activity measurements, the absolute cross section for the ${}^3\text{He}(n, \gamma)$ reaction was determined as described below. The analyses of the spectra were confined to a region above 15.4 MeV to avoid the effects of the discriminator on the shape of the spectra near the low-energy cut-off, and to a region below 27.0 MeV to avoid similar cut-off effects for pulses near the maximum amplitude that could be digitized.

The first step in the extraction of the cross sections was to correct the spectra for deadtime losses by dividing the number of counts in each channel by the appropriate fractional livetime given in Table 5.3.

The second step was the subtraction of the cosmic ray background from the *gas in* and *gas out* spectra. This was done by subtracting from each spectrum the cosmic ray component given by eqn.(5.6), scaled to match the high-energy region of the spectrum above the counts produced by ${}^3\text{He}(n, \gamma)$, ${}^7\text{Li}(p, \gamma)$ and pile-up events.

The third step was to subtract the contribution to the measured ${}^3\text{He}(n, \gamma)$ gamma ray spectrum due to the neutrons from the ${}^7\text{Li}(p, n_1){}^7\text{Be}(0.43 \text{ MeV})$ reaction. This applied to the data at $E_p = 2.77, 3.22$ and 3.68 MeV . To calculate the contribution in each case, a Monte Carlo simulation was done for the response of the spectrometer to ${}^3\text{He}(n, \gamma)$ gamma rays produced by the same number of neutrons from the ${}^7\text{Li}(p, n_1){}^7\text{Be}(0.43 \text{ MeV})$ reaction as was produced in the experiment. Except for the kinematics of the production of the neutrons, the simulations were identical to those done for the neutrons from the ${}^7\text{Li}(p, n_0){}^7\text{Be}(\text{g.s.})$ reaction. The absolute cross section for the ${}^3\text{He}(n, \gamma)$ reaction used in the calculations

was that given by eqn.(4.1), with $\sigma_0 = 1 \mu\text{b}$ in each case. Table 5.1 shows the calculated maximum energies of the two neutron groups for each measurement. The proton energies were chosen so that the energy of the n_1 group in any measurement was close to the energy of the n_0 group in the previous measurement. Hence, the contribution subtracted from the measured ${}^3\text{He}(n, \gamma)$ spectra was that calculated with the Monte Carlo simulation, but scaled by the cross section extracted for the n_0 group from the previous measurement.

The number of n_1 group neutrons produced in any measurement was calculated by multiplying the total number of neutrons by the fraction that were n_1 group neutrons. The total number was deduced from the activity measurements (cf. Table 5.2), and the fraction was calculated using the ${}^7\text{Li}(p, n)$ cross sections of [Li75].

The corrected *gas out* spectra only contain counts due to gamma rays from the ${}^7\text{Li}(p, \gamma)$ reaction that leak through the shadowbar, and the unresolved pile-up of gamma rays from (n, γ) reactions within the spectrometer. These spectra were fitted over the region of interest using a function of the form

$$f_{bkgd}(x) = a_1 e^{-\frac{1}{2} \left(\frac{x-a_2}{a_3} \right)^2} + a_4 + a_5 x + a_6 x^2 \quad (5.6)$$

The spectra and the results of the fits are shown in Figure 5.14. To determine the number of counts N_{ROI} in the region of interest above 15.4 MeV produced by gamma rays from the ${}^3\text{He}(n, \gamma)$ reaction, the fit to the corrected *gas out* spectrum and the Monte Carlo generated spectrum were scaled and summed to match the corrected *gas in* spectrum, using a least-squares fitting procedure. The results of the fit at each energy are shown in Figure 5.15. The agreement between the positions of the peak in the *gas in* and Monte Carlo generated spectra indicate that the gain correction factors calculated during the digital pulse processing were reasonably accurate. The area under the scaled Monte Carlo spectrum in the region of interest (N_{ROI}) is shown in Table 5.4 for each data run. From the scaling factor

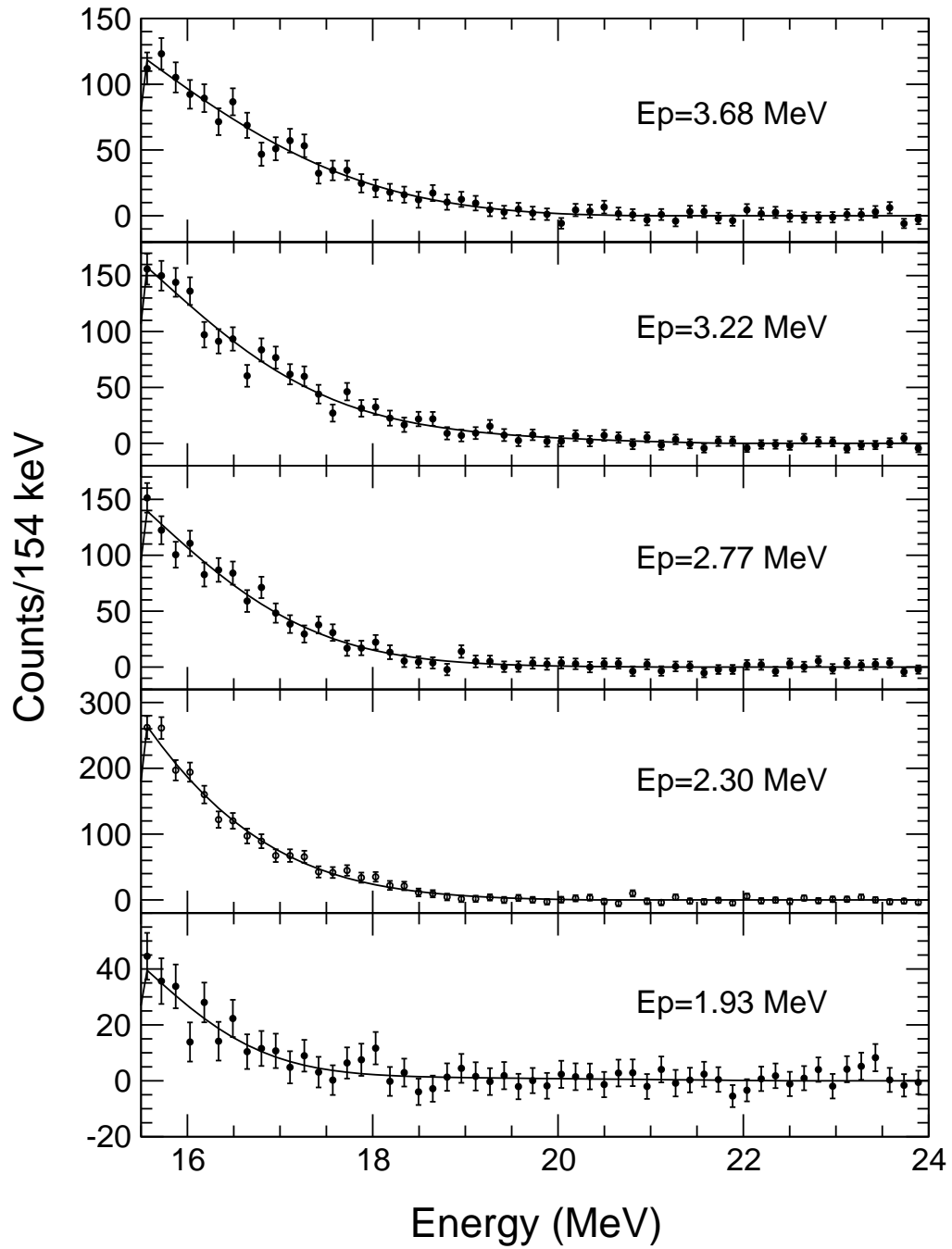


Figure 5.14: The deadtime corrected and cosmic ray subtracted *gas out* spectra, along with the results of fits to eqn.(5.7). The spectra and the results of the fits have been squashed into 256 channel spectra for clarity. The solid points are the *gas out* data, and the results of the fits are shown as lines.

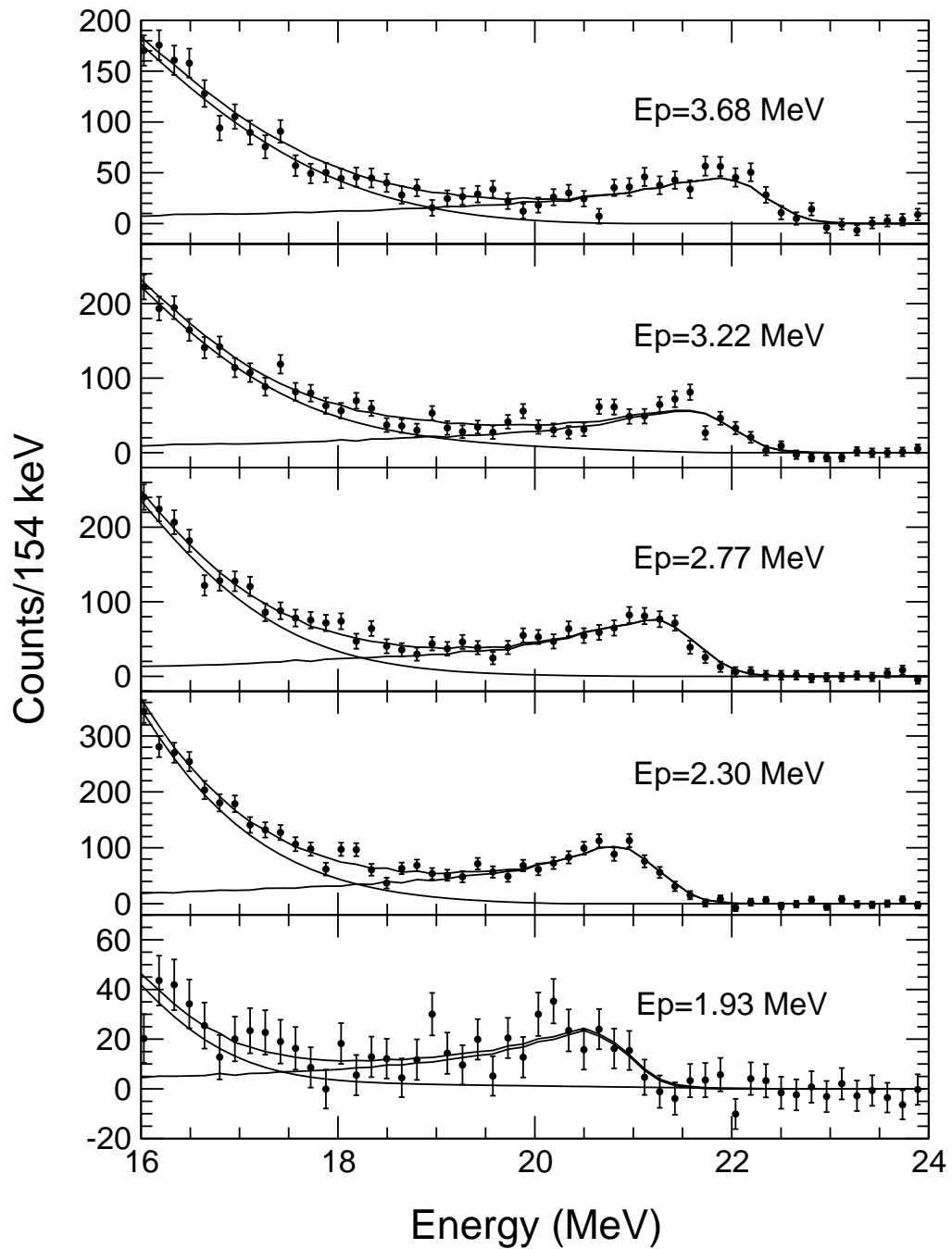


Figure 5.15: The corrected *gas in* spectra along with the results of the fitting procedure, squashed into 256 channel spectra for clarity. The solid points are the *gas in* data; the fitted *gas out* data, fitted Monte Carlo response, and sum of the fits are shown as lines in each case.

Table 5.4: Gamma Ray Production and Detection

E_p (MeV)	N_{ROI}	N_γ
1.93	$389 \pm 46(\text{stat})$	$1089 \pm 130(\text{stat}) \pm 15(\text{syst})$
2.30	$1784 \pm 66(\text{stat})$	$4872 \pm 180(\text{stat}) \pm 68(\text{syst})$
2.77	$1417 \pm 61(\text{stat})$	$3813 \pm 160(\text{stat}) \pm 53(\text{syst})$
3.22	$1137 \pm 60(\text{stat})$	$3041 \pm 160(\text{stat}) \pm 43(\text{syst})$
3.68	$928 \pm 54(\text{stat})$	$2461 \pm 140(\text{stat}) \pm 34(\text{syst})$

C_{MC} for the Monte Carlo generated spectrum, and the number of gamma rays $(N_\gamma)_{MC}$ aimed at the crystal in the simulation, the number of gamma rays N_γ aimed at the crystal during each experiment is given by

$$N_\gamma = C_{MC} (N_\gamma)_{MC} (0.968 \pm 0.014) \quad (5.7)$$

where the last factor corrects for the over-attenuation of the gamma rays through the shielding materials in the calculations (see page 78). The results for N_γ are also shown in Table 5.4. As noted on page 100, the number of counts in the region of interest is related to the number of gamma rays aimed at the BGO crystal by $N_{ROI} \simeq 0.37N_\gamma$.

The number of gamma rays produced in the ^3He counter that are aimed toward the BGO crystal is also given by

$$N_\gamma = N_n n_{He} t \frac{d\sigma}{d\Omega} \Delta\Omega \quad (5.8)$$

where N_n is the number of neutrons that passed through the ^3He counter, n_{He} is the atomic density of the ^3He gas (4.535×10^{20} atoms/cm³), t is the effective target thickness (cm), $\Delta\Omega$ is the effective solid angle subtended by the BGO crystal, and $d\sigma/d\Omega$ is the differential cross section for the $^3\text{He}(n, \gamma)$ reaction averaged over the neutron energies and $\Delta\Omega$. The total number of neutron histories started was recorded after each calculation, along with the number of neutrons that entered the ^3He counter. By scaling these results to the number of neutrons produced in each experiment as calculated from the activation measurements

(cf. Table 5.2), the number of neutrons N_n that entered the target was determined for each data run. The effective solid angle $\Delta\Omega$ was calculated from the ratio of the number of gamma rays aimed at the BGO crystal to the total number produced in the simulation. The effective target thickness and the differential cross section averaged over the neutron energies is given by

$$t \frac{d\sigma}{d\Omega} = L \frac{d\sigma}{d\Omega}(E_0) \overline{\langle f_\sigma(E_n) (l/L) \rangle} \quad (5.9)$$

where L is the maximum possible pathlength through the ^3He gas (25.90 cm), E_0 is the maximum neutron energy for the run, l is the pathlength seen by each neutron entering the ^3He counter, and $f_\sigma(E_n)$ is the ratio of the $^3\text{He}(n, \gamma)$ cross sections at E_n and E_0 . The product of f_σ and (l/L) is the weighting factor on each gamma ray (see page 60), hence, $\overline{\langle f_\sigma(E_n) (l/L) \rangle}$ is given by the average value of the weighting factors on the gamma rays produced in the $^3\text{He}(n, \gamma)$ reaction.

From eqn.5.8 and 5.9, the measured differential cross section averaged over $\Delta\Omega$ is

$$\frac{d\sigma}{d\Omega}(E_0) = \frac{N_\gamma}{N_n n_{He} L \Delta\Omega \overline{\langle f_\sigma(E_n) (l/L) \rangle}} \quad (5.10)$$

If the angular distribution for the $^3\text{He}(n, \gamma)$ reaction was isotropic as assumed in the Monte Carlo simulation, then the result from eqn.5.10 would be equivalent to $d\sigma/d\Omega(E_0, 90^\circ)$. However, if the gamma rays are emitted over a dipole distribution ($W(\theta) \sim \sin^2 \theta$), as indicated by previous experiments [Al80, We82], then the differential cross section at 90° is obtained from eqn.5.10 by correcting for the reduced cross section seen at other angles. Thus, $d\sigma/d\Omega(E_0, 90^\circ) = C_{W(\theta)} d\sigma/d\Omega(E_0)$, where the correction factor $C_{W(\theta)}$ is

$$C_{W(\theta)} = \frac{\int_0^\pi g(\theta) d\theta}{\int_0^\pi \sin^2 \theta g(\theta) d\theta} \quad (5.11)$$

and $g(\theta)d\theta$ is the distribution of angles calculated by the Monte Carlo simulation (see, for example, Figure 5.12). The quantities necessary for computing $d\sigma/d\Omega(E_0, 90^\circ)$ are shown

Table 5.5: Quantities for Computing the Differential Cross Sections

E_p (MeV)	N_n	$\Delta\Omega$ (sr)	$\langle f_\sigma(l/L) \rangle$	$C_{w(\theta)}$
1.93	$(7.58 \pm 0.07(\text{stat}) \pm 0.39(\text{syst})) \times 10^{12}$	0.03423	0.16423	1.0525
2.30	$(1.72 \pm 0.02(\text{stat}) \pm 0.09(\text{syst})) \times 10^{13}$	0.03416	0.18557	1.0501
2.77	$(7.84 \pm 0.11(\text{stat}) \pm 0.97(\text{syst})) \times 10^{12}$	0.03432	0.18672	1.0486
3.22	$(5.63 \pm 0.05(\text{stat}) \pm 0.29(\text{syst})) \times 10^{12}$	0.03449	0.18524	1.0464
3.68	$(3.80 \pm 0.04(\text{stat}) \pm 0.20(\text{syst})) \times 10^{12}$	0.03449	0.18578	1.0449

The uncertainties on $\Delta\Omega$, $\langle f_\sigma(l/L) \rangle$ and $C_{w(\theta)}$ are insignificant in comparison to the other uncertainties, and are ignored.

 Table 5.6: The Differential and Absolute Cross Sections for the ${}^3\text{He}(n, \gamma)$ Reaction

E_p (MeV)	E_0 (MeV)	$\frac{d\sigma}{d\Omega}(E_0, 90^\circ)$ ($\mu\text{b}/\text{sr}$)	$\sigma_{n,\gamma}(E_0)$ (μb)
1.93	0.135	$2.29 \pm 0.05(\text{stat}) \pm 0.12(\text{syst})$	$19.2 \pm 2.3(\text{stat}) \pm 1.0(\text{syst})$
2.30	0.571	$4.00 \pm 0.15(\text{stat}) \pm 0.22(\text{syst})$	$33.5 \pm 1.3(\text{stat}) \pm 1.8(\text{syst})$
2.77	1.068	$6.77 \pm 0.30(\text{stat}) \pm 0.84(\text{syst})$	$56.7 \pm 2.6(\text{stat}) \pm 7.1(\text{syst})$
3.22	1.530	$7.54 \pm 0.40(\text{stat}) \pm 0.41(\text{syst})$	$63.1 \pm 3.4(\text{stat}) \pm 3.4(\text{syst})$
3.68	1.999	$8.99 \pm 0.53(\text{stat}) \pm 0.49(\text{syst})$	$75.3 \pm 4.4(\text{stat}) \pm 4.1(\text{syst})$

in Table 5.5, and the results for the differential cross sections are shown in Table 5.6. The statistical uncertainty ($\pm 1 \sigma$) was calculated in the steps outlined in this chapter, while the calculation of the systematic uncertainty in the Monte Carlo simulations is outlined in Section 4.3.

Assuming that the gamma rays are emitted over a dipole angular distribution, the total cross section for the ${}^3\text{He}(n, \gamma)$ reaction is given by $\sigma_{n,\gamma}(E_0) = (8\pi/3) d\sigma/d\Omega(E_0, 90^\circ)$, and is shown in Table 5.6 for each energy. The results are discussed in the next chapter.

Chapter 6

Conclusions

The absolute cross section of the ${}^3\text{He}(n, \gamma)$ reaction was measured at five energies between $E_n=0.14\text{--}2.0$ MeV. The ~ 21 MeV gamma rays were detected at 90° with respect to the beam direction using a spectrometer housing a $127\text{ mm} \times 76\text{ mm}$ BGO crystal. In the present experiment, neutron backgrounds are severe and good timing is not required. Hence, the BGO crystal was chosen over the more usual choice of NaI crystal. A spectrometer with a BGO detector can have the same absolute efficiency for the detection of medium energy gamma rays as a larger spectrometer housing a NaI detector, as well as a comparable energy resolution. The backgrounds are expected to be lower in the BGO detector, which makes up for the poorer resolving time for pile-up detection due to the slower photomultiplier tube. The energy resolution of the system was 8.0% at $E_\gamma=21$ MeV, which is adequate for the present experiment. The active shield surrounding the BGO detector suppressed cosmic ray muon events with an efficiency $\geq 99\%$. In order to reduce the random blocking of valid events, the active shield was designed so that gamma rays, neutrons and escaping radiation from the crystal would not be likely to trigger the production of blocking pulses. As a result of this, the system deadtime during the measurements was $\leq 0.5\%$. The background rate above ~ 1 MeV during the measurements was between $10\text{--}20$ kcps, and was due mostly to neutron capture gamma rays. By clipping the pulses from the detector to ~ 350 ns,

the fraction of counts above 13 MeV due to pile-up was kept below 10%. A conventional pile-up rejection circuit was found to be inadequate for eliminating pulses with pile-up, due to the small amount of light emitted by the BGO crystal. For good energy resolution, an efficient photomultiplier tube with a long risetime is required to detect the light output of the crystal. The long risetime results in a pile-up resolving time of only ~ 120 ns. Also, the relatively large shot noise on the clipped pulses causes the spurious rejection of higher energy events. Hence, instead of using conventional electronics, the pulses from the BGO detector were digitized and processed off-line on a computer. The pulse fitting algorithm used in the present experiment results in a pile-up resolving time of ~ 50 ns, which is an improvement over the expected resolving time of ~ 140 ns for the peak detection method used by [Ch86, Dr89]. The present algorithm also allows gain corrections to be made on the data. These improvements, however, come at the expense of greater complexity, more personal attention during the pulse correction and deconvolution stage, and longer computation times. The fitting routine processes pulses at a rate of ~ 7 events/s on a SUN 4/110 computer. Hence, it is unlikely that such an algorithm could be used in a real-time system.

The response function of the spectrometer was calculated using a Monte Carlo simulation. The photon, electron and positron tracking parts of the program were tested using the 992 keV resonance of the $^{27}\text{Al}(p, \gamma)^{28}\text{Si}$ reaction, and the 441 keV resonance of the $^7\text{Li}(p, \gamma)^8\text{Be}$ reaction. The calculated and experimental results were in agreement in both cases. In the latter case, the value of $\sigma_R = 6.0$ mb recommended by [Aj88] was replaced with the value $\sigma_R = 4.83$ mb, which was calculated from the thick target yield result of [Fo49] using modern values of the resonance width and the proton stopping power. Due to the poor resolution of the ^3He proportional counter used in the experiment, the neutron

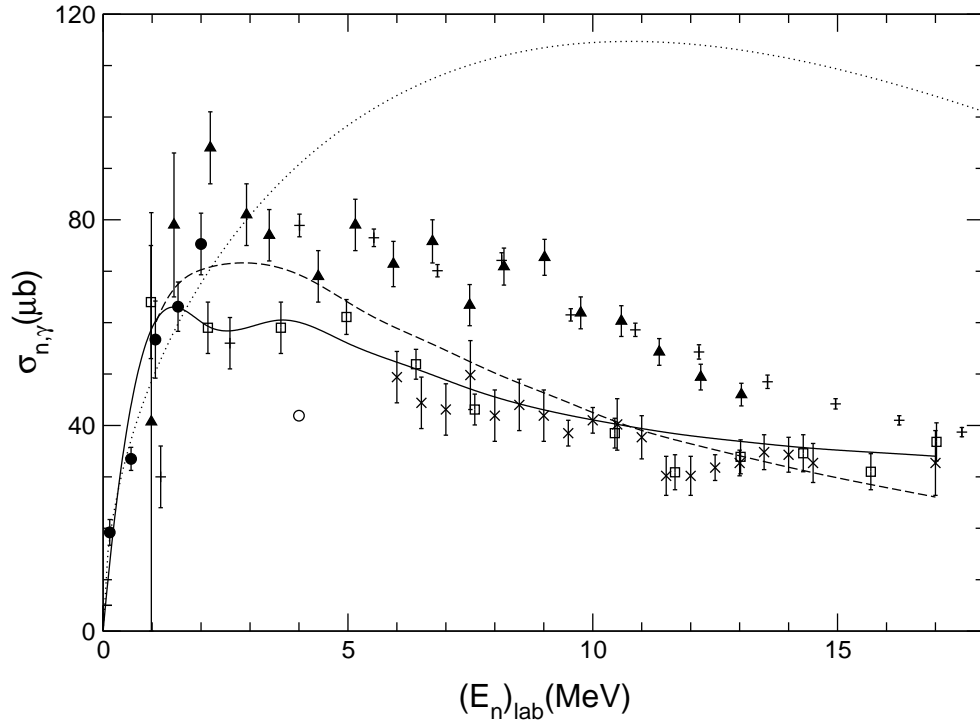


Figure 6.1: Measured and calculated values of the cross section for the ${}^3\text{He}(n,\gamma)$ reaction. The symbols are defined as follows: (n,γ) : \bullet the present work; \times [Wa81]; \circ [Zu63] (uncertainty unknown); (γ,n) : \square [Be80]; \triangle [Ir75]; $+$ [Na91]; --- [Ca83a]; --- [Un90] (normalized to the three highest energy points from the present work); $\text{-}\cdot\text{-}\cdot\text{-}$ eqn.4.1 [Fl51] (fitted to the results of the present work).

tracking part of the program was not verified experimentally. However, due to the small amount of material between the neutron source and the ${}^3\text{He}$ gas, the estimated uncertainty in the neutron flux calculations is only $\sim \pm 5\%$.

The results of the present measurement of $\sigma_{n,\gamma}$ as given in Table 5.4 are shown in Figure 6.1, along with the (n,γ) results of [Zu63, Wa81] and the converted (γ,n) results of [Ir75, Be80, Na91]. Also shown in the figure are the results of a fit to the present data with eqn.4.1 [Fl51] ($\text{-}\cdot\text{-}\cdot\text{-}$), the converted (γ,n) cross section recommended by Calarco *et al.* [Ca83a] (---), and the results of a refined resonating group model calculation [Un90] (---) normalized to the three highest energy points from the present work.

The energy dependence of the present results is described reasonably well by eqn.4.1

(ie. $\sigma_{n,\gamma} = C\sqrt{E}(20.58 + \frac{3}{4}E)^3 e^{-3E/4\varepsilon}$; $\varepsilon = 6\text{MeV}$) (see Figure 6.1). The fit to the present data yields a reduced chi-square of $\chi_R^2=1.46$. Thus, it was an acceptable approximation to use eqn.4.1 for calculating the energy dependence of the cross section during the Monte Carlo simulations (cf. Section 4.1.1). At higher energies, however, the cross section calculated from the fit clearly deviates from all of the measurements. The expression for $\sigma_{n,\gamma}$ was derived using Gaussian-type wave functions and neglecting non-central forces (ie. all particles in the ground states of the nuclei are assumed to be in the $0s_{1/2}$ shell). The value of 6 MeV for the natural unit of energy $\varepsilon=\alpha^2\hbar^2/2M$ corresponds to an oscillator size parameter for the Gaussian-type wave functions of $\alpha^{-1}=1.9$ fm. This is slightly larger than the value of $\alpha^{-1}=1.67$ fm used successfully by Reichstein *et al.* [Re71] for resonating group model calculations of some $A=4$ systems. A better fit to the cross section over all energies is obtained if a value $\varepsilon\sim 3$ MeV is used, however, this corresponds to an unacceptably large value $\alpha^{-1}=2.6$ fm for the oscillator size parameter. Thus, the poor results at higher energies are probably due to neglecting non-central forces and expressing the ground states of the nuclei as pure $0s_{1/2}$ Gaussian-type wave functions. This is corroborated by the recoil corrected continuum shell model calculations of Halderson and Philpott [Ha79] that demonstrate the need to include 1p-1h correlations of the type $|0s_{1/2}^{-1} n s_{1/2}\rangle^{J=0}$ in the ground state of ${}^4\text{He}$.

Unfortunately, due to the poor quality of the (γ, n) data just above the threshold for the reaction, it is not possible to rule out any of the previous measurements based on the results of the present measurement alone. Also, the structure at low energies in the converted cross section recommended by Calarco *et al.* [Ca83a] is due to an unphysical choice for the energy dependence of $\sigma_{\gamma,n}$ near the threshold. Hence, for a more accurate comparison, it is necessary to extend the present results using a suitable theory to higher

energies ($E_n > 5$ MeV) where the other results are more dependable. Recently, Wachter *et al.* [Wa88] performed a refined resonating group model (RRGM) calculation of the two-body photodisintegration cross sections on ${}^4\text{He}$. The results of the calculations for $\sigma_{\gamma,p}$ agree with the values recommended by [Ca83a], and those for $\sigma_{\gamma,n}$ agree with the results of [Ir75, Na91]. Also, similar calculations of the ${}^4\text{He}(e, e'p)$ and ${}^4\text{He}(e, e'n)$ cross sections agree well with recent measurements from Mainz [Sp89]. However, it has been mentioned [Ti92] that there is some problem with the manner in which Siegert's Theorem has been applied in the calculations, which could have resulted in the cross section being too large. Also, there is an indication that the lack of two-particle correlations in the microscopic RRGm calculations results in an incorrect shape for the giant resonance peak. Sofianos *et al.* [So92] recently calculated the ${}^4\text{He}(\gamma, p)$ cross section using an integrodifferential equation approach (IDEA) and an optical model treatment of final state interactions. Their results are in good agreement with the recent experimental results of Feldman *et al.* [Fe90], reproducing the flattening of the giant dipole resonance seen in the experiment. It was reported that the results were sensitive to the choice of optical model parameters. When the calculations were performed using optical potential parameters calculated from fits to phase shifts from the RRGm calculations, a peaked giant resonance behaviour similar to that of the RRGm results was produced. This suggests that two-particle correlations must necessarily be included in the microscopic calculations to reproduce the flattened resonance behaviour. However, since no results for the ${}^4\text{He}(\gamma, n)$ cross section based on IDEA have been published as yet, the best theoretical results at present are probably still provided by the RRGm calculations. These results [Un90] were used to extend the results of the present measurements to higher energies, and are shown in Figure 6.1. The calculated results have been reduced by $\sim 33\%$ to match the three highest energy points from the present work (the calculations do not

extend to the two lower energy points). The extended results agree well with the results of [Be80, Wa81], and thus with the recommended cross section of [Ca83a], but not with the higher results of [Ir75, Na91]. It would also appear that a flattening of the cross section over the peak of $\sigma_{\gamma,n}$ (between $(E_n)_{lab}=5-20$ MeV) as suggested by the results of Sofianos *et al.* [So92] might result in a better match to the experimental results of [Be80, Wa81].

In summary, the absolute cross section of the ${}^3\text{He}(n, \gamma)$ reaction was measured between $E_n=0.14-2.0$ MeV to an accuracy of $\sim\pm 10\%$, which is suitable for the design optimization of the high energy gamma ray source. The cross section was extended to higher energies using the re-normalized RRGGM results, and was found to agree with the values recommended by Calarco *et al.* [Ca83a] over the region of the giant dipole resonance. Every reasonable theory and simultaneous measurement of the ratio of the $\sigma_{\gamma,p}/\sigma_{\gamma,n}$ has yielded a result close to unity. Thus, if the recommended values of [Ca83a] for $\sigma_{\gamma,n}$ are correct, then the results of [Be88, Fe90] for $\sigma_{\gamma,p}$ are probably correct as well. These results, however, are in disagreement with the recent results of the elastic photon scattering measurements by Wells *et al.* [We92], indicating that there could be some problems with the latter.

Bibliography

- [Aj88] F. Ajzenberg-Selove, Nucl. Phys. **A490** (1988) 1.
- [Al79] V.P. Alfimenkov, S.B. Borzakov, J. Wierzbicki, O.N. Ovchinnikov, L.B. Pikel'ner, and E.I. Sharapov, JETP Letters **29** (1979) 91.
- [Al80] V.P. Alfimenkov, S.B. Borzakov, G.G. Bunatyan, J. Wierzbicki, L.B. Pikel'ner, and E.I. Sharapov, Sov. J. Nucl. Phys. **31** (1980) 10.
- [Am69] G. Amsel, R. Bosshard, and C. Zajde, Nucl. Instr. and Meth. **71** (1969) 1.
- [An77] A. Anttila, J. Keinonen, M. Hautala, and I. Forsblom, Nucl. Instr. and Meth. **147** (1977) 501.
- [Ba57] F.C. Barker and A.K. Mann, Philos. Mag. (Ser. 8) **2** (1957) 5.
- [Ba84] F.C. Barker, Aust. J. Phys. **37** (1984) 583.
- [Be53] H.A. Bethe, Phys. Rev. **89** (1953) 1256.
- [Be63] M.J. Berger, in *Methods in Computational Physics*, Volume 1, ed. B. Alder, S. Fernbach and M. Rotenberg, (Academic Press, New York and London, 1963) 135.
- [Be69] P.R. Bevington, *Data Reduction and Error Analysis for the Physical Sciences*, (McGraw-Hill Book Company, New York, San Francisco, St. Louis, Toronto, London and Sydney, 1969) 235.
- [Be80] B.L. Berman, D.D. Faul, P. Meyer, and D.L. Olson, Phys. Rev. C **22** (1980) 2273.
- [Be88] R. Bernabei, A. Chisholm, S. d'Angelo, M.P. De Pascale, P. Picozza, C. Schaerf, P. Belli, L. Casano, A. Incicchitti, D. Prospero, and B. Girolami, Phys. Rev. C **38** (1988) 1990.
- [Be89] Scientific and Technical Description of the Mark II SNO Detector, eds. E.W. Beier and D. Sinclair, SNO-89-15 (1989).
- [Be90] J.R. Beene, F.E. Bertrand, D.J. Horen, R.L. Auble, B.L. Burks, J. Gomez del Campo, M.L. Halbert, R.O. Sayer, W. Mittag, Y. Schutz, J. Barrette, N. Alamanos, F. Auger, B. Fernandez, A. Gillibert, B. Haas, and J.P. Vivien, Phys. Rev. C **41** (1990) 920.
- [Bl68] S.L. Blatt, J. Mahieux, and D. Kohler, Nucl. Instr. and Meth. **60** (1968) 221.

- [Bl86] C.L. Blilie, D. Dehnhard, D.B. Holtkamp, S.J. Seestrom- Morris, S.K. Nanda, W.B. Cottingham, D. Halderson, C.L. Morris, C.Fred Moore, P.A. Seidl, H. Ohnuma, and K Maeda, *Phys. Rev. Lett.* **57** (1986) 543.
- [Bo82] R. Böttger, H. Klein, A. Chalupka, and B. Strohmaier, in *Nuclear Data for Science and Technology; Proceedings of the International Conference, Antwerp 1982*, ed. K.H. Böckhoff, (D. Reidel Publishing Company, Dordrecht, Boston and London, 1983) 484.
- [Bo88] G.O. Bolme, L.S. Cardman, R. Doerfler, L.J. Koester, Jr., B.L. Miller, C.N. Papanicolas, H. Rothhaas, and S.E. Williamson, *Phys. Rev. Lett.* **61** (1988) 1081.
- [Br72] K.W. Broda and W.R. Johnson, *Phys. Rev. A* **6** (1972) 1693.
- [Bu60] J.C. Butcher and H. Messel, *Nucl. Phys.* **20** (1960) 15.
- [Ca83a] J.R. Calarco, B.L. Berman, and T.W. Donnelly, *Phys. Rev. C* **27** (1983) 1866.
- [Ca83b] J.R. Calarco, S.S. Hanna, C.C. Chang, E.M. Diener, E. Kuhlmann, and G.A. Fisher, *Phys. Rev. C* **28** (1983) 483.
- [Ch86] R.E. Chrien and R.J. Sutter, *Nucl. Intsr. and Meth.* **A249** (1986) 421.
- [Ch89] R. Cherubini, G. Moschini, R. Nino, R. Policroniades, and A. Varela, *Nucl. Instr. and Meth.* **A281** (1989) 349.
- [Cl69] G.J. Clark, P.B. Treacy, and S.N. Tucker, *Aust. J. Phys.* **22** (1969) 663.
- [Co90] P. Corvisiero, M. Anghinolfi, L.Z. Dzhilavyan, G. Gervino, L. Grosso, G. Ricco, M. Sanzone, M. Taiuti, and A. Zucchiatti, *Nucl. Instr. and Meth.* **A294** (1990) 478.
- [Cr64] A. Crispin and P.J. Hayman, *Proc. Phil. Soc.* **83** (1964) 1051.
- [De49] S. Devons and M.G.N. Hines, *Proc. Roy. Soc.* **199** (1949) 56.
- [Di70] E.M. Diener, J.F. Amann, S.L. Blatt, and P. Paul, *Nucl. Instr. and Meth.* **83** (1970) 115.
- [Do72] W.R. Dodge and J.J. Murphy, *Phys. Rev. Lett.* **28** (1972) 839.
- [Do87] G. Domogala and H. Freiesleben, *Nucl. Instr. and Meth.* **A257** (1987) 7.
- [Dr81] D.M. Drake, L.R. Nilsson, and J. Faucett, *Nucl. Instr. and Meth.* **188** (1981) 313.
- [Dr89] V. Drndarevic, P. Ryge, and T. Gozani, *Nucl. Instr. and Meth.* **A277** (1989) 532.
- [Ej89] H. Ejiri, *Gamma Ray and Electron Spectroscopy in Nuclear Physics*, (Oxford, Clarendon Press, New York, Oxford University Press, 1989) 161.
- [En78] P.M. Endt and C. Van der Leun, *Nucl. Phys.* **A310** (1978) 1.
- [Ew87] G.T. Ewan *et al.*, Sudbury Neutrino Observatory Proposal, SNO-87-12 (1987).
- [Fe90] G. Feldman, M.J. Balbes, L.H. Kramer, J.Z. Williams, H.R. Weller, and D.R. Tilley, *Phys. Rev. C* **42** (1990) R1167.

- [Fl51] B.H. Flowers and F. Mandl, Roy. Soc. Proc. **A206** (1951) 131.
- [Fo48] W.A. Fowler, C.C. Lauritsen, and T. Lauritsen, Rev. Mod. Phys. **20** (1948) 236.
- [Fo49] W.A. Fowler and C.C. Lauritsen, Phys. Rev. **76** (1949) 314.
- [Ge91] G. Gervino, M. Anghinolfi, M. Castoldi, P. Corvisiero, G. Ricco, M. Sanzone, M. Taiuti, and A. Zucchiatti, Nucl. Instr. and Meth. **A309** (1991) 497.
- [Gi59] J.H. Gibbons and R.L. Macklin, Phys. Rev. **114** (1959) 571.
- [Gi60] J.H. Gibbons and H.W. Newson, in *Fast Neutron Physics, Part 1*, ed. J.B. Marion and J.L. Fowler, (Interscience Publishers, Inc., New York, Interscience Publishers Ltd., London, 1960) 133.
- [Go59] H.E. Gove, in *Nuclear Reactions, Vol. I*, ed. P.M. Endt and M. Demeur, (North-Holland Publishing Company, Amsterdam, 1959) 259.
- [Go72] N.B. Gove and A.H. Wapstra, Nuclear Data Tables **A11** (1972) 127.
- [Gr74] B. Grosswendt, Nucl. Instr. and Meth. **116** (1974) 97.
- [Gr75] B. Grosswendt and E. Waibel, Nucl. Instr. and Meth. **131** (1975) 143.
- [Gu67] A.K. Gupta and N. Nath, Nucl. Instr. and Meth. **53** (1967) 352.
- [Ha74] M.D. Hasinoff, S.T. Lin, D.F. Measday, and T.J. Mulligan, Nucl. Instr. and Meth. **117** (1974) 375.
- [Ha79] D. Halderson and R.J. Philpott, Phys. Rev. Lett. **42** (1979) 36, and **44** (1980) 54.
- [Ha83] O. Häusser, M.A. Lone, T.K. Alexander, S.A. Kushneriuk, and J. Gascon, Nucl. Instr. and Meth. **213** (1983) 301.
- [Ha86] Harshaw/Filtrol Partnership, Technical Reference GE 114.
- [Ha88] A. Håkansson, J. Blomgren, S. Crona, A. Likar, A. Lindholm, L. Nilsson, N. Olsson, and R. Zorro, Nucl. Instr. and Meth. **A273** (1988) 211.
- [He54] W. Heitler, *The Quantum Theory of Radiation*, 3rd Edition, (Oxford University Press, London, 1954) 272.
- [Ho48] P.V.C. Hough, Phys. Rev. **73** (1948) 266.
- [Ir75] J.D. Irish, R.G. Johnson, B.L. Berman, B.J. Thomas, K.G. McNeill, and J.W. Jury, Can. J. Phys. **53** (1975) 802.
- [Ja82] J.F. Janni, Atomic Data and Nuclear Data Tables **27** (1982) 147.
- [Jo64] W.R. Johnson, D.J. Buss, and C.O. Carroll, Phys. Rev. **135** (1964) A1232.
- [Ka56] H. Kahn, *Applications of Monte Carlo*, Rand Corporation Research Memorandum RM-1237-AEC (Rand Corp., 1956).
- [Ke60] E. Keil, E. Zeitler, and W. Zinn, Z. Naturforsch. **15a** (1960) 1031.

- [Ke77] C.R. Kerns, IEEE Trans. Nucl. Sci. **NS-24** (1977) 353.
- [Ki66] H.J. Kim, W.T. Milner, and F.K. McGowan, Nuclear Data **A1** (1966) 225.
- [Kn89] G.F. Knoll, *Radiation Detection and Measurement*, 2nd Edition, (John Wiley and Sons, Inc., New York, Chichester, Brisbane, Toronto, Singapore, 1989).
- [Ko59] H.W. Koch and J.W. Motz, Rev. Mod. Phys. **31** (1959) 920.
- [Ko79] M.A. Kovash and S.L. Blatt, Nucl. Instr. and Meth. **163** (1979) 113.
- [Le78] Table of Isotopes, Seventh Edition, ed. C.M. Lederer and V.S. Shirley, (John Wiley and Sons, Inc., New York, Chichester, Brisbane, Toronto, 1979).
- [Le84] E.E. Lewis and W.F. Miller, *Computational Methods of Neutron Transport*, (Wiley-Interscience, New York, 1984) Chapter 7.
- [Le90] Lecroy 1990 Catalog. Reference Guide to Digital Waveform Instruments, page IV-2.
- [Le92] SNO Internal Report DC-17-360-01, ed. J.R. Leslie (1992).
- [Li37] M.S. Livingston and H.A. Bethe, Rev. Mod. Phys. **9** (1937) 245.
- [Li73] H. Liskien and A. Paulsen, Nuclear Data Tables **A11** (1973) 569.
- [Li75] H. Liskien and A. Paulsen, Atomic Data and Nuclear Data Tables **15** (1975) 57.
- [Ma78] R. Madey, F.M. Waterman, A.R. Baldwin, J.N. Knudson, J.D. Carlson, and J. Rapaport, Nucl. Instr. and Meth. **151** (1978) 445.
- [Ma82] B. Maurel, G. Amsel, and J.P. Nadai, Nucl. Instr. and Meth. **197** (1982) 1.
- [Mc48] W.A. McKinley, Jr. and H. Feshbach, Phys. Rev. **74** (1948) 1759.
- [Mc80] R.C. McBroom, H.R. Weller, S. Manglos, N.R. Roberson, S.A. Wender, D.R. Tilley, D.M. Skopik, L.G. Arnold, and R.G. Seyler, Phys. Rev. Lett. **45** (1980) 243. See also R.C. McBroom, H.R. Weller, N.R. Roberson, and D.R. Tilley, Phys. Rev. C **25** (1982) 1644.
- [Mc88] V. McLane, C.L. Dunford, and P.F. Rose, *Neutron Cross Sections, Volume 2*, (Academic Press, Inc., San Diego, 1988).
- [Me70a] H. Messel and D.F. Crawford, *Electron-Photon Shower Distribution Function*, (Pergamon Press, Oxford, 1970).
- [Me70b] W.E. Meyerhof, M. Suffert, and W. Feldman, Nucl. Phys. **A148** (1970) 211.
- [Me85] C.L. Melcher, J.S. Schweitzer, A. Liberman, and J. Simonetti, IEEE Trans. Nucl. Sci. **NS-32** (1985) 529.
- [Na91] S.I. Nagornyi, Yu.A. Kasatkin, V.A. Zolenko, I.K. Kirichenko, and A.A. Zayats, Sov. J. Nucl. Phys. **53** (1991) 228.
- [Ne85] W.R. Nelson, H. Hirayama, and D.W.O. Rogers, Stanford Linear Accelerator Center SLAC-Report-265, December 1985.

- [No91] S. Nozawa, private communication.
- [Nu89] *Nuclides and Isotopes*, Fourteenth Edition, Revised 1989 by F.W. Walker, J.R. Parrington, and F. Feiner, ©1989 General Electric Co.
- [Pa74] P. Paul, in *Nuclear Spectroscopy and Reactions, part A*, ed. J. Cerny (Academic Press, New York, 1974) 345.
- [Pe55] J.E. Perry, Jr. and S.J. Bame, Jr., Phys. Rev. **99** (1955) 1368.
- [Ph79] T.W. Phillips, B.L. Berman, D.D. Faul, J.R. Calarco, and J.R. Hall, Phys. Rev. C **19** (1979) 2091.
- [Re71] I. Reichstein, D.R. Thompson, and Y.C. Tang, Phys. Rev. C **3** (1971) 2139.
- [Sa84] A.M. Sandorfi and M.T. Collins, Nucl. Instr. and Meth. **222** (1984) 479.
- [Sc63] W.T. Scott, Rev. Mod. Phys. **35** (1963) 231.
- [Se84] S.M. Seltzer and M.J. Berger, Int. J. Appl. Radiat. Isot. **35** (1984) 665.
- [Se86a] S.M. Seltzer and M.J. Berger, At. Data Nucl. Data Tables **35** (1986) 345.
- [Se86b] S.J. Seestrom-Morris, C.L. Morris, J.M. Moss, T.A. Carey, D. Drake, J.-C. Dousse, L.C. Bland, and G.S. Adams, Phys. Rev. C **33** (1986) 1847.
- [Sh56] N. Sherman, Phys. Rev. **103** (1956) 1601.
- [Sh90] K. Shibata, Japan Atomic Energy Research Institute Report JAERI-M 90-024. See also J. Nucl. Sci. Technol. **27** (1990) 81.
- [Si72] D. Sinclair, *A Study of the Low Energy Levels in ^{127}I using the $^{127}\text{I}(n, n'\gamma)$ Reaction*, Ph.D. Dissertation (Queen's University at Kingston, 1972) 28.
- [So92] S.A. Sofianos, H. Fiedeldey, and W. Sandhas, Few-Body Systems, Suppl. **6** (1992) 276.
- [Sp89] M. Spahn, Th. Kihm, K.T. Knöpfle, J. Friedrich, N. Voegler, Ch. Schmitt, V.H. Walther, M. Unkelbach, and H.M. Hofmann, Phys. Rev. Lett. **63** (1989) 1574.
- [St70] E. Storm and H.I. Israel, Nuclear Data Tables **A7** (1970) 565.
- [Su68] M. Suffert, W. Feldman, J. Mahieux, and S.S. Hanna, Nucl. Instr. and Meth. **63** (1968) 1.
- [Ti92] D.R. Tilley, H.R. Weller, and G.M. Hale, Nucl. Phys. **A541** (1992) 1.
- [Ts73] H.K. Tseng and R.H. Pratt, Phys. Rev. A **7** (1973) 1423.
- [Un90] M. Unkelbach, private communication.
- [Ur92] V. Uras, Master's Thesis, Queen's University at Kingston, (1992) (unpublished).
- [Va81] B.J. Varley, J.E. Kitching, W. Leo, J. Miskin, R.B. Moore, K.D. Wunsch, R. Decker, H. Wollnik, and G. Siegert, Nucl. Instr. and Meth. **190** (1981) 543.

- [Wa81] L. Ward, D.R. Tilley, D.M. Skopik, N.R. Roberson, and H.R. Weller, Phys. Rev. C **24** (1981) 317.
- [Wa88] B. Wachter, T. Mertelmeier, and H.M. Hofmann, Phys. Rev. C **38** (1988) 1139.
- [We81] H.R. Weller and N.R. Roberson, IEEE Trans. Nucl. Sci. **NS-28** (1981) 1268.
- [We82] H.R. Weller, N.R. Roberson, G. Mitev, L. Ward, and D.R. Tilley, Phys. Rev. C **25** (1982) 2111.
- [We91] R. Wervelman, K. Abrahams, H. Postma, J.G.L. Booten, and A.G.M. van Hees, Nucl. Phys. **A526** (1991) 265.
- [We92] D.P. Wells, D.S. Dale, R.A. Eisenstein, F.J. Federspiel, M.A. Lucas, K.E. Mellendorf, A.M. Nathan, and A.E. O'Neill, Phys. Rev. C **46** (1992) 449.
- [Ya91] Q. Yang, D.J. O'Connor, and Zhonglie Wang, Nucl. Instr. and Meth. **B61** (1991) 149.
- [Ze63] C.D. Zerby, in *Methods in Computational Physics*, Volume 1, ed. B. Alder, S. Fernbach, and M. Rotenberg, (Academic Press, New York and London, 1963) 90.
- [Zu63] R.W. Zurmühle, W.E. Stephens, and H.H. Staub, Phys. Rev. **132** (1963) 751.

Vita

Name: Robert John Komar

Place and year of birth: Sudbury, Ontario, 1963

Education: Ontario primary and secondary schools;
completed Grade XIII 1981

Queen's University 1981-85;
awarded B.Sc. Eng. (Physics) 1985

Queen's University 1985-87;
awarded M.Sc. 1987

Queen's University 1988-92;
present program

Experience: Summer Student (Nuclear Physics)
Queen's University 1984,1985

Teaching Assistant (Physics)
Queen's University 1985-92

Awards: Ontario Scholarship, 1981

Susan Near Scholarship,
Queen's University, 1984

Dean's Award,
Queen's University, 1984

G. Neilson Whyte Fellowship,
Queen's University, 1985-86

Reinhardt Fellowship,
Queen's University, 1986-89, 1990-92

McLaughlin Fellowship,
Queen's University, 1988-89

Queen's Graduate Fellowship,
Queen's University, 1989-90, 1991-92